

ION-FLOW DRIVEN INSTABILITIES IN  
SHEATH-PRESHEATH REGION OF LOW  
TEMPERATURE PLASMA

*By*

VARA PRASAD KELLA

PHYS06201104007

INSTITUTE FOR PLASMA RESEARCH, GANDHINAGAR

A thesis submitted to the  
Board of Studies in Physical Sciences

In partial fulfillment of requirements  
for the degree of

DOCTOR OF PHILOSOPHY

*of*

HOMI BHABHA NATIONAL INSTITUTE

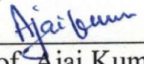

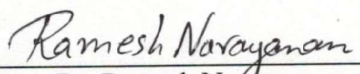
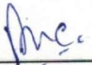
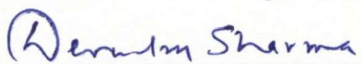
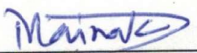
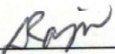
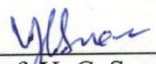


July 2017

# Homi Bhabha National Institute

## Recommendations of the Viva Voce Committee

As members of the Viva Voce Committee, we certify that we have read the dissertation prepared by VARA PRASAD KELLA entitled "ION-FLOW DRIVEN INSTABILITIES IN SHEATH-PRESHEATH REGION OF LOW TEMPERATURE PLASMA" and recommend that it may be accepted as fulfilling the thesis requirement for the award of Degree of Doctor of Philosophy.


 Chairman - Prof. Ajai Kumar	Date: 08/11/2017
 Guide / Convener - Dr. Joydeep Ghosh	Date: 08/11/2017
 Examiner - Dr. Ramesh Narayanan	Date: 08/11/2017
 Member 1- Prof. P. K. Chattopadhyay	Date: 08/11/2017
 Member 2- Dr. Devendra Sharma	Date: 08/11/2017
 Member 3- Dr. Mainak Bandyopadhyay	Date: 08/11/2017
 Member 4- Dr. D. Raju	Date: 08/11/2017
 Tech. Adviser- Prof. Y. C. Saxena	Date: 08/11/2017

Final approval and acceptance of this thesis is contingent upon the candidate's submission of the final copies of the thesis to HBNI.

I/We hereby certify that I/we have read this thesis prepared under my/our direction and recommend that it may be accepted as fulfilling the thesis requirement.

Date: 8/11/17

Place: IPR, Gandhinagar

  
Guide

## STATEMENT BY AUTHOR

This dissertation has been submitted in partial fulfillment of requirements for an advanced degree at Homi Bhabha National Institute (HBNI) and is deposited in the Library to be made available to borrowers under rules of the HBNI.

Brief quotations from this dissertation are allowable without special permission, provided that accurate acknowledgement of source is made. Requests for permission for extended quotation from or reproduction of this manuscript in whole or in part may be granted by the Competent Authority of HBNI when in his or her judgement the proposed use of the material is in the interests of scholarship. In all other instances, however, permission must be obtained from the author.



Vara Prasad Kella

## DECLARATION

I, hereby declare that the investigation presented in the thesis has been carried out by me. The work is original and the work has not been submitted earlier as a whole or in part for a degree/diploma at this or any other Institution/University.

A handwritten signature in blue ink, appearing to read 'K. P. Kella', is positioned above the printed name.

Vara Prasad Kella



## List of Publications arising from the thesis

### Journal:

1. A comparative study of sheath potential profile measurements with laser-heated and current-heated emissive probes  
Vara Prasad Kella, Payal Mehta, A. Sarma, J. Ghosh, P.K. Chattopadhyay. *Rev. Sci. Instrum.* **87**, 043508, (2016).
2. Observation of ion-ion counter streaming instability in presheath-sheath region of mesh grid immersed in low temperature plasma  
Vara Prasad Kella, J. Ghosh, P. K. Chattopadhyay, D. Sharma and Y. C. Saxena. *Physics of Plasmas* **24**, 032110, (2017).
3. Experimental observation of ion-ion co-streaming instability in the presheath region of a mesh grid immersed in Ar+He two-ion-species laboratory plasma  
Vara Prasad Kella, J. Ghosh, D. Sharma, Y. C. Saxena and P. K. Chattopadhyay. *Under internal review.*
4. Self-excited ion-acoustic instability in the presheath of low temperature plasma  
Vara Prasad Kella, J. Ghosh, D. Sharma, Y. C. Saxena and P. K. Chattopadhyay. *to be submitted.*
5. Effective electron temperature measurement using line intensity ratio method in Ar+He two-ion species plasma  
Vara Prasad Kella, J. Ghosh, S. Banerjee, R. Manchanda and C. Malay. *to be submitted.*

K. V. P. K.

Vara Prasad Kella

## DEDICATIONS

To my parents  
Satyavati and Simhachalam  
grandparents  
Durgamba and Subba Rao garu.

## ACKNOWLEDGEMENTS

First of all I would like to thank the God, who gave me the great family. The Sacrifice of my parents Satyavati and Simhachalam; and sisters Krishnaveni, Annapurna and Triveni, only make my education possible. The knowledge and character I gain from them make me proud. I am also grateful to my grandparents Durgamba and Subba Rao garu, who given immense of support and encouragement in my education.

I especially thank to my supervisor Dr. Joydeep Ghosh for his guidance, support and motivation in completing this thesis. I am grateful to his friendly and helping nature. I enjoyed a lot in discussing with him right from the beginning of course work. The patience and methodology he observed in clarifying the concepts to the new comers to the field like me are great. The independence given by him helps me in defining the research problems to be addressed and able to enjoy the flavor of research work. It is my pleasure to work with him and very much happy to continue the journey in plasma physics research in the future.

I convey my thanks to Doctoral Committee members Prof. Ajai Kumar, Prof. Y.C. Saxena, Prof. P. K. Chattopadhyay, Dr. Devendra Sharma, Dr. Mainak Bandyopadhyay, Dr. D. Raju for their valuable suggestions and visionary thoughts in defining the experimental work and understanding the results. The discussion with the members helps me in understanding the concepts and how to think and carry in the right way.

I would like to thank Prof. Amita Das, Prof. Sudip, Prof. Ganesh, Prof. Mukerjee, Dr. Kundu, Dr. Devendra Sharma, Prof. P. K. Chattopadhyay, Dr. Joydeep Ghosh, Dr. Shantanu Karkari, Dr. G. Ravi, Mrs. Bharati, Dr. Mukhesh Ranjan for teaching plasma physics during the course work in IPR. I am also thankful to all the Teachers, who taught me from preschool to post graduation level. Their dedication and love on the respective subjects motivate me to continue the education. I am grateful to their encouragement and wishes in this journey.

The immense help of Spectroscopy group members Mrs. Ranjana, Dr. Malay, Dr. Santanu, Mrs. Nilam, Dr. Payal, Mrs. Niral and Aditya Team members - Mr. Kumar, Mr. Tanna makes the experiments possible and carried out smoothly in Spectroscopy Division, IPR. Their help in developing the experimental set-up

and diagnostics; learning spectroscopy techniques is highly appreciated. I thanks to the Library team, who make the treasure of plasma physics resources in IPR library. The resources provided by the Library team help me to gain knowledge in plasma physics. The response and support from the work shop team in IPR make the things going in experiments. Their understanding makes the designing and development of vacuum system and diagnostics so easy to me. The efforts made by the stores section and purchase section in providing the required instruments in time are great.

Thanks to my all friends, who accompanied with me during childhood, schooling, college, and university campus, and made every moment memorable. I specially convey my thanks to the friends in IPR who make me pleasant and helpful environment. The warm welcome and support given by my seniors Veda Prakash, Kshitish, Guru, Satya, Jugal, Deepak, Ujjwal, Rana, Vikram, Sharad, Sushil, Sanat, Pravesh, Rameswar, Aditya, Soumen, Sayak, Manjit, Sita, Vikram, Vikrant, Prabal and others was memorable. The company of my friends Akanksha, Vidhi, Deepa, Bibhu, Mangi, Rupendra, Neeraj and other hostelmates Harish, Samir, Megharaj, Chandra sekar, Salim, Upendra Prasad, Debu, Sonu, Umesh, Amit, Arghya, Modhu, Narayan, Ratan, Bhumika, Sagar, Aalam, Deepak, Atul, Chetan, Prabhakar, Pallavi, Meenakshi, Shivam, Rupak, Jana, Gaurav, Avinish, Dipshika, Preeti, Neeraj, Arnab, Arun, Yogesh and others whose company made hostel life memorable.

I would also like to thank the Cricket players of Research Scholar (RS) -Team, IPR-Team and all other different group teams in IPR for their joyful and memorable company in the cricket field.

Finally, Thanks to the great gifts in my life, my better half Lakshmi Prasanna and my energy booster, my son Yeshmit, who helps a lot in making me happy, energetic and motivated throughout this great journey.



## SYNOPSIS

For all practical purposes, plasma has to come in contact with material wall. In the contact region of the plasma with the material surface, a potential exists to contain the more mobile charged species of the plasma. The non-neutral potential region of plasma which exists between quasi-neutral plasma and material surface in contact with the plasma is termed as ‘sheath’. There also exists a transition region between the quasi-neutral plasma and non-neutral sheath, called ‘presheath’, in order to maintain the flux of lesser mobile charged species of the plasma. These ‘sheath-presheath’ region is very critical in defining the nature of interaction of plasma particles with the material surface. Particle dynamics in sheath-presheath defines the most important phenomena in plasmas like, etching processes of material surface using plasma, particle implantation processes using plasmas, heat-loads to the walls of the chamber in which the plasma is contained, temperature of plasma particles etc.

Generally, in unmagnetized, low pressure plasma, the surface in contact with plasma attains negative floating potential by virtue of higher mobility of electrons than ions. Plasma shields this potential in a narrow positive space charge region called Sheath. In order to have a stable sheath structure, ions needed to enter the sheath edge with a minimum velocity  $v \geq \sqrt{kT_e/M_i}$ , called Bohm velocity [1]. Ions reach to the Bohm velocity by the potential drop of  $\sim \frac{1}{2} kT_e$  in the transition region called Presheath. This ion flow is generally believed to be laminar as it accelerates from the presheath to enter into the sheath region. However, it has been reported recently that under certain discharge conditions of low neutral pressure, the ion flow in presheath region may not remain laminar [2, 3]. Instead, instabilities like ion-acoustic instability, secondary electron emission instability [4, 5], ion-ion counter streaming instability [6, 7] exist in sheath-presheath region formed around solid/perforated material surfaces in low temperature plasma [8, 9]. Further in multi-ion species plasmas, presence of ion-ion co-stream instability in the sheath-presheath region has also been reported along with the above mentioned ones [9, 10]. These instabilities in the sheath-presheath region modify the particle

flow velocities and distribution functions which is predicted to affect the particle transport in this region [11].

In general, the instabilities in the sheath-presheath region can be classified into three categories: (1) ion-ion instabilities (2) electron-ion instabilities and (3) electron-electron instabilities. Ion-ion instability may arise either in presence of two different ion streams moving in the same direction in the sheath-presheath or in two inter-penetrating ion streams of same ion species or different ion species. The earlier case is possible in multi-ion species plasma, where different ion species streaming along with each other in sheath-presheath and latter is possible in sheaths produced by transparent grids in the plasma. Electron-ion instabilities excitation depends on phase velocities of the wave electron and ion distribution function, i.e., when the phase velocity of the wave matches with the positive slope of the electron distribution function, ion wave receives energy from the electrons and grows as instability [12]. Electron-electron instabilities are excited in the presence of secondary-electron emission from the physical surface. Hall-thrusters are one of the devices, which contains this instability [13].

Ion-flow driven instabilities in sheath-presheath region have major importance in the context of particle dynamics. When these instabilities exist, the instabilities can enhance the friction between the particles. In general, the instability enhanced friction is much stronger than the normal coulomb collision friction, so that the role of the instability in particle dynamics would be significant [8, 14]. Sheath-presheath region is much susceptible to the ion flow-driven instabilities due to the accelerated flow of ions. The commonly encountered ion-flow driven instabilities in the presheath region, formed around the solid/perforated surfaces in contact with low temperature, low pressure, single or two-ion-species plasma, are ion-acoustic instability, ion-ion counter streaming instability and ion-ion co-stream instability.

When counter streaming of two ion beams exists in the presheath region, there could be a possibility of ion-ion counter streaming instability. This instability is commonly found in the presheath near grids immersed in plasma, space plasmas and near virtual cathodes. Grids have been normally used in the plasma discharges

in double plasma devices, ion-beam extractors for ion and neutral etching processes etc. Ion-ion counter streaming instability is encountered near the grids because of the counter streaming of ions from both sides of the grids [6, 7]. Anomalous ion heating has been reported caused by the presence of the ion-ion counter streaming in ionosphere [15]. Recently, ion velocity-locking observed near the virtual cathode and ion-ion counter streaming instability is identified to be responsible for ion-ion enhanced collisions [16].

Studies of electrostatic instabilities in multi-ion species plasma frequently encountered in ionosphere and fusion plasmas have attained much interest for understanding generalized Bohm criterion in multi-ion species plasmas. Recent experiments show that, in two ion-specie plasma of nearly equal ion densities, both the ion species, reach the sheath edge with equal velocities in the same potential fall despite having different masses. Theoretical works predicts that, ion-ion two-stream instability generated by the differential flow of two ion species could be the reason to draw the lighter and heavier ion species to common velocity at the sheath edge [9].

Ion-acoustic instability has been reported to be responsible for anomalous ion heating in collisionless, low pressure discharges [17]. Experimentally, current-driven ion-acoustic instability has been studied in low temperature  $\left(\frac{T_e}{T_i} \gg 1\right)$ , laboratory experimental devices by introducing electron and ion beams of suitable energies into the background plasma [12, 18–21]. The ion-acoustic instability can also be self-excited near the sheath edge region where the ions reach with Bohm velocity [11]. This ion-acoustic instability near the sheath-presheath edge is thought to be reason for Langmuir’s Paradox, i.e., anomalous fast equilibration of electron distribution function to Maxwellian in low temperature and low pressure discharges. Electron scattering via an instability-enhanced collective response and hence fluctuations arising from convective ion-acoustic instability near the discharge boundary might be the reason for this Paradox [22].

Although, the sheath-presheath instabilities are studied in detail theoretically, the experimental observations of these instabilities are rare or non-existing. In this

thesis work, experimental measurements of ion-flow driven instabilities excited in the presheath of low temperature plasma, namely (1) ion-ion counter streaming instability (2) ion-ion co-streaming instability in two-ion species plasma and (3) ion-acoustic instability has been reported and analyzed. The experimental observations are ably supported by deriving dispersion relations for the above mentioned instabilities. The thesis is organized as the follows:

## **Chapter-1: Introduction and outline**

This chapter presents a comprehensive review on formation and existence of sheath-presheath region and the instabilities present in sheath-presheath region, mainly the ion-flow driven instabilities, in low temperature plasmas. The review is followed by the motivation behind the work carried out and presented in this thesis.

## **Chapter-2: Experimental set-up and diagnostics**

The instabilities in the sheath-presheath region are studied in a linear, filament-produced plasma device. The compatible and versatile device has been designed and installed in IPR from scratch to carry out the above-mentioned studies. The linear device consists of a stainless steel (SS) discharge chamber of length 50 cm and inner diameter 20 cm. For studying the instabilities in low pressure plasmas, the experimental chamber is evacuated up to a base pressure of  $3 \times 10^{-6}$  mbar using turbo molecular pump (TMP) backed by a rotary pump. Plasma is produced in the device using biased hot-filaments located at one end of the chamber. Permanent magnets are installed on the inner periphery of the cylindrical chamber along the axis to obtain a broken-line cusp magnetic field configuration to enhance the plasma density. Argon, Helium and Argon + Helium plasmas with densities in the range of  $\sim 5 \times 10^7 - 2 \times 10^9$  /cc and temperatures in the range of  $\sim 2 - 8$  eV have been obtained in this device by varying the fill-in gas pressure, the bias voltage and the filament current. A planar SS grids of side 5 cm and thickness  $\sim$



0.1 mm with  $\sim 75$  % transparency is used for producing the sheath-presheath near the axial and vertical center of the experimental chamber. The plasma as well as the sheath-presheath region has been diagnosed with cold Langmuir probes, emissive probes and spectroscopy to measure the plasma parameters and their fluctuations. The dimension of the sheath and presheath are determined by measuring the spatial profiles of plasma potential using emissive probes. The movable cylindrical Langmuir probe made of tungsten having length 4 mm and diameter 0.7 mm is employed for measurement of plasma parameters and their fluctuations in the sheath-presheath and in bulk plasmas. The instabilities are identified by analyzing the measured time series of floating potential fluctuation from both movable Langmuir probe and stationary grid using Fast Fourier Transform algorithm. This chapter describes the experimental device and the diagnostics.

### **Chapter-3: Identification of Sheath-presheath boundaries**

Before exploring the sheath-presheath instabilities, the sheath-presheath plasma region has been thoroughly characterized and the sheath-presheath boundaries are measured. This has been done by measuring the plasma potential profile in the sheath-presheath-bulk region of plasma using two different types of emissive probe namely, current-heated emissive probe (CEP) and laser-heated emissive probe (LHEP). The experimentally measured potential profiles are then fitted with Child-Langmuir profile (CLP) to obtain the sheath dimension. The region between the sheath having CLP and the bulk having constant potential profile provides the dimension of the presheath region. Estimations of Sheath and presheath boundaries using CEP and LHEP emissive probes along with the development and advantages of Laser-heated have been discussed in this chapter.

### **Chapter-4: Ion-ion counter streaming instability in the presheath of single ion species and two-ion species plasmas**

Observation of ion-ion counter streaming instability in the presheath region of the grid by virtue of counter-streaming of ions from both sides of the grids in single ion species plasma (Argon and Helium) as well as in two-ion species (Argon + Helium) plasma is presented in this chapter. The observation of ion-ion counter streaming instability in the presheath region of the grid in two-ion species (Argon + Helium) plasma is reported for the first time. The broad band peaks in the frequency spectra (Ar plasma: 10-20 kHz; He plasma: 25-35 kHz; Ar + He plasma: 10-40 kHz) of measured floating potential fluctuations of grid and Langmuir probe on both sides of the grid are identified as ion-ion counter streaming instability. The instability is successfully terminated by restricting the ion flow through the grid by covering the grid from one side. The phase velocity and wave number of the wave have been obtained by simultaneous measurement of grid and Langmuir probe signals. The wave number estimated through phase velocity measurement matched well with the derived dispersion relation for both the single and two-ion species plasmas [6]. The derived dispersion relation predicted excitation of wider range of wave numbers in two-ion species plasma, which is experimentally corroborated through observation of broader and flatter peaks (10-40 kHz) in the frequency spectra of fluctuations in Ar + He plasma [6].

## **Chapter-5: Ion-ion co-stream instability in the presheath of two-ion species plasma**

This chapter illustrates the observations of ion-ion co-streaming instability in the presheath region of the grid immersed in two-ion species (Ar + He) plasma [10]. To the best of our knowledge these results are never reported before. Unlike, the ion-ion counter streaming instability, the co-streaming instability is observed only when the ion concentrations of both the specie are equal. The neutral pressure ratio of Ar and He is being maintained around  $\left(\frac{P_{He}}{P_{Ar}}\right) \sim 15-18$  for obtaining equal concentrations of Ar and He ions in two specie plasma [23]. The instability ceases to exist as the neutral pressure ratio is varied from  $\sim 15-18$  by increasing or de-

creasing the neutral pressure of any of the gases. Excitation of this instability with equal concentration of two ions may indicate its role in equilibrating the Bohm velocities of both the ions with different masses at the sheath edge as observed in other experimental [24] and theoretical [8] studies. The measured phase velocity of the wave is close to the individual Bohm velocity of the lighter species, i.e., of Helium in this case [10]. The measured wave number is consistent with the derived dispersion relation.

## **Chapter-6: Self-excited ion-acoustic instability in the presheath of single ion species plasma**

This chapter describes the observations of self-excited ion-acoustic instability in the sheath-presheath region [25]. Again, to the best of our knowledge, these observation are reported for the first time. The observed ion-acoustic instability is found to be very weak in comparison to the ion-ion co and counter streaming instabilities, which is consistent with the theory. Parametric studies show that the instability depends heavily on the ion-neutral collision frequency and exists in a very narrow plasma parameter range. The measured phase velocity of the wave matches well with the system sound speed within the experimental errors and the measured wave number remains consistent with the theoretical dispersion relation at the observed frequency.

## **Chapter-7: Conclusion and future scope**

The experimental results on the observations on ion-flow driven instabilities in sheath-presheath of low temperature plasma and their analysis presented in this thesis have been summarized in this chapter. Ion-ion counter streaming instability in single and two-ion species plasma, ion-ion co-streaming instability in two-ion-species plasma and ion-acoustic instability in single ion species plasma has been explored experimentally in sheath-presheath regime for the first time. The con-

ditions for the existence of these instabilities are studied in detail, which is vital for understanding nature of sheath-presheath phenomena. The experimental results are found to be in good agreement with the theoretical derived dispersion relations. Future scope includes further substantiation of these results using non-invasive spectroscopy diagnostics. For example, spectroscopic measurements of ion fluctuations of different ions separately in two ion-species plasma by varying the ion concentrations will be very useful in understanding the phenomena of ions with different masses reaching the sheath edge with equal Bohm velocities as observed in other experimental and theoretical studies.



# Contents

List of Figures . . . . .	xv
List of Tables . . . . .	xxi
<b>1 Introduction</b>	<b>1</b>
1.1 Introduction to Plasma . . . . .	1
1.1.1 Debye Shielding . . . . .	5
1.2 Sheath-Presheath . . . . .	8
1.2.1 General Sheath Condition for multi-ion species plasma . . .	10
1.2.2 Child-Langmuir's Law . . . . .	13
1.2.3 Presheath potential profile . . . . .	14
1.3 Collisions in Plasma . . . . .	15
1.3.1 Coulomb Collisions . . . . .	16
1.3.2 Ion-Neutral Collisions . . . . .	18
1.4 Instabilities in Unmagnetized Plasma . . . . .	20
1.4.1 Ion-flow driven Instabilities . . . . .	21
1.5 Ion-flow driven instabilities in sheath-presheath . . . . .	22
1.6 Motivation and Previous work . . . . .	24
1.7 Organization of the thesis . . . . .	29
<b>2 Experimental Set-up and Diagnostics</b>	<b>31</b>
2.1 Experiment Set-up . . . . .	32
2.2 Filament Discharge Plasma . . . . .	35
2.3 Plasma Parameters Measurement . . . . .	39
2.3.1 Langmuir Probe Theory . . . . .	40
2.3.1.1 Electron Flux . . . . .	41
2.3.1.2 ion flux . . . . .	43
2.3.1.3 Electron Current . . . . .	44
2.3.1.4 The Ion current . . . . .	45

## CONTENTS

2.3.1.5	Relation between $V_f$ and $V_P$ . . . . .	46
2.3.2	Sheath effects . . . . .	47
2.3.3	Fitting Experimental Data . . . . .	48
2.3.4	Langmuir probe Experimental Results . . . . .	49
2.4	Line Ratio Method . . . . .	54
2.4.1	Line ratio method Experimental Results . . . . .	57
2.5	Plasma Fluctuations Measurement and Analysis . . . . .	59
2.5.1	Wave number measurement . . . . .	63
2.6	Summary . . . . .	64
<b>3</b>	<b>Identification of Sheath-Presheath boundaries</b>	<b>67</b>
3.1	Introduction . . . . .	67
3.2	Estimation of Space potential using Emissive Probes . . . . .	70
3.2.1	Space Potential Measurement . . . . .	70
3.2.2	Laser-heated emissive probe . . . . .	74
3.3	Probes design . . . . .	75
3.4	Experimental Results and Discussions . . . . .	78
3.4.1	Estimation of Space potential using CEP . . . . .	79
3.4.2	Estimation of Space potential using LHEP . . . . .	80
3.4.3	Sheath Potential Profile Measurement using CEP and LHEP . . . . .	81
3.5	Conclusion . . . . .	87
<b>4</b>	<b>Ion-ion counter-streaming instability</b>	<b>89</b>
4.1	Introduction . . . . .	89
4.2	Experimental Set-up . . . . .	93
4.3	Experimental Results . . . . .	97
4.4	Dispersion relation for ion-ion counter streaming instability . . . . .	106
4.4.1	Single ion species plasma . . . . .	106
4.4.2	Two-ion-species plasma . . . . .	112
4.5	Discussion . . . . .	114
4.5.1	Effect of Mass Ratio on the instability . . . . .	118

4.6	Summary . . . . .	118
<b>5</b>	<b>Ion-ion co-streaming instability</b>	<b>121</b>
5.1	Introduction . . . . .	121
5.2	Plasma parameter regime . . . . .	124
5.3	Experimental Results and Discussion . . . . .	125
5.4	Conclusions . . . . .	139
<b>6</b>	<b>Ion-acoustic instability</b>	<b>141</b>
6.1	Introduction . . . . .	141
6.2	Linear Dispersion Relation . . . . .	143
6.3	Plasma parameter regime . . . . .	149
6.4	Experimental Results . . . . .	150
6.5	Discussion . . . . .	151
<b>7</b>	<b>Conclusions and Future scope</b>	<b>157</b>
7.1	Future Scope . . . . .	162
	<b>Bibliography</b>	<b>163</b>

# List of Figures

1.1	The range of density and temperature of plasmas [26] . . . . .	3
1.2	Variation of Debye length with plasma density for an electron temperature 2 eV. . . . .	7
1.3	Plasma potential and density variation in sheath-presheath region. .	9
1.4	The electrostatic potential (blue solid line) and ion flow (red dash line) throughout presheath. . . . .	16
1.5	ion-neutral mean path and collision frequency at the sheath edge (ion velocity $\sim$ Bohm velocity) with respect to neutral pressure . .	19
2.1	Schematic diagram of the experimental chamber. . . . .	33
2.2	Picture of the experimental set-up. . . . .	34
2.3	The variation of neutral pressure in the chamber with gas flow rate for Argon and Helium. . . . .	34
2.4	Electron-impact ionization cross-section for Argon[27]. . . . .	36
2.5	Schematic diagram of the circuit for plasma discharge. . . . .	37
2.6	Electron impact rate coefficients for Argon[28]. . . . .	38
2.7	Typical I-V characteristics of Langmuir probe . . . . .	41
2.8	Langmuir probe I-V trace. Solid line is the analytic fit for the experimental data . . . . .	50
2.9	Plot of logarithm of electron current vs bias current of the raw experimental data shows two populated electrons . . . . .	50
2.10	Second derivative of the fit . . . . .	51
2.11	EEDF obtained from fit to the experimental data . . . . .	51
2.12	Variation of the Distribution function with working pressure . . . .	52
2.13	Variation of the plasma density with working pressure at discharge current ( $I_d$ ) = 0.8 A and discharge voltage ( $V_d$ ) = 60V. . . . .	53



## LIST OF FIGURES

2.14	Variation of the effective electron temperature with working pressure at discharge current ( $I_d$ ) = 0.8 A and discharge voltage ( $V_d$ ) = 60V.	53
2.15	Emission spectra of Argon plasma at central wavelength 420nm . . .	58
2.16	Emission spectra of Argon plasma at central wavelength 434nm . . .	58
2.17	Electron temperature vs working pressure for a discharge current of 800 mA . . . . .	60
2.18	Power spectrum of the fluctuation data (a) with noise (b) with reduced noise using Welch method . . . . .	61
2.19	Keysight make InfiniiVision DSO-X 2024A model oscilloscope used for signal acquisition. . . . .	63
2.20	(a) Amplitude vs time of the two signals $f$ and $g$ . (b) Time delay between the signals $f$ and $g$ obtained by Cross-correlation . . . . .	65
3.1	Schematic diagram of probes (a) Laser-heated Emissive probe (b) Current-heated emissive probe . . . . .	76
3.2	Schematic diagram of the probe circuits . . . . .	77
3.3	(a) Schematic diagram of the chamber (b) Schematic of Laser-heated probe arrangement. . . . .	77
3.4	Characteristics of CEP for different emission currents. Electron density and temperature are $\sim 5 \times 10^{14} m^3$ and $\sim 2.5$ eV, respectively. .	81
3.5	CEP I-V traces for bias circuit connected to different legs of the probe; (-o-) for connection to positive leg and (-*-) for negative leg.	82
3.6	LHEP I-V traces for various emission levels in bulk plasma. Electron density and temperature are $\sim 5 \times 10^{14} m^3$ and $\sim 2.5$ eV, respectively.	83
3.7	Potential profile measured with LHEP and CEP for various distance from the plate surface. The error bar in distance (x-axis) is $\pm 1.5$ mm. Electron density and temperature are $\sim 4 \times 10^{14} m^3$ and $\sim 3$ eV, respectively. . . . .	85
3.8	Child law and Presheath potential fit to the LHEP experimental data. The measurement errors are within $\pm 5\%$ . . . . .	86

4.1	(a) Grids placed in the plasma (b) near virtual cathode formation (c) wake formation behind the object in flowing plasma (d) Terrestrial region of ionospheric plasma. ion flows are shown with arrows. . . .	91
4.2	(a) Schematic diagram of the experimental set-up. (b) Cross-sectional view showing surface cusp magnetic field (c) Circuit diagram for Grid and Langmuir probe. . . . .	94
4.3	Typical filtered fluctuation signals between 10-30 kHz, acquired simultaneously from floating mesh grid and floating langmuir probe .	95
4.4	Power spectra of (a) Grid and (b) Langmuir probe shows broad band frequency in the frequency range 20 kHz at working pressure $8 \times 10^{-4}$ mbar, discharge current 1.2 A, discharge voltage 80 V, $n_e = 8 \times 10^8/cc$ , $T_e = 4$ eV. . . . .	98
4.5	Frequency spectra of floating potential fluctuations from Langmuir probe in presheath and bulk plasmas. At working pressure $9 \times 10^{-4}$ mbar, discharge current 0.75 A, discharge voltage 80 V, $n_e = 6 \times 10^8/cc$ , $T_e = 3$ eV. . . . .	99
4.6	Variation of low frequency peak with discharge current. Central frequency (blue line -*-) and width of the broad band peak (red line -o-) decreases with decreasing discharge current. working pressure $8 \times 10^{-4}$ mbar, discharge voltage 80 volts . . . . .	100
4.7	Variation of low frequency peak with neutral pressure. Central frequency (blue line -*-) and width of the broad band peak (red line -o-) decreases with decreasing neutral pressure. Discharge current 1.2 A, discharge voltage 80 volts . . . . .	101
4.8	Graph showing power spectral density vs. frequency for high and low working pressures. High pressure: $6 \times 10^{-3}$ mbar; Low pressure: $8 \times 10^{-4}$ mbar . . . . .	102
4.9	Ion-neutral mean free path vs. working pressure. The mean free path approaches the presheath dimension ( $\sim 1$ cm), at high neutral pressures $4 - 6 \times 10^{-3}$ mbar. . . . .	103

## LIST OF FIGURES

4.10	Power spectra of ion-ion counter streaming instability in logarithmic scale, in Argon, Helium and Ar+He multi ion species plasma. $P_{fill} = 3 \times 10^{-3}$ mbar, $n_e \sim 5 \times 10^8/cc$ , $T_e \sim 2-3$ eV. . . . .	105
4.11	Function (Y) vs frequency ( $\omega$ ) for $\frac{kV_0}{\omega_p} > \sqrt{2}$ , in experimental conditions of ion plasma frequency 1 MHz. It is clear from figure that the dielectric response function has four real roots . . . . .	109
4.12	Function (Y) vs frequency ( $\omega$ ) for $0 < \frac{kV_0}{\omega_p} < \sqrt{2}$ , in experimental conditions of ion plasma frequency 1 MHz. It is clear from figure that the dielectric response function has two real roots and two imaginary roots. . . . .	110
4.13	Growth rate of ion-ion counter streaming instability for $V^2/C_s^2 = 0.2, 0.4, 0.6$ and $0.8$ in presheath. . . . .	110
4.14	Normalized growth rates for ion-ion counter streaming instability in two-ion-species (Ar-He) plasma for different Mach numbers ( $M = V/C_s$ ), $M^2 = 0.8$ (solid line), $0.6$ (dotted line), $0.4$ (dashed line), $0.2$ (dash-dot line), with $\omega_{pr} = \omega_{p2}/\omega_{p1} = \sqrt{10}$ . . . . .	113
4.15	Schematic diagram of Sheath-Presheath produced on both side of mesh grid immersed in plasma. Arrow indicates counter streaming of ions across the mesh grid from either side, accelerated through potential well . . . . .	115
4.16	Correlation between time series data of Langmuir probe and Grid showing a time delay of 5 micro seconds . . . . .	116
4.17	Grid and Langmuir probe floating potential fluctuation signal, filtered between 20-22 kHz. . . . .	117
4.18	Grid and Langmuir probe floating potential fluctuation signal, filtered between 20-22 kHz. . . . .	119
4.19	Frequency plot with grid in floating and biased in the electron saturation regime (+10 V) . . . . .	120

5.1	(a) Schematic diagram of the experimental set-up. (b) Cross-sectional view showing surface cusp magnetic field (c) Circuit diagram for Grid and Langmuir probe. . . . .	125
5.2	Wavelength spectra shows emission spectral lines from He I and Ar I in Ar+He plasma . . . . .	128
5.3	Time series data of floating potential fluctuations from (a) grid and (b) Langmuir probe . . . . .	128
5.4	Frequency spectra of floating potential fluctuation signal from (a) grid and (b) Langmuir probe . . . . .	129
5.5	Comparison of frequency spectra of floating potential fluctuation signal from Langmuir probe from presheath and bulk plasmas . . . .	129
5.6	The coherence between time series signal from grid and Langmuir probe . . . . .	130
5.7	The phase lag vs. frequency obtained from floating potential fluctuation time series data from grid and Langmuir probe . . . . .	130
5.8	Frequency spectra of floating potential fluctuation signal from grid (1) in Ar-He plasma with $\left(\frac{P_{He}}{P_{Ar}}\right) \sim 18$ (2) in Ar plasma after Helium flow is turned off . . . . .	132
5.9	Variation of amplitude of the peak with partial pressure ratio $\frac{P_{He}}{P_{Ar}} \sim 18, 10, 8$ and $5$ . . . . .	133
5.10	Normalized growth rates calculated for Ar+He plasma, solid line (-) by solving equ 5.2 numerically and dashed line (- -) from approximate growth rate equ 5.4 with $\Delta V = C_{s1} - C_{s2}$ , $T_e = 3$ eV and $n_e = 2 \times 10^9/\text{cc}$ . . . . .	137
5.11	(a) Measured central frequency vs neutral pressure ratio (b) Real frequency obtained theoretically vs ion concentration ratio for different wavenumbers (k) (c) Measured amplitude of the peak vs neutral pressure ratio (d) Normalized maximum growth rate vs ion concentration ratio. . . . .	138

## LIST OF FIGURES

6.1	Growth rate plots of ion-acoustic instability for ion velocity $V_i = 0.9 C_s$ and $T_e/T_i = 100$ . . . . .	146
6.2	Growth rate plots of ion-acoustic instability for different ion velocities in the presheath normalized with Bohm velocity. . . . .	146
6.3	Growth rates for ion-acoustic instability near the sheath edge with different electron to ion temperature ratio ( $T_e/T_i$ ) and ion velocity $V_i = 0.9 C_s$ . $T_e/T_i = 50$ (solid line), 100 (dash-dot line), 200 (dash line), 300 (dotted line), and 400 (dot-dash line) . . . . .	147
6.4	(a) Schematic diagram of the experimental set-up. (b) Cross-sectional view showing surface cusp magnetic field. (c) Circuit diagram for Grid and Langmuir probe. . . . .	149
6.5	Frequency spectra of floating potential fluctuations from grid at a working pressure $5 \times 10^{-4}$ mbar, electron density $n_e = 3 \times 10^8/\text{cc}$ and effective electron temperature $T_e = 8$ eV. . . . .	152
6.6	Phase with respect to frequency between grid and Langmuir probe floating potential fluctuations. . . . .	152
6.7	Coherence between grid and Langmuir probe floating potential fluctuations. . . . .	153
6.8	Power spectra of floating potential fluctuations at electron density $\sim 8 \times 10^7/\text{cc}$ , effective electron temperature $\sim 8$ eV and working pressure (a) $5 \times 10^{-4}$ mbar (b) $5.5 \times 10^{-4}$ mbar (c) $6.5 \times 10^{-4}$ mbar. . . . .	153
6.9	Comparison of power spectra of floating potential fluctuations at electron density $6-8 \times 10^7/\text{cc}$ , effective electron temperature 7-8 eV and discharge currents $I_d = 0.6$ A and 1.0 A . . . . .	154

# List of Tables

2.1	Ar I and Ar II transitions, Energy levels, statistical weight and absorption oscillatory strength . . . . .	59
-----	----------------------------------------------------------------------------------------------------------------	----

# 1

## Introduction

### Introduction to Plasma

Plasma is an ionized gas, consists of charged (electrons and ions) particles satisfying two basic necessary (but not sufficient) properties, (a) presence of freely moving charged particles, and (b) large number of these particles. Plasma also contains neutral (atoms and/or molecules) particles and their relative number would affect the features of the system. The plasma is mainly characterized by ‘collective-behaviour’ originating from the properties of the interaction between its constituent particles. Neutrals as well as charged particles interact by means of electromagnetic interactions. However, the forces between neutrals are short-range force, i.e., a neutral atom does not affect another one until they collide. On the other hand, each charged particle produces a long-range field (Coulomb field), which can affect

## Chapter 1. Introduction

---

many particles located far away from it and visa-versa. Hence collective effects are important for a charged particle gas to be called plasma.

Majority of the universe is in plasma state. Although naturally occurring plasma is rare on Earth (e.g. a lightning strike), there are many man-made plasma examples. In a lightning stroke an oxygen-nitrogen plasma is heated at approximately 20,000 °K, similar to that of a laboratory arc. Although the stroke is only a few centimetres thick and lasts only a fraction of a second. There exists a long list of man-made plasmas such as sparks, arcs, fluorescent lamp, plasma torches, plasma-displays, plasma thrusters, fusion plasmas etc. These natural and man-made plasmas are classified by many characteristics, such as temperature, density, degree of ionization, and approximations of the model describing them. One such classification based on density and temperature of the plasma is shown in Figure 1.1. Because the plasmas are conductive and respond to electric and magnetic fields and can be efficient sources of radiation, they are usable in numerous applications where such control is needed or when special sources of energy or radiation are required. The man-made plasmas are produced and researched for various application ranging from power generation to industrial application and also in medical sciences. One of the important application of plasma is for generating electricity by means of nuclear fusion. It is quite well known that the fusion powers the Sun and the Stars converting matter into energy. In the Sun massive gravitational force creates the right condition for fusion. Fusion devices, based on either magnetic confinement scheme or inertial confinement scheme, aim to generate power from the fusion reactions on Earth [29–32].

Another important application of plasma is in plasma processing of materi-



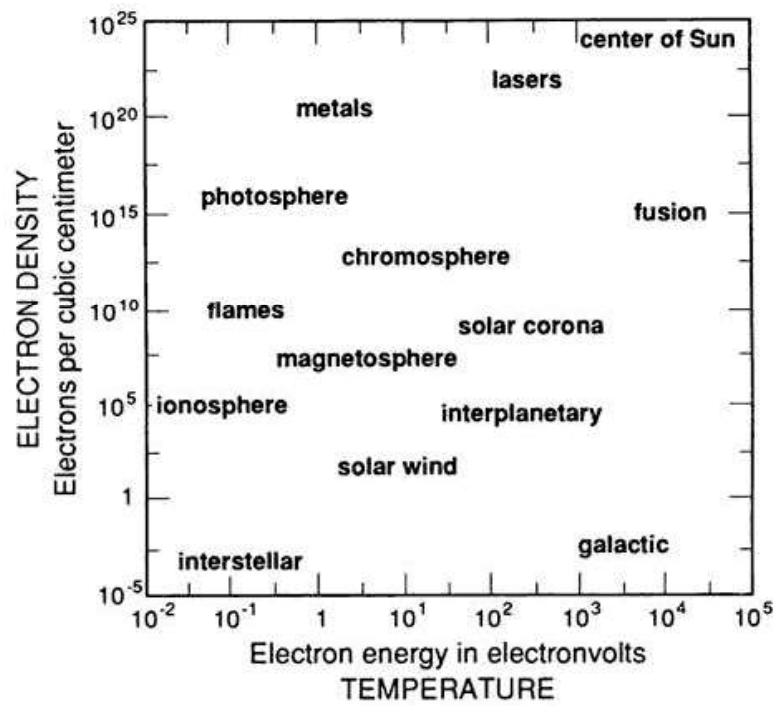


Figure 1.1: The range of density and temperature of plasmas [26]

als [33–35] The chemical and physical properties of the surface of a material can be suitably modified using plasmas of different nature. To name a few, the plasma processing techniques include: Plasma activation, Plasma etching, Plasma surface modification of metals, wool, textile, Plasma polymerization, Plasma cleaning, Plasma electrolytic oxidation, production of nanoparticles etc. [36–43] Plasmas are also used to destroy the solid, liquid and gaseous toxic halogenated and hazardous substances [44] or to generate anti-corrosion, thermal barriers, anti-wear coatings, etc [45, 46]. Furthermore, recently the plasma usages has been extended to biomedical applications. Atmospheric plasma is widely used for sterilization, selective killing of tumor cells, gene transfection, and healing wounds.

In plasma processing as well as in fusion plasmas too, the interaction of plasma with the material surface constitute a subject in itself. Whenever the plasma comes in a contact of a material it forms a thin layer between it and the material surface, known as ‘sheath’. The sheaths play an important role in determining the flux, energy, and type of species incident on the surface. In general, the sheath is ion rich, which confines electrons in, and expels ions from the plasma. The energy that ions gain as they fall through the sheath regulates both the physical and chemical processes that occur at surfaces contacting the plasma. Such plasma-surface interactions are very important in plasma processing mentioned above. The ion sheaths can be collisional or non-collisional depending upon the ion-neutral collisional mean free path compared to the sheath lengths. In collisional sheath, ion collisions can significantly reduce the ion impact energy on the surface. However, in the non-collisional sheaths, the instabilities present in the sheath play an important role in deciding the ion impact on the surface. The experimental observation of

ion-flow driven instabilities in the sheath-presheath region form the subject matter of this thesis work.

## Debye Shielding

The sheath formation is due to the plasma's fundamental characteristics of shielding any electric field present in it. If a positive potential is applied to an object immersed in a plasma, a cloud of electrons surrounds the object and diminishes the effect of positive potential in a very narrow region around the object. This process of shielding is known as Debye Shielding. If the plasma particles are assumed to be cold, i.e., having no temperature, then the shielding is perfect and no potential leaks out of the region of shielding. However, in case of finite temperature, the particles, mainly the electrons in the edge of the electron cloud around the object possess sufficient thermal energy to escape from the electrostatic potential well leading to imperfect shielding. Potential of the order of  $kT_e/e$  can leak into the plasma in this case. Consider a metal grid placed at a position  $x = 0$  and having a potential  $\Phi_0$ .  $\Phi(x)$  be the potential at a distance 'x' from the grid. Assuming an infinite mass ratio  $M/m$  of ions and electrons, the electrons instantaneously react to the applied field whereas the ions do not move and form a stable uniform background of positive charges. The Poisson equation in one-dimension is given by

$$\epsilon_0 \nabla^2 \Phi = \epsilon_0 \frac{d^2 \Phi}{dx^2} = -e(n_i - n_e) \quad (1.1)$$

## Chapter 1. Introduction

---

Let  $n_0 = n_e = n_i$  be the plasma density in the bulk plasma. Electrons follow Boltzmann distribution, so that electron density in the potential is given by

$$n_e = n_0 \exp\left(\frac{e\Phi}{kT_e}\right) \quad (1.2)$$

Substituting  $n_i$  and  $n_e$  in equation 1.1, we have

$$\epsilon_0 \frac{d^2\Phi}{dx^2} = en_0 \left\{ \left[ \exp\left(\frac{e\Phi}{kT_e}\right) - 1 \right] \right\} \quad (1.3)$$

In the region where  $|e\Phi/kT_e| \ll 1$ ,

$$\epsilon_0 \frac{d^2\Phi}{dx^2} = en_0 \left\{ \left[ \left(\frac{e\Phi}{kT_e}\right) + \frac{1}{2} \left(\frac{e\Phi}{kT_e}\right)^2 + \dots \right] \right\} \quad (1.4)$$

Keeping only linear terms, we have

$$\epsilon_0 \frac{d^2\Phi}{dx^2} = \frac{n_0 e^2}{kT_e} \Phi \quad (1.5)$$

Defining

$$\lambda_D = \left( \frac{\epsilon_0 kT_e}{n_0 e^2} \right)^{1/2} \quad (1.6)$$

Equation 1.5 becomes,

$$\lambda_D^2 \frac{d^2\Phi}{dx^2} = \Phi \quad (1.7)$$

whose solution is given by

$$\Phi = \Phi_0 \exp\left(-\frac{|x|}{\lambda_D}\right) \quad (1.8)$$

where,  $\lambda_D$  is called Debye length, is a measure of the shielding distance.

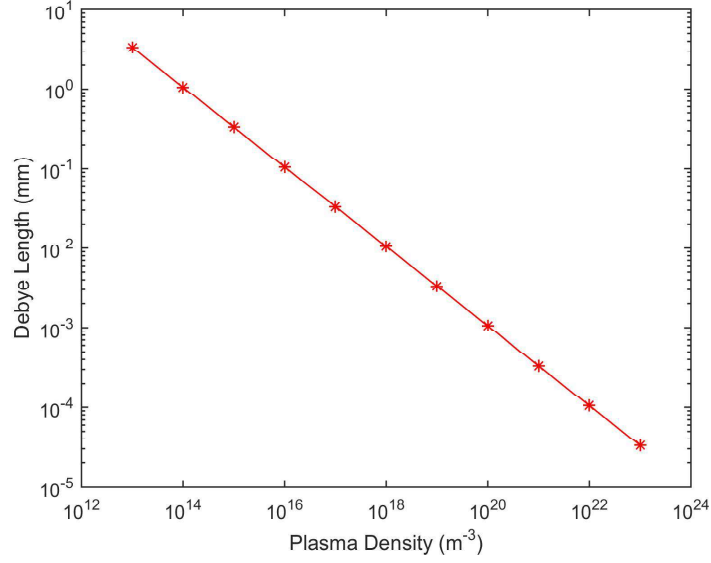


Figure 1.2: Variation of Debye length with plasma density for an electron temperature 2 eV.

If the dimension of the system  $L$  is much larger than Debye length ( $L \gg \lambda_D$ ), then whatever local or external electric potentials arise in the system are shielded within  $\lambda_D$  such that the remaining bulk plasma is free of electric potential. Since the Debye length is inversely proportional to plasma density, the plasma needs to have certain density to satisfy the above. So a criterion for an ionized gas to be a plasma is that it should be dense enough that  $\lambda_D$  is much smaller than  $L$ . Figure 1.2 shows the typical variation of Debye length with plasma density for an electron temperature of 2 eV.

### Sheath-Presheath

In general, any physical surface in contact with plasma gets negative potential because of the high mobility of electrons. This potential is shielded by the positive space charge associated with the ions in a small region of length scale Debye length. This non-neutral region is called ‘Sheath’. The electric field present in the sheath accelerates the ions towards the physical boundary. To have a stable sheath formations, ions needed to be accelerate to a certain minimum velocity  $v \geq \sqrt{kT_e/m_i}$  at the sheath edge, where  $T_e$  is the electron temperature and  $m_i$  is the mass of the ion. Bohm first derived this condition for the ion in the single ion species plasma, called “Bohm criterion”. In general, the equality holds good and ions reach with Bohm velocity at the sheath edge. Ions gain this minimum velocity from the potential drop present in the weak electric field extended regime, so called the ‘Presheath’. The typical potential and density profiles of sheath-presheath regime is as shown in Figure 1.3. Most of the potential is contained in the narrow sheath region and the residual potential is contained in the comparatively broad presheath region. Electron and ion densities start decreasing from entrance of presheath but still quasi-neutral condition holds in the presheath, but in the sheath the quasi-neutrality did not valid anymore.

Particle dynamics in the Sheath-presheath regime defines the interaction of plasma with physical surroundings. These dynamics are very much important in understanding basic phenomena in almost all types of plasmas like low temperature plasmas, space plasmas, tokamak devices, rf and industrial plasmas. The study of particle entry velocities near the sheath edge is a subject as old as plasma physics.

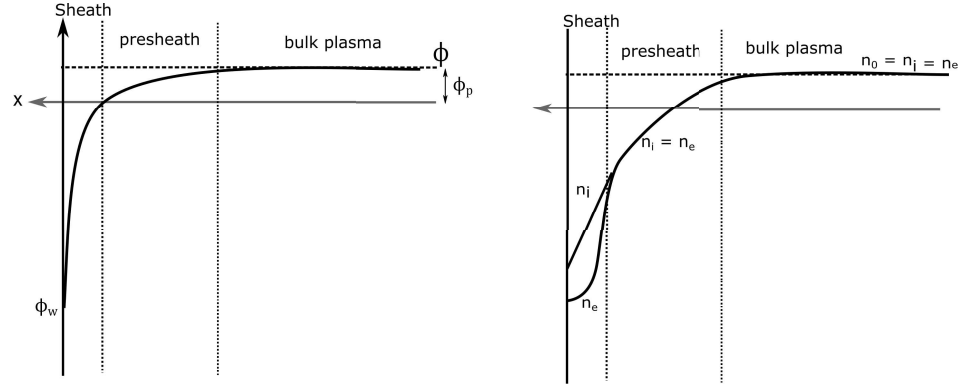


Figure 1.3: Plasma potential and density variation in sheath-presheath region.

Much theoretical and experimental work has been carried out in understanding these velocities in various plasma conditions like unmagnetized plasmas, magnetized plasmas, multi-ion species plasmas, rf plasmas and tokamak plasmas.[47–51]

In case of single-ion species plasma, ions follow Bohm criterion at the sheath edge, however in case of two-ion species plasma, the Bohm criterion is not clear. The subject of entry velocities of the individual ions in case of multi-ion species plasma is under scrutiny. Riemann derived generalized Bohm criterion in case of multi ion-species plasma [1], however this model does not explore the exact values of individual ions entry velocities. The discussion of ion velocities at the sheath edge is made in the later part of this thesis. General condition for sheath stability, sheath potential profile sheath thickness and presheath potential profile are discussed in the next subsequent sections.

### General Sheath Condition for multi-ion species plasma

Consider an unmagnetized plasma system consists of electrons, positive ions and neutrals. The fluid equations for ions gives,

$$\frac{\partial n_i}{\partial t} + \nabla \cdot (n_i v_i) = S_i \quad (1.9)$$

$$m_i \frac{\partial v_i}{\partial t} + m_i v_i \cdot \nabla v_i = e_i \mathbf{E} - \frac{1}{n_i} \nabla p_i - R_i \quad (1.10)$$

where  $m_i$ ,  $n_i$  and  $v_i$  are the mass, density and velocity of the ion component  $i$ .  $\mathbf{E} = -\nabla\Phi$  designates the electric field,  $S_i$  is the source term and  $R_i$  is the friction force.

Sheath defined on the length scale  $\lambda_D$ . For a thin planar sheath in the  $z$ -direction, we can write

$$\nabla = \hat{z} \frac{d}{dz}, \quad (1.11)$$

$$\mathbf{E} = \hat{z} E, \quad (1.12)$$

$$E = -\frac{d\Phi}{dz} \quad (1.13)$$

The sheath potential  $\Phi$  is determined by Poisson's equation

$$\frac{d^2\Phi}{dz^2} = -\frac{\rho}{\varepsilon_0} \quad (1.14)$$



and the boundary condition

$$\Phi \rightarrow 0 \quad \text{for} \quad \frac{z}{\lambda_D} \rightarrow -\infty \quad (1.15)$$

of a decaying wall distortion. This boundary condition defines the sheath edge on the sheath scale and represents the transition to a large plasma scale  $L \gg \lambda_D$ . The space charge density  $\rho$  in the sheath is assumed to be a function of potential  $\Phi$  vanishing at the sheath edge.

Multiplying equation 1.14 with  $\frac{d\Phi}{dz}$ , and integrating yields

$$\varepsilon_0 E^2 + \left( \frac{d\rho}{d\Phi} \right)_{\Phi=0} \Phi^2 = \text{constant} \quad (1.16)$$

For the sheath edge boundary condition,  $\text{constant} = 0$  and from equation 1.16,

$$\left( \frac{d\rho}{d\Phi} \right)_{\Phi=0} \leq 0 \quad (1.17)$$

This condition is the general sheath condition.

Space charge density,

$$\rho = \sum_i e_i n_i - e n_e \quad (1.18)$$

for steady state, collisionless sheath with no extra ionization, ion fluid equations becomes

$$n_i \frac{dv_i}{dz} + v_i \frac{dn_i}{dz} = 0 \quad (1.19)$$

$$m_i v_i \frac{dv_i}{dz} = -e_i \frac{d\Phi}{dz} - \gamma_i k T_i \frac{1}{n_i} \frac{dn_i}{dz} \quad (1.20)$$

## Chapter 1. Introduction

---

Using above two equations we get,

$$\frac{dn_i}{d\Phi} = \frac{n_i e_i}{m_i v_i^2 - \gamma_i k T_i} \quad (1.21)$$

Electrons are assumed to be Boltzmann distributed, then

$$\frac{dn_e}{d\Phi} = \frac{n_e e}{k T_e} \quad (1.22)$$

Equation 1.17 becomes,

$$\sum_i \frac{e_i^2 n_{i0}}{m_i v_{i0}^2 - \gamma_i k T_i} \leq \frac{e^2 n_{e0}}{k T_e} \quad (1.23)$$

This is called Generalized Bohm Criterion, where suffix 0 refers to sheath edge.

If we consider ions are singly ionized to be cold i.e.,  $T_i = 0$ , the above equation becomes

$$\sum_i \frac{n_{i0}}{n_{e0}} \frac{C_{si}^2}{v_i^2} \leq 1 \quad (1.24)$$

where  $C_{si} = \sqrt{\frac{k T_e}{m_i}}$  Bohm velocity of the  $i^{th}$  ion species and the summation is over all ion species. Equation 1.24 is called Bohm criterion for multi ion species plasma.

For two-ion species plasma, the Bohm criterion becomes,

$$\frac{n_1}{n_e} \frac{C_{s1}^2}{v_1^2} + \frac{n_2}{n_e} \frac{C_{s2}^2}{v_2^2} \leq 1 \quad (1.25)$$

Hence, in case of two ion-species plasma, the ion velocities at the sheath edge  $v_1$  and  $v_2$  will satisfy equation 1.25. But this equation does not provide the exact solution of the individual ion species. This topic of entry velocities of ion species

at the sheath edge in two ion-species plasma will be discussed in section 1.4.1.

## Child-Langmuir's Law

In the limit of ion initial energy  $\varepsilon_s$  small compared to the potential in the sheath, the ion energy and flux conservation equations given by,

$$\frac{1}{2}Mv_x^2 = -e\Phi(x) \quad (1.26)$$

$$en(x)v(x) = J_0 \quad (1.27)$$

where  $J_0$  is the constant ion flux.

From the above two equations, we get

$$v_x = \sqrt{\frac{-2e\Phi}{M}} \text{ and} \quad (1.28)$$

$$n(x) = \frac{J_0}{e(-2e\Phi/M)^{1/2}} \quad (1.29)$$

From Poisson equation, (here neglecting electrons)

$$\frac{d^2\Phi}{dx^2} = -\frac{J_0}{\epsilon_0} \left( -\frac{2e\Phi}{M} \right)^{-1/2} \quad (1.30)$$

Multiplying above equation by  $\frac{d\Phi}{dx}$  and integrating from 0 to x, we have

$$\frac{1}{2} \left( \frac{d\Phi}{dx} \right)^2 = 2 \frac{J_0}{\epsilon_0} \left( \frac{2e}{M} \right)^{-1/2} (-\Phi)^{1/2} \quad (1.31)$$

Applying the boundary conditions  $\frac{d\Phi}{dx} = -E = 0$  at  $\Phi = 0$  ( $x = 0$ ) and integrating

again, we get

$$\Phi^{3/4} = \frac{3}{2} \left( \frac{J_0}{\epsilon_0} \right)^{1/2} \left( \frac{2e}{M} \right)^{-1/4} x \quad (1.32)$$

At  $x = s$ ,  $\Phi = -V_0$ , then

$$J_0 = \frac{4}{9} \epsilon_0 \left( \frac{2e}{M} \right)^{1/2} \frac{V_0^{3/2}}{s^2} \quad (1.33)$$

Equation 1.33 is well known as Child's law of space charge limited current in a plane diode. With spacing 's', this formula gives current between two electrodes as a function of potential difference between them. However,  $J_0$  given explicitly as

$$J_0 = en_s C_s \quad (1.34)$$

From above two equations, we get sheath thickness

$$s = \frac{\sqrt{2}}{3} \lambda_{Ds} \left( \frac{2V_0}{T_e} \right)^{3/4} \quad (1.35)$$

where  $\lambda_{Ds}$  is the Debye length at the sheath edge and  $V_0$  is the potential on the wall.

## Presheath potential profile

Riemann provided the constant collision frequency model for a one dimensional weakly ionized plasma in front of a plane absorbing wall.[52] The equations pro-

viding electrostatic potential and ion flow velocity in the presheath are given by

$$\frac{e\Phi}{T_e} = \ln\left(\frac{c_s}{V_i}\right) \quad \text{and} \quad (1.36)$$

$$dz = dV_i \left( \frac{c_s^2 - V_i^2}{V_i^2 \nu^{i-n}} \right) \quad (1.37)$$

where,  $c_s$  is the Bohm velocity,  $V_i$  is the ion velocity and  $\nu$  is the ion-neutral collision frequency.

In the collision model, two special cases has to be evaluate (1) constant collision frequency,  $\nu_c(V_i) = \text{constant} = V_i/l$  and (2) constant mean free path,  $\nu_c(V_i) = V_i/\lambda$ .

For constant collision frequency model, and choose coordinate system where  $z = 0$  is the sheath edge, and  $z$  takes negative values throughout the presheath to a distance  $z = -l = -2\lambda^{i-n}$ . For the constant ion-neutral collision frequency, equations 1.37 yields,

$$\frac{e\Phi}{T_e} = \text{arccosh}(1 - z/l) \quad \text{and} \quad (1.38)$$

$$V_i = c_s \left[ 1 - \frac{z}{l} (1 - \sqrt{1 - 2l/z}) \right] \quad (1.39)$$

Figure 1.4 shows the electrostatic potential and ion flow velocity in the presheath.

## Collisions in Plasma

Particles in plasma interact with themselves through ‘Collisions’. Collisions between charged particles in a plasma differ fundamentally from those between atoms

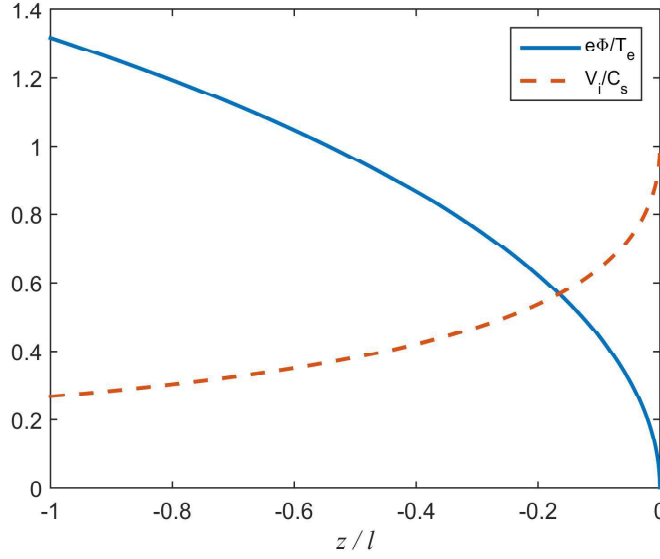


Figure 1.4: The electrostatic potential (blue solid line) and ion flow (red dash line) throughout presheath.

(or molecules) in a neutral gas because of the long range of the Coulomb force. Apart from colliding within themselves, the charged particles also collide with the neutrals present in the plasma. Collisions analysis of plasmas are very important as they describe many phenomena in plasmas such as diffusion, resistivity, ionization, energy equipartition, radiations etc. in and from the plasma.

## Coulomb Collisions

Let consider simple estimation of electron-ion collision frequency. To have a collision, the electrons have to reach to a closest distance ( $b_{ei}$ ) towards ion such that electron thermal energy is of the order of potential energy due to coulomb force

between ion and electron. i.e.,

$$\frac{1}{2}m_e v_{the}^2 \sim T_e \sim \frac{Ze^2}{4\pi\epsilon_0 b_{ei}} \quad (1.40)$$

Hence,

$$b_{ei} \sim \frac{Ze^2}{4\pi\epsilon_0 T_e} \quad (1.41)$$

Thus, electrons at a distance  $b_{ei}$  of ions have a significant collisions with those ions.

Since the electron only notices ions at a distance  $b_{ei}$ , it samples a volume  $\pi b_{ei}^2 \lambda_{ei}$ , where  $\lambda_{ei}$  is the electron-ion collision mean free path. The probability of finding an ion in this volume is unity, so it must satisfy  $n_i \pi b_{ei}^2 \lambda_{ei} \sim 1$ . From this we obtain,

$$\lambda_{ei} \sim \frac{1}{n_i \pi b_{ei}^2} \sim \frac{(4\pi\epsilon_0)^2 T_e^2}{Z^2 e^4 n_i} \quad (1.42)$$

The collision frequency

$$\nu_{ei} \sim \frac{v_{the}}{\lambda_{ei}} \sim \frac{Z^2 e^4 n_i}{(4\pi\epsilon_0)^2 m^{1/2} T_e^{3/2}} \quad (1.43)$$

The effect of weak collisions between the particles separated by Debye length dominated, can be accommodate with Coulomb logarithm, i.e.,

$$\nu_{ei} \sim \frac{Z^2 e^4 n_i \ln \Lambda_{ei}}{(4\pi\epsilon_0)^2 m_e^{1/2} T_e^{3/2}} \quad (1.44)$$

Similarly electron-electron and ion-ion collision frequencies can be obtained,

$$\nu_{ee} \sim \frac{e^4 n_e \ln \Lambda_{ee}}{(4\pi\epsilon_0)^2 m_e^{1/2} T_e^{3/2}} \quad (1.45)$$

and

$$\nu_{ii} \sim \frac{Z^4 e^4 n_i \ln \Lambda_{ii}}{(4\pi\epsilon_0)^2 m_i^{1/2} T_i^{3/2}} \quad (1.46)$$

### Ion-Neutral Collisions

The collisions of the charged particles with neutrals can be elastic or in-elastic in nature. The probability of the collisions can be explained in terms of total effective cross-section. Consider a thin slice of stationary neutral particles with an area  $A$  and thickness  $dx$  with density  $n_g$ . Assume the atoms are simple spheres of cross section area  $\sigma$ . The number of atoms in the slice is given by  $n_g A dx$ .

The fraction of the slice occupied with atoms is

$$\frac{n_g A dx \sigma}{A} = n_g dx \sigma \quad (1.47)$$

Let  $\Gamma_0$  be the incident particle flux, then the flux of particle coming out of slice without collisions is

$$\Gamma(x) = \Gamma_0 (1 - n_g \sigma dx) \quad (1.48)$$

The change in particle flux as the particles passing through slice is given by,

$$\frac{d\Gamma}{dx} = -\Gamma n_g \sigma \quad (1.49)$$

The solution of the above equation is,

$$\Gamma = \Gamma_0 \exp(-n_g \sigma x) = \Gamma_0 \exp\left(-\frac{x}{\lambda}\right) \quad (1.50)$$



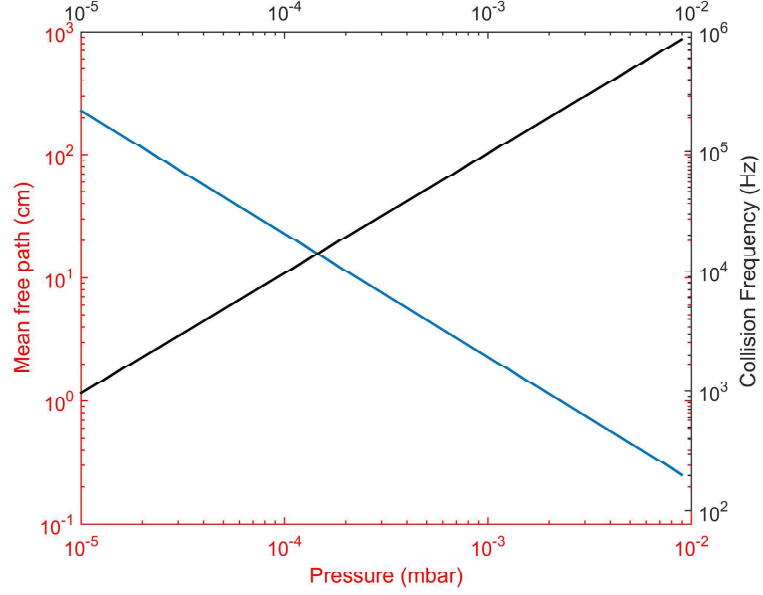


Figure 1.5: ion-neutral mean path and collision frequency at the sheath edge (ion velocity  $\sim$  Bohm velocity) with respect to neutral pressure

where  $\lambda = \frac{1}{n_g \sigma}$  is the collisional mean free path defined as, the distance in which the particle flux would decrease to  $\frac{1}{e}$  of its initial value.

The mean time between two collisions is given by

$$\tau = \frac{1}{n_g \sigma v} \quad (1.51)$$

where  $v$  is the velocity of the particle.

Collisional frequency averaging over all Maxwellian velocities is given by

$$\nu = \frac{1}{\tau} = n_g \sigma \bar{v} \quad (1.52)$$

# Instabilities in Unmagnetized Plasma

A plasma in thermodynamic equilibrium is characterized by homogeneous Maxwellian particle distributions at rest with each other. Deviations of the plasma from such a thermodynamic equilibrium state can be the source of free energy, leading, under certain conditions, to instabilities. The plasma through instability discharges its free energy and will try to retain the equilibrium. In this process, the energy may be converted into different forms such as violent motion of plasma particles, radiations etc. In plasmas such a conversion takes place in collective way and any small deviation from the equilibrium can either grow or lead to further deviations. The rate of these changes are determined by dynamic time scales much faster than the collisional time scales. In this way, a plasma instability can lead to loss of stability through enhanced transport of plasma particles and energy out of the system.

Deviations from thermodynamic equilibrium can arise both in an homogeneous or an inhomogeneous systems. In an homogeneous system, deviations from thermodynamic equilibrium are found in velocity space. The ion-acoustic instability is an example of an instability arising from such a velocity deviation, in this particular case in the form of electrons streaming with respect to ions. Similarly, in multi-species plasmas, the streaming of different ions with respect to each other also can excite instabilities. Furthermore, the Weibel instability is another example, which results from an anisotropic electron velocity distribution. The instabilities of a weakly inhomogeneous plasma with the Maxwellian velocity distribution of particles caused by the density and temperature gradients are often called drift instabilities, and the corresponding types of perturbations are the drift waves. For

example, Rayleigh-Taylor instability can occur when a dense plasma is supported against gravity by the pressure of a magnetic field.

## **Ion-flow driven Instabilities**

Instabilities can be self excited in the sheath-presheath of a low temperature plasma by virtue of different flow velocities between constituent charged particles. The free energy associated with the particle streams will effect the particle transport in this regime, so that the particle fluxes and particle energies to the surface, estimated by the classical models might be changed drastically.

The streaming of ions with differential velocities can cause ion-ion streaming instability and the system is unstable to the instability. These instabilities can be excited when same or different ion species moving in opposite direction and also when different ion species moving in same direction with different velocities. Depending on the direction of ion streams, this instability can be categorized into two types (1) ion-ion counter-streaming instability (2) ion-ion co-streaming instability.

When the instability exists, it can enhance the friction force and anomalous ion heating can take place. This anomalous ion heating by the instability has been extensively studied in space plasma where the differential flow of ion species possible in ionospheric region.[15, 53, 54] The auroral zone is the one of the most prominent region for ion-ion two-stream instability to exist. The ionospheric ions (e.g.,  $H^+$ ,  $He^+$  and  $O^+$ ) can flow with differential speeds by virtue of difference in their mass. The linear theory for ion-ion streaming instability under auroral conditions has been reported by different authors. It is shown that the differential

ion flow can cause instability, which can lead to strong heating of ions with net energy being transferred from lighter ions to heavier ions.

### **Ion-flow driven instabilities in sheath-presheath**

Instabilities in the ‘bulk’, ie., in the main body of the plasma have been studied theoretically and experimentally since several decades. However, recent measurements [23] of ion flow velocities in sheath-presheath region of two ion species, low temperature plasmas using Laser Induced Fluorescence (LIF) led to several theoretical studies regarding the presence of instabilities in the sheath presheath region. Instabilities in this region can be self excited by virtue of different flow velocities between the constituent charged particles. The free energy associated with the particle streams triggers the instabilities which in turn affect the particle transport in this region. This altered particle transport due to these instabilities drastically modify the classical estimations of particle fluxes and energies to the surface around which the sheath is formed. So the conditions to excite, sustain and study these instabilities in the sheath-presheath region and their effects on the dynamics of particles in this region are the subject of recent research.

Due to the significant ion flow speeds in the sheath-presheath regime, these instabilities can also be excited in the plasma sheath-presheath regimes of low temperature plasmas. The effect of these instabilities on the ion dynamics in the sheath-presheath is a very interesting subject because they can control the ion velocities in this regime. Although the subject has been studied theoretically, experimental observations are very rare.

One such instability in the sheath-presheath region namely the ion - ion co

streaming instability has been identified as the cause for resolving the ambiguity related to generalized Bohm Condition in the multi-ion species plasmas. Generalized Bohm criterion in case of multi-ion-species plasma is one of the topic that draw much attention because of its direct practical implications in tokamak, space plasmas and plasma processing plasmas. Generalized Bohm criteria in multi-ion species plasma has been given by Riemann[1] and is expressed as

$$1 \geq \sum_j \frac{n_{j0}/n_{e0} C_j^2}{v_j^2} \quad (1.53)$$

Where  $C_j = \sqrt{kT_e/m_j}$  the ion Bohm speed for each ion species of mass  $m_j$ . The zero subscript refers to the quantities at the presheath-sheath edge. But, the generalized criterion does not give the exact solution for the individual velocities. The most common solutions are either both ions reach the sheath edge with equal velocities or they reach with their individual Bohm velocities. Franklin and Gudmundsson showed that, each ions reach the sheath-presheath edge with their individual Bohm speed.[55, 56] Some other experiments showing, both ions reach the sheath-presheath edge with common sound speed for nearly equal ion concentrations [56–59]. The reason to attain equal velocity instead of individual Bohm speeds is explained by enhanced collision friction between ions due to ion-ion two stream instability.[11, 60] This strong friction is reduces the relative velocity between the species.

Similar to the co-streaming instability, ion-ion counter streaming instability can also be excited in the sheath-presheath region in case of similar or different ion species moving in the opposite directions. This instability can exists in the sheath-presheath region produced around a transparent grid placed inside the plasma and

also in cases when ions are reflected back from the sheath potential well [7, 61]. Apart from these co and counter streaming instabilities, ion-acoustic instability can also be excited in the presheath region. Having a much weaker growth rate compared to the streaming instabilities, the excitation of ion-acoustic instability in the presheath region is very sensitive to the experimental conditions and the ion-neutral collisions.

## Motivation and Previous work

In this thesis work, ion-flow driven instabilities in the sheath-presheath region of mesh grid immersed in a weakly collisional low temperature plasma are studied experimentally. Three main instabilities present in the sheath presheath region such as ion-ion counter streaming instability, ion-ion co streaming instability and ion-acoustic instability are identified, characterized and compared to the theoretically derived dispersion relations. Although, all these instabilities are predicted, simulated and studied theoretically, experimental observations of these instabilities in sheath-presheath region are next to none. As mentioned earlier, the plasma sheaths are characteristics of all bounded plasmas, formed near the boundary, and the knowledge of flow speed of ions is important in a broad range of plasma applications from fusion plasmas to plasma processing to space plasmas to plasma diagnostics. In single ion species plasma, several experimental measurements of ion flow velocity near the sheath-presheath boundary confirmed the Bohm criterion to be valid. However, in case of multiple ion-species plasma, the generalized Bohm criterion becomes ambiguous and does not provide a unique solution for determining the flow speeds of each ion species at the sheath boundary. Most plasmas used

for industrial applications as well as Scrape-of-Layer (SOL) plasmas of magnetic fusion devices, consist of more than one ion species. Hence, extensive experimental, theoretical and simulation studies have been carried out to understand the flow of ions in the region where they exit a quasi-neutral plasma and enter into a non-neutral sheath in weakly collisional plasmas containing two ion species.

The contest of flow speeds of the ion species in the sheath-presheath regime in case of multi-ion species plasma has been receiving attention since 1980's. The first experimental measurement of ion flow speeds at the sheath edge using LIF technique in two-ion species (Ar+He) plasma has been presented by Severn *et al* in 2003 [23]. In this experiments, diode Laser based Laser Induced Fluorescence (LIF) diagnostics with Ar scheme has been used for Argon ion velocity distribution function (IVDF) measurements. The experimental results shows Ar ions reach the sheath edge with velocity exceeding their Bohm velocity and almost reaches with system sound speed. These results are contradict earlier predictions that ions reach sheath edge with individual Bohm velocities and hence opens the discussion about ion flow velocities at the sheath edge. Later, Lee *et al.*, measured velocities of both Argon and Xenon using two different Lasers in Ar+Xe plasma in 2007 [62]. The results shows both ion species reaches the sheath edge with velocity equal to system sound speed. Baalrud proposes a theory that this could be a consequence of ion-ion collision friction enhanced by ion-ion two stream (co-stream) instability [8]. The theory also finds that the difference in ion velocity at the sheath edge also depends on relative ion concentration. Baalrud concluded that both ion species reach the sheath edge with equal velocities when both ion concentrations are nearly equal and ion reaches with their individual Bohm velocities when the

difference in concentrations is large. Hershkowitz et al. [63], performed experiments to test Baalrud's theory by varying concentration of Argon from 5% to 90% and the results are found to be in good agreement with the theory. But in 2011, Gudmundsson performed particle-in-cell Monte Carlo simulations to study  $Ar^+$  and  $Xe^+$  velocities near the sheath edge [64]. They find that the ions reach the sheath edge with their individual Bohm velocities and find no evidence of any instability in the simulations, which is proposed mechanism for common system speed by Baalrud. The discrepancy is resolved later by Baalrud *et al* in 2015 [9] by showing that a critical temperature ratio is required for the instability to have positive growth rate using exact numerical solution of the dispersion relation. They have shown that the temperature ratio in the PIC-MCC simulations of Gudmundsson *et al* fall below the threshold. Baalrud et al further confirmed the presence of ion-ion co streaming instability near the sheath edge by carrying out PIC-MCC simulations [R] when the threshold  $\left(\frac{T_e}{T_i}\right)$  is satisfied. The theory suggests, two stream instabilities arise when the differential ion flow speed exceeds a threshold condition :  $V_1 - V_2 > \Delta V_c$ . The electric field present in the presheath accelerates the lighter species to faster speed and causes differential flow. The resultant instability enhanced friction rapidly becomes so strong that  $\Delta V$  cannot significantly exceeds  $\Delta V_c$ . Using condition provided by  $\Delta V = \Delta V_c$  and generalized Bohm criterion, the speed of each ion species at the sheath edge is uniquely determined [60]. Although theoretically predicted and confirmed with simulations, the instability has not been unambiguously measured experimentally. Observed peaks in the MHz frequency range in the frequency spectra of ion saturation current to a negatively biased cylindrical probe has been attributed to ion-ion streaming



instabilities [8, 65] in Argon + Helium two ion specie plasma. This frequency of the instability has been found to be increasing with the addition of Argon to a Helium plasma. And as this increasing behaviour is found consistent with the theoretical prediction, the instability is believed to be due to ion-ion co-streaming instability. Direct experimental observation of ion-ion co-streaming instability in the presheath region still remained a challenging problem. In this thesis, direct measurement of ion-ion co-streaming instability in the presheath region of a mesh grid immersed in two ion specie plasma has been reported for the first time. The wavenumber of the identified ion-ion co-streaming instability has been measured which matched quite well with the calculated one from the dispersion relation. The instability is excited only in case of nearly equal ion concentration of Ar<sup>+</sup> and He<sup>+</sup> and fades away when the concentration ratio deviates from unity. This experimentally verifies the predominant condition for the instability to excite at equal concentrations of both ion specie in two-ion specie plasmas.

Ion-ion counter streaming instability comes under the same category of ion-ion streaming instabilities in which ions move in opposite directions of each other. In case of sheath-presheath produced around a mesh grid immersed in a low temperature weakly ionised plasmas, the counter flow of ions from both sides of the grid results in ion-ion counter streaming instabilities in the presheath region on either side of the mesh grid. Nakamura et al first reported this instability in the presheath of a grid separating the source and diffusion chambers in a double plasma device with a single ion species plasma. To the best of our knowledge, this work is the only direct experimental measurement of ion-ion counter streaming instability. In this thesis, detailed experimental studies of ion-ion counter streaming instability

in the presheath-sheath region on either side of a floating mesh grid immersed in a filament-produced low temperature, low pressure Ar, He, and Ar + He plasmas has been carried out. Again, to the best of our knowledge, the observations of ion-ion counter streaming instability in plasmas produced with different gases as well as with gas mixtures are reported for the first time. This instability has been identified as the ion-ion counter streaming instability as it ceases to exist when the mesh grid is covered with a thin metal foil from one side, which restricts the counter streaming of the ions. Further, the wavenumber,  $k$ , of the wave is measured experimentally, which matches quite well with the calculated one from the dispersion relation of ion-ion counter streaming instability. Unlike the observations of Nakamura *et al* [7], the instability has been observed even when the mesh is kept floating inside the plasma, i.e., no biasing of the grid is required to excite the instability and the effect of biasing the mesh in both polarities has also being studied in detail. The effect of this instability on the particle dynamics inside the sheath-presheath region has not been explored much. Very recently Yip *et al* [61] reported ion velocity-locking in the neighborhood of virtual cathode. The locking has been observed in presence of counter streaming of ions. They argued that the locking is due to enhanced collision friction by ion-ion counter streaming instability.

Ion-acoustic instability has also been observed and studied in presheath-sheath region of the mesh grid immersed in weakly ionized single-ion species plasma. Ion-acoustic instability, excited due to differential drift flows between electrons and ions, is quite well known in the bulk plasmas and have been studied by various authors both experimentally and theoretically. It can be excited in the presheath

formed in low temperature, low pressure plasmas and is theoretically predicted to thermalize the ion velocity distribution function near the sheath edge [9, 66]. Langmuir's paradox, i.e., rapid thermalization of electrons to Maxwellian distribution in a low pressure plasma are thought to be due to enhanced electron-electron scattering in the presheath through ion-acoustic instability induced collisions [67]. It can also cause anomalous particle transport in the plasma boundaries. Ion-acoustic waves are launched in the bulk plasma and their characteristics are studied at the sheath boundary by Oksuz *et al* [68]. In this thesis, direct experimental observations of self excited ion-acoustic instability in presheath region is presented. A very narrow region of plasma parameters are identified where this instability has been found to be existing. The instability is found to be critically dependent on the ion-neutral collisions.

## Organization of the thesis

The remaining chapters in this thesis are organized as follows.

### **Chapter-2: Experimental set-up and Diagnostics**

In this chapter, detailed description of the experimental device, diagnostics used in the study, analysis techniques and plasma characterizations are presented.

### **Chapter-3: Identification fo Sheath-presheath boundaries**

In this chapter, detailed description of Current-heated emissive probe and Laser-heated emissive probe is presented along with the advantages of measuring plasma potential using Laser-heated probe in the presence of strong electric fields. The Sheath and presheath boundaries also been identified using spatial potential profile.

### **Chapter-4: Ion-ion counter streaming instability in the presheath of single-ion species and two-ion species plasmas**

Ion-ion counter streaming instability excited in the presheath of a mesh grid immersed in single-ion species as well as two-ion species plasma has been studied. The measured wave number ( $k$ ) of the excited wave is compared with the unstable wave numbers derived using fluid model.

### **Chapter-5: Ion-ion co-streaming instability in the presheath of two-ion species plasmas**

Ion-ion co-streaming instability by the parallel flow of different ion species in the presheath of two-ion species plasma has been studied experimentally. The conditions to excite the instability has been explored. The wave number and phase velocity of the excited wave are experimentally measured and reported for the first time.

### **Chapter-6: Self-excited ion-acoustic instability in the presheath of single-ion species plasmas**

Self-excited ion-acoustic instability in the presheath of single-ion species plasma by virtue of differential flow between ions and electrons has been studied. The wave number and phase velocity of the excited wave are measured. The pressure regime in which the instability sustain in the plasma discharge has been identified. The neutral pressure damping of the instability is studied which shows the instability is much sensitive to the ion-neutral collisions.

### **Chapter-7: Conclusions and Future work**

Conclusions of the thesis work and future work that can be carried for further investigation are presented in this final chapter.

# 2

## Experimental Set-up and Diagnostics

In this chapter, experimental set-up has been described in detail including plasma production and diagnostics. Hot-cathode filament discharge phenomena used for plasma production in this study has been explained. Plasma characterization by Langmuir probe and optical emission spectroscopy methods is presented and plasma floating potential fluctuation measurement and analysis techniques of Fast Fourier Technique has been discussed.

### Experiment Set-up

Experiments are carried in a compatible cylindrical device, made with stainless steel material having length of 50 cm and inner diameter 20 cm, whose schematic diagram and picture are as shown in Figures 2.1 and 2.2 respectively. Plasma discharge is created by hot-cathode filament discharge method. Two tungsten filaments of length 5 cm and diameter 0.25 mm are placed at the one end of the chamber. These filaments are heated by passing high electric current through them and get emitting electrons by thermionic process. These thermionic emitted electrons are accelerated by negative bias to the filaments with respect to grounded chamber. These energetic electrons ionize the neutrals and initiate the discharge. Before plasma initiation, the chamber is evacuated to a base pressure of  $6 \times 10^{-6}$  mbar using Turbo molecular pump back up by rotary pump. The chamber is equipped with total 10 number 25KF ports to introduce probes, gas insertion, pressure gauges and filament holders etc. The chamber also has a large view port on the top to accomplish spectroscopy diagnostics. The pressure in the discharge chamber is monitored by hot-cathode ionization gauge. To improve the plasma confinement, the inner surface of the chamber is aligned with permanent NdFeB magnets. The alternative rows of south and north pole faces produce cusp magnetic field along the inner surface. The magnetic field strength on the surface of the magnets is  $\sim 2$  kG. The strength of the magnetic field decreases rapidly away from magnetic rows and decreases up to few gauss within 5 cm. So the plasma at centre region of the chamber is considered to be unmagnetized. The primary electron loss to the wall is restricted by this magnetic field, which increases the ionization and

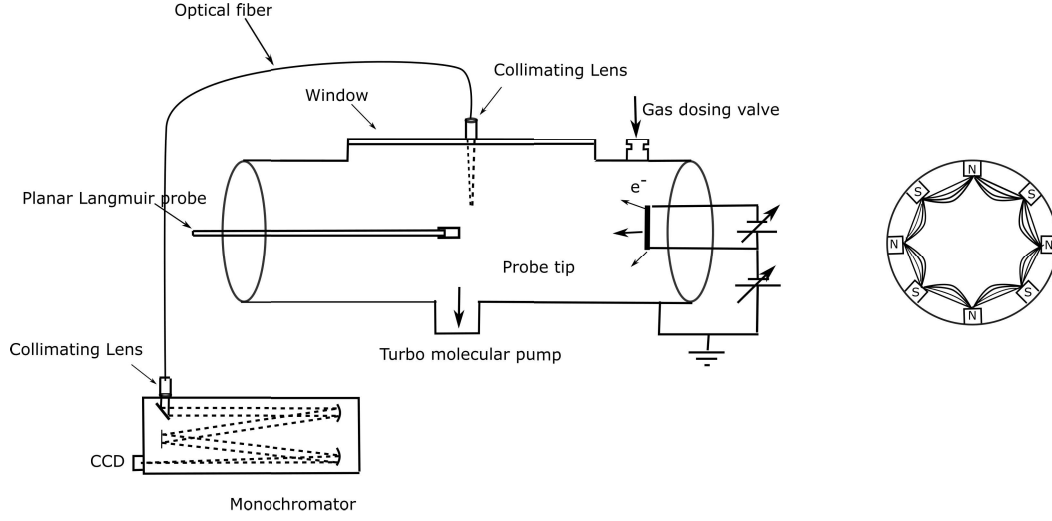


Figure 2.1: Schematic diagram of the experimental chamber.

hence density of the plasma. Total 14 rows of magnets with alternative north and south poles are arranged. The schematic of the surface magnetic field is as shown in Figure 2.1.

Plasma of different gases (Ar, He ) and mixture of gases (Ar+He) is produced in the system. For controlled gas feeding, two mass flow controllers (MFC) has been used. The pressure in the discharge chamber has been monitored with mass flow rate of individual gases. When a mixture of gases used in the experiments, the flow rates measured has been used to know partial pressure ratios. Figure 2.3 shows the mass flow rate versus neutral pressure for Argon and Helium gases.

For plasma parameters measurement probe diagnostics as well as spectroscopy diagnostics have been employed. Cylindrical Langmuir probes is used to measure plasma fluctuations from bulk as well as sheath-presheath regions. A planar Langmuir probe is also employed to measure electron density, temperature and electron energy distribution function. For sheath-presheath potential profile measurement,

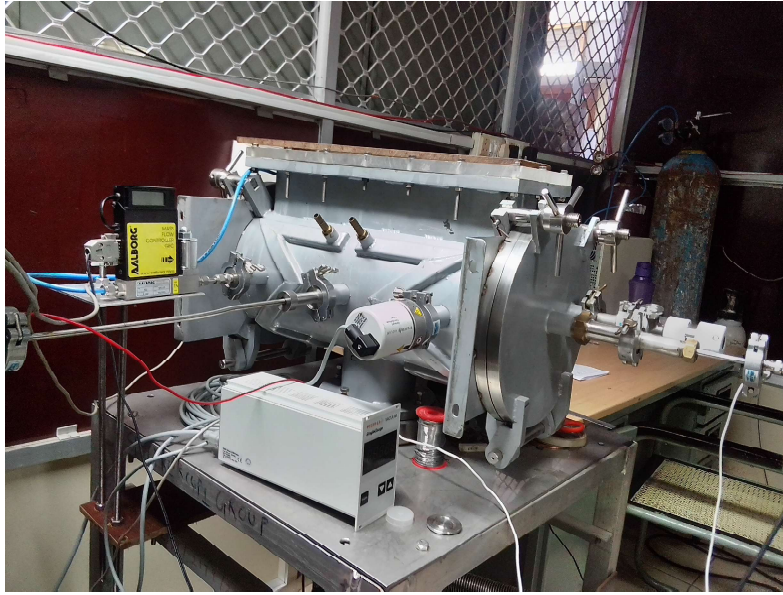


Figure 2.2: Picture of the experimental set-up.

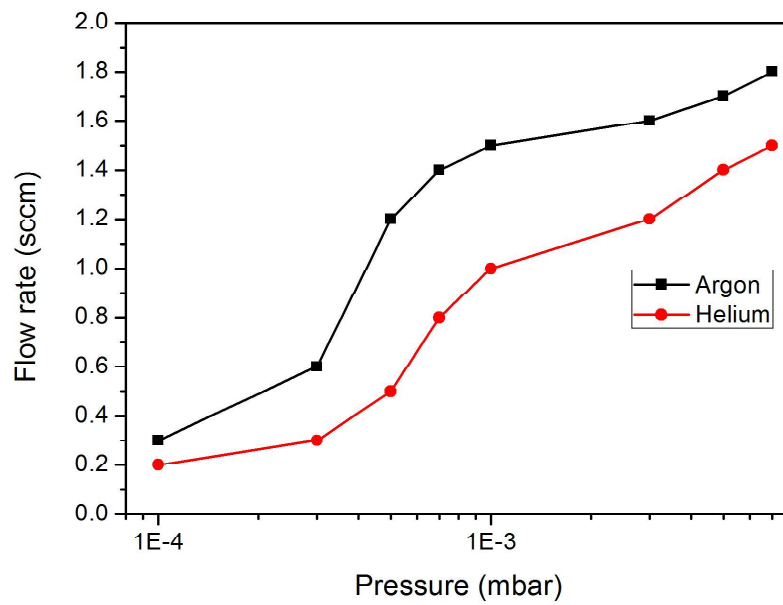


Figure 2.3: The variation of neutral pressure in the chamber with gas flow rate for Argon and Helium.



accurate plasma potential measurement is needed, and for the same, Emissive probes have been used. In this study, two different types of emissive probes studied namely, (1) current-heated emissive probe and (2) Laser-heated emissive probe. The detailed description of the emissive probes and the advantages of using Laser-heated emissive probe over conventional emissive probe is discussed in Chapter 3.

For optical emission spectroscopy measurements, two different spectrometers has been used. One is a miniature spectrometer of wavelength range 300 - 950 nm and optical resolution  $\sim 1$  nm. This spectrometer is able to cover the entire visible region and useful for identification of strong lines from the plasma with lower resolution. Another one is a high resolution monochromator with wavelength scanning length of 20 nm at a time. The high optical resolution of 0.02 nm (maximum) with CCD detector is used for detailed study of electron temperature measurement using line ratio method.

## Filament Discharge Plasma

Hot-filament discharges are widely used to generate collisionless and weakly collisional discharges for a variety of experiments in basic plasma physics. It is well known Plasma with densities in the range  $10^7 - 10^9$  /cc can be generated in the filament discharges. Electron impact ionization process is the major mechanism of ionization in these discharges. An electron with sufficient kinetic energy can ionize the neutrals depends on the ionization cross-section of that particular species.

$$e_{fast}^- + A = A^+ + e_{slow}^- + e_{slow}^- \quad (2.1)$$

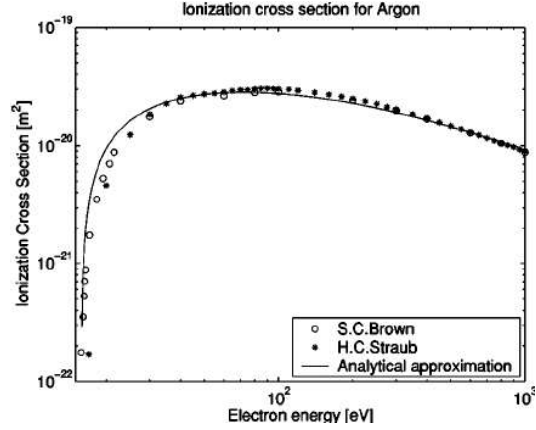


Figure 2.4: Electron-impact ionization cross-section for Argon[27].

Ionization cross section of the species defines the range of electron energy where the ionization will be maximum. Figure 2.4 shows ionization cross-section for neutral Argon[69], which shows ionization is maximum for the electron energy range 60-80 eV. Tungsten filaments has been heated to high temperatures by passing direct current through them. Primary electrons will be emitted from the surface of the filaments by thermionic process. Tungsten is one of the good material as a thermal electron emitter because of its high melting point 3683 K. The emitted electron current density is limited by the space charge. The saturation current density  $J_{max}$  is obtained from Richardson-Dushman equation,

$$J_{max} = A_0 T^2 \exp(-e\phi/kT) \quad (2.2)$$

where  $A_0$  is the Dushman's constant ( $1.2 \times 10^6 A/m^2 deg^2$ ) These electrons are accelerated by a dc electric field towards the surface of the chamber, which serves as anode. These accelerated primary electrons causing the ionization of neutrals, re-

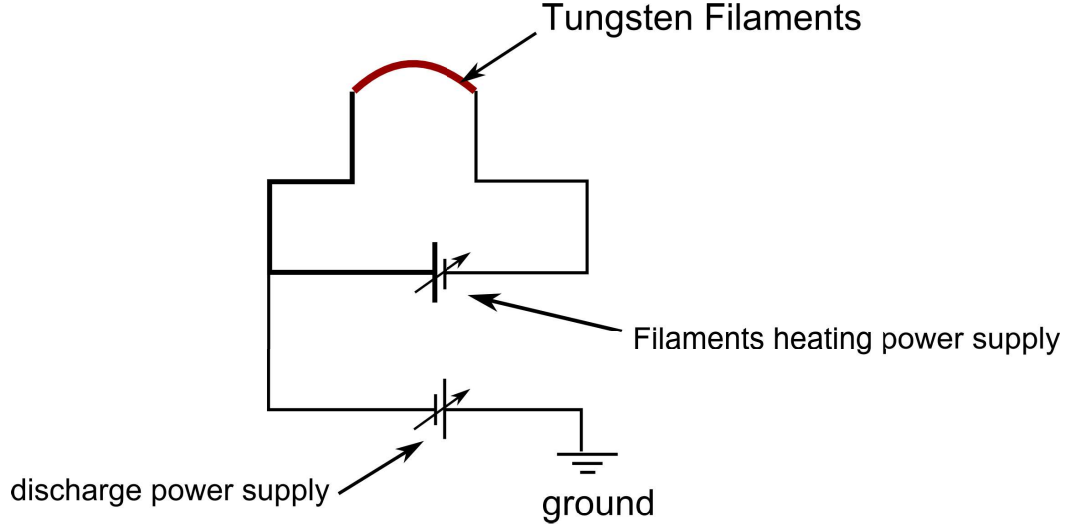


Figure 2.5: Schematic diagram of the circuit for plasma discharge.

sulting plasma ignition. The circuit diagram for the filament discharge is as shown in Figure 2.5. The Maxwellian group of electron can also play significant role in the ionization. The tail part of the Maxwellian electrons have sufficient energy to sustain ionization. Figure 2.6 shows rate coefficients for Argon with respect to different electron temperature. From Figure 2.6, it is clear that the Maxwellian electrons with temperature greater than 2-3 eV can participate in the ionization of Argon.

For many of the plasma applications and basic study, a low electron temperature and high plasma density discharge is desired. In the hot-filament discharges, electrons can be categorized into (1) primaries from the filaments, (2) the secondaries from the ionization of neutral gas, and (3) secondary electrons from walls. Electron temperature estimation from the first principle using particle and energy balance is not perfect in this discharge because, many processes like heating by secondary electrons from wall and heating by primary electrons can affect the par-

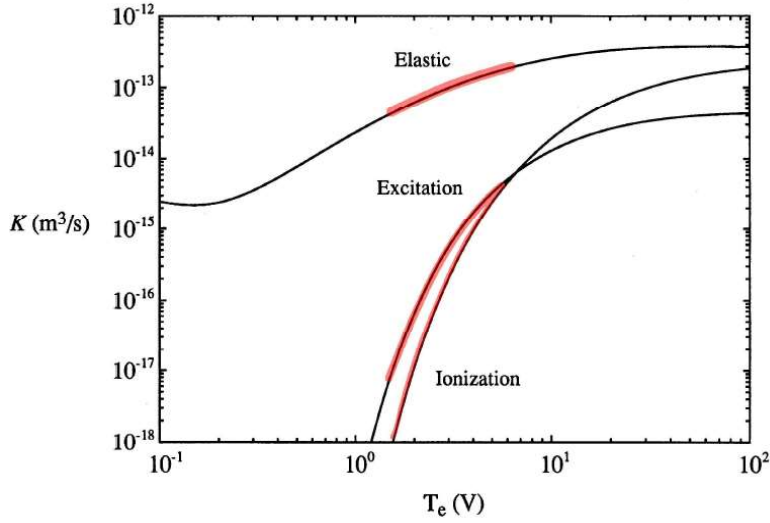


Figure 2.6: Electron impact rate coefficients for Argon[28].

ticle and energy balance.[70] The primary electrons are the energetic electrons from the filaments that creates the plasma by ionizing the neutral gas. The electrons which have high enough energy that can not participate in the ionization collisions more than one time. So they do not loose much energy to become Maxwellian and are known as mono energetic. Electrons from the ionization of neutrals (plasma electrons) can be divided into two types. One having energy less that  $e\Phi$ , where  $e\Phi$  is the potential drop in the sheath at near the chamber wall. These electrons do not cross the potential barrier at the wall and becomes confined. Another group of electrons having energy greater than  $e\Phi$  can cross the potential barrier at the wall and get lost to the chamber wall. The secondary electrons from the wall have energy distribution with a width of approximately 10-15 eV . These electron energy can be controlled by using inner wall material having low secondary electron emission coefficient.[71] In these experiments, the filament heating current used

for plasma production is in the range of 5 - 6 A through each filament. Discharge voltages are operated in 50-80 V. Filling pressures are operated in the range of  $3 \times 10^{-4}$  -  $5 \times 10^{-3}$  mbar. Plasma densities and electron temperature produced in the range of  $5 \times 10^7$  -  $5 \times 10^9$  /cc and 3-8 eV respectively.

## Plasma Parameters Measurement

Langmuir probe is one of the oldest and effective diagnostic tool widely used for measurement of plasma parameters since they were introduced by Langmuir in the 1920s [72]. In general, Langmuir probe is a small metal electrode inserted into a plasma and measures the response probe current with respect to applied varying bias voltage around floating potential. Plasma parameters can be estimated by analyzing current-voltage (I-V) characteristics [73]. This simplicity of design and operation establish the Langmuir probe as a fundamental tool in most of the plasma discharges for estimation of local plasma parameters. From Probe I-V characteristics, electron temperature, electron density, electron distribution function, floating potential and plasma potential can be estimated.

For accurate plasma potential measurement hot-Langmuir probe known as ‘Emissive probes’ are used. The working principle and details of the probe are presented in Chapter 3.

On the other hand the measurement of electron temperature with noninvasive method is also attractive for many plasma applications. Plasma processing systems are often used to generate reactive species for film growth. In such systems, a small concentration of metallic impurities can lead to the formation of defects in the lattice, which strongly affects quality of the films. Hence metallic probes are

not desirable in these systems. [74] Noninvasive methods are also access in limited plasma devices such as tokamaks, stellarators and space propulsion systems [75–78]. In this thesis work, spectral line intensity ratio method proposed first time by Cunningham [79] has been used to estimate electron temperature. The light from the plasma is collected by fibers. Emission spectra of Argon ions and Argon neutrals are recorded by dispersing the light through spectrometer.

### Langmuir Probe Theory

As mentioned earlier, the Langmuir probe is a simple and reliable tool for estimation of Plasma parameters electron and ion densities, electron temperature and energy distribution function and plasma potential. It consist of a bare metal wire or a metal disk that is biased with a variable power supply with respect to a reference electrode. Although the construction and operation of Langmuir probe is simple, analysis of the I-V traces to obtain the plasma parameters is not straight forward.

The potential at which the net current drawn by the probe is zero, is called Floating potential. Any isolated object placed in the plasma attains this potential. In this case, total flux of electron and ions reaching the object are equal. When applied postitive bias with respect to floating potential, the electron current starts increasing and ion current decreases. The electron current increases exponentially up to plasma potential, if the electron velocity distribution is Maxwellian (generally this is the case). When bias voltage is much higher than plasma potential, the electron current comes to saturation beacuse of the shielding effects. When negative bias is applied with respect to floating potential, ions start attact towards

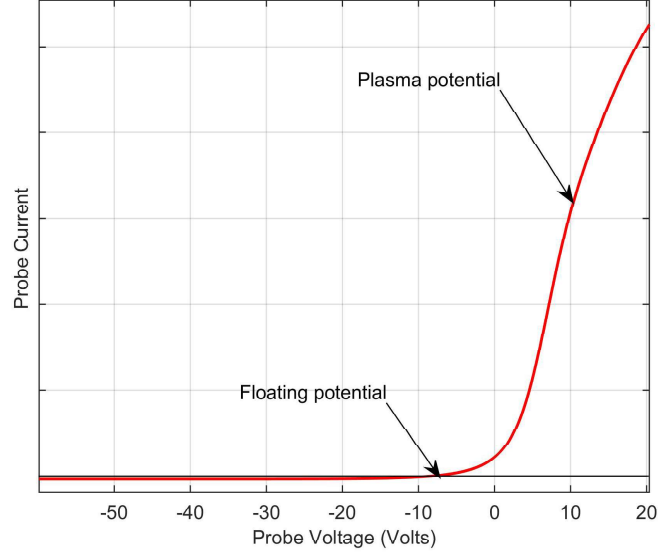


Figure 2.7: Typical I-V characteristics of Langmuir probe

the probe and electrons repelled. The ion current comes to saturation at high negative bias. So the ideal I-V characteristics of Langmuir probe placed inside plasma looks similar to that in Figure 2.7. However, this electron and ion currents will not saturate in practical situations. Because of the sheath effects, the electron and ion saturation currents tends to increase with the bias voltage. These effects are discussed in 2.3.2

### **Electron Flux**

The effects of the collisions develop a distribution of velocities for each species. On the average and in the absence of other external forces, the particles will then move with a velocity that is solely a function of macroscopic temperature and mass of that species. The charged particles therefore can be described by velocity

## Chapter 2. Experimental Set-up and Diagnostics

---

distribution function, usually it is Maxwellian velocity distribution function which is a most probable distribution of velocities for a group of particles in thermal equilibrium.

In one dimension, the Maxwellian velocity distribution function is

$$f(v) = \sqrt{\frac{m}{2\pi kT}} \exp\left(\frac{-mv^2}{2kT}\right) \quad (2.3)$$

The average velocity of the particles becomes

$$\langle v \rangle = \sqrt{\frac{8kT}{\pi m}} \quad (2.4)$$

The flux of particle in one dimension (say z-direction) for the Maxwellian distribution of particle velocities is given by  $n\langle v \rangle$ . In this case average of particle velocity taken over positive z-direction only. The particle flux is then

$$\Gamma_z = \int n v_z f(v) d^3v \quad (2.5)$$

which can be evaluated by integrating the velocities in spherical coordinates with the velocity volume element given by

$$d^3v = v^2 dv d\Omega = v^2 dv \sin\theta d\theta d\phi \quad (2.6)$$

where  $d\Omega$  represents element of the solid angle. If the incident velocity has cosine distribution, the one sided flux (*normal flux*) is



$$\Gamma_z = n \left( \frac{m}{3\pi kT} \right)^{3/2} \int d\phi \int \sin\theta d\theta \int v \cos\theta \exp(-v^2/v_{th}^2) v^2 dv \quad (2.7)$$

which gives

$$\Gamma_z = \frac{1}{4} n \langle v \rangle = \frac{1}{4} n \sqrt{\frac{8kT}{\pi m}} \quad (2.8)$$

### **ion flux**

In low temperature plasmas, ions are relatively cold in temperature with respect to electrons. Because the energy transferred to the ions by the collision of electrons is very small in fraction so that ions comes to the equilibrium at lower temperatures. Therefore the plasma in general is described as containing Maxwellian electrons and cold ions with high electron to ion temperature ratio. As a result the velocity of the ions and their fluxes at the boundaries tend to be determined by the electric fields generated at the plasma interface to conserve charge, and is different from the electron flux derived above.

The ion flux depends on the ion Bohm velocities at the ion-sheath edge and effective sheath area combined with probe area. Ion current can be written as

$$I_i = n_s e v_i A \quad (2.9)$$

where  $n_s$  is the density at the sheath-presheath boundary,  $A$  is the effective ion collection area at the sheath boundary and  $v_i$  is the ion velocity at the sheath edge (bohm velocity). This current is called Bohm current.

## Chapter 2. Experimental Set-up and Diagnostics

---

The potential at the sheath edge fallen to a value  $\left(\frac{-kT_e}{2e}\right)$  relative to bulk plasma potential. The electron density at the sheath edge is (where it follows Boltzmann distribution)

$$n_s = n_0 \exp\left(\frac{e\phi_0}{kT_e}\right) = n_0 \exp\left(\frac{e\frac{-kT_e}{2e}}{kT_e}\right) = 0.6n_0 \quad (2.10)$$

Velocity of the ions at the sheath edge is

$$v_i = \sqrt{kT_e/M} \quad (2.11)$$

When the potential is large compared to the electron temperature,  $(\phi \gg kT_e/e)$ , the majority of the electrons repelled over the sheath thickness. This means electron density essentially goes to zero relatively to the sheath edge, and the electron space charge does not significantly affect the sheath thickness. Such sheaths are called Child - Langmuir sheaths. The ion current follows Child - Langmuir law.

$$J_i = \frac{4\epsilon}{9} \sqrt{\frac{2e}{M}} \left( \frac{V^{3/2}}{d^2} \right) \quad (2.12)$$

This states that ion current per unit area that can pass through a planar sheath is limited by space charges and is proportional to the voltage power 3/2 divided by square of the sheath thickness.

### Electron Current

- For bias voltage  $V_B \ll V_p$ , all the electrons are repelled by the probe and electron current  $I_e=0$ .

- For bias voltage  $V_B < V_p$ , the electrons are partially repelled by the probe and for a maxwellian velocity distribution, current decreases exponentially with decrease in bias voltage.
- For  $V_B > V_p$ , the potential is shielded by the plasma and the electron current is saturated.

The electron saturation current is given by

$$I_{es} = \frac{1}{4} n_e e \sqrt{\frac{8kT_e}{\pi m}} A \quad (2.13)$$

When the bias voltage less than plasma potential, this saturation current will decreases exponentially

$$I_e = I_{es} \exp [-e (V_P - V_B) / kT_e] \quad (2.14)$$

The electron current as a function of  $V_B$  can be represented as

$$I_e(V_B) = \begin{cases} I_{es} \exp [-e (V_P - V_B) / kT_e] & \text{if } V_B \leq V_P \\ I_{es} & \text{if } V_B > V_P \end{cases} \quad (2.15)$$

### The Ion current

- For  $V_B \gg V_P$ , all the positive ions are repelled by the probe potential and ion current becomes zero.
- For  $V_B \ll V_P$ , the probe collects ion saturation current  $I_{is}$ .

## Chapter 2. Experimental Set-up and Diagnostics

---

- The ion current decreases as we increase the positive potential and ions tend to repel when we cross the plasma potential.

The ion current  $I_i(V_B)$  can be written as

$$I_i(V_B) = \begin{cases} -I_{is} \exp[e(V_P - V_B)/kT_i] & \text{if } V_B \geq V_P \\ -I_{is} & \text{if } V_B < V_P \end{cases} \quad (2.16)$$

When  $T_i \equiv T_e$ ,

$$I_{is} = \frac{1}{4} n_i e \sqrt{\frac{8kT_i}{\pi M}} A \quad (2.17)$$

When  $T_i \ll T_e$ ,

$$I_{is} = 0.6 n_i e \sqrt{\frac{kT_e}{M}} A \quad (2.18)$$

### Relation between $V_f$ and $V_P$

Floating potential is the bias voltage at which  $I_e(V_f) + I_i(V_f) = 0$

$$I_{es} \exp[-e(V_P - V_f)/kT_e] = 0.6 n_i e \sqrt{\frac{kT_e}{M}} A, \text{ (since } V_f < V_P \text{)} \quad (2.19)$$

It gives

$$V_f = V_P + (kT_e/e) \ln \left( 0.6 \sqrt{\frac{2\pi m}{M}} \right) \quad (2.20)$$

For Argon plasma,

$$V_f = V_P - 4.04 (kT_e/e) \quad (2.21)$$

For Helium plasma,

$$V_f = V_P - 5.19 (kT_e/e) \quad (2.22)$$

### **Sheath effects**

Plasma density can be estimated from electron saturation current or ion saturation current. However, these measurement of plasma electron density or ion density from the saturation currents can yields enormous errors. This is because the Langmuir probe I-V characteristics never saturates. The current drawn by the probe increases continously at high bias voltages as sheath produced around the probe expands. Hence accurate estimation of saturation currents is vital in determining the plasma particle density.

In most of the practical situations (even in Maxwellian electrons), identifying the plasma potential (at which electron current saturates) by classical procedure results significant errors, becuase of the smooth transition in the electron current near the plasma potential, which can result errors as high as one order in plasma density estimation. The plasma potential found by differnetiation  $I_p(V)$  gives precise plasma potential value corresponding to the maximum of  $dI_p/dV$  or  $d^2I_p/dV^2 = 0$ . The presence of hot electrons and magnetic fields further complicates the estimation of accurate electron saturation current and hence generally it is not suggested to estimate the plasma electron density using electron saturation current [80].

The use of ion saturation current for ion density measurement is better as the errors in estimating the ion saturation current are less. However, the expansion of sheath will not make the probe current saturates. For planar probes, in medium dense plasma the extrapolation of probe current at high neagative bias to the plasma potential gives reasonably good estimation of ion saturation currents and hence ion density. If the expansion of ion curent is non-linear, the extrapolation

technique does not provide accurate results. In this case cylindrical Langmuir probe has advantages such as, definite theory describing the sheath expansion and thus ion current expansion; it is possible to use small area probes and thus reduce the effects due to depletion of low-energy electrons [81].

### Fitting Experimental Data

As mentioned earlier, the theory of probes is not as simple as the probe construction. Many extensive reviews of the probe theory can be found in the literature. [82–84] Even for ideal case, much care needed to be taken on analysis of I-V traces. The current collected by the probe is intrinsically noisy, as the plasmas in themselves are a significant source of noise. First and second derivative of I-V traces are needed for plasma potential estimation and EEDF respectively. Performing first and second derivative operations on raw data including the noise will give erroneous results since the noise get amplified by the derivative process. Several techniques developed for this purpose, such as applying probe current to an analog double differentiating circuit; [85, 86] performing numerical differentiation after digital smoothing [87, 88] and use of a differentiating ac signal superimposed on the dc probe bias voltage. [89, 90] The another way of doing is, make analytic fit to the I-V characteristics and deduce the plasma parameters using fitting parameters.

An empirical equation that fits single Langmuir probe I-V characteristics is given by, [91]

$$I = \exp \left[ a_1 \tanh \left( \frac{V + a_2}{a_3} \right) \right] + a_4 \quad (2.23)$$

where  $V$  and  $I$  are the probe bias voltage and probe current, respectively, and

$a_1, a_2, a_3, a_4$  are fitting parameters. In case of two electron temperature plasma, to accommodate slight change of slope, Eq. (2.23) can be modified as, [92]

$$I = \exp \left[ a_1 \tanh \left( \frac{V + a_2}{a_3} \right) \right] + a_4 + \exp \left[ a_5 \tanh \left( \frac{V + a_6}{a_7} \right) \right] + a_8 \quad (2.24)$$

Plasma parameters are estimated using the fitting parameters. A software package in MATLAB language [93], modified according to two electron temperature plasma is employed for data analysis. Probe I-V data and initial guess fitting parameters are inputs to this program and outputs are ion saturation current, electron saturation current, floating potential, plasma potential, plasma electron temperatures, and the normalized EEDF.

## Langmuir probe Experimental Results

Typical Langmuir probe I-V trace at discharge current 0.65 A, discharge voltage 60 V and neutral pressure  $1 \times 10^{-3}$  mbar is shown in Figure 2.8. The solid lines in the plot is the result of fit to the experimental data with Equation 2.24. The empirical fits are differentiated twice to get second derivative and EEDF and are plotted in Figs. 2.10 and 2.11 respectively. EEDFs for different working pressures at a discharge current 650mA and discharge voltage 60 V are plotted in Figure 2.12.

The presence of two temperature electrons is clearly evident from Figure 2.9. The area under the EEDF curve gives the electron number density of each compo-

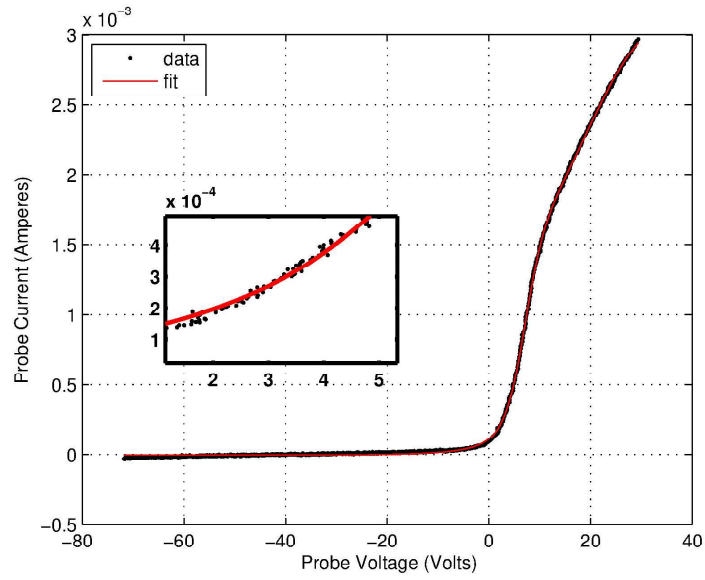


Figure 2.8: Langmuir probe I-V trace. Solid line is the analytic fit for the experimental data

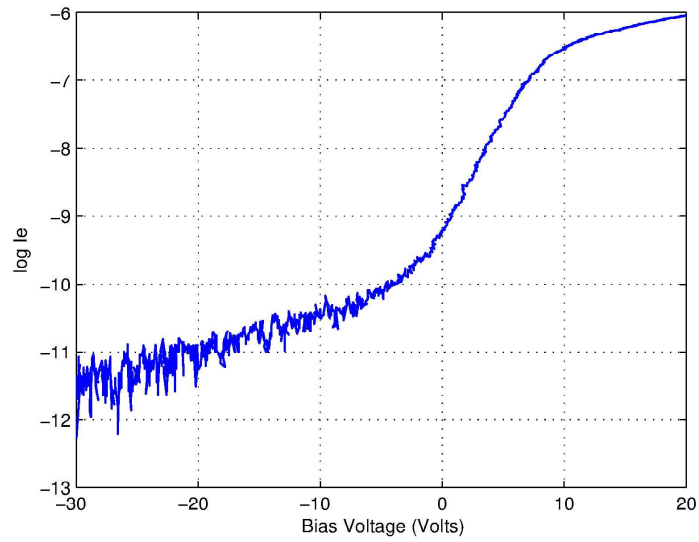


Figure 2.9: Plot of logarithm of electron current vs bias current of the raw experimental data shows two populated electrons



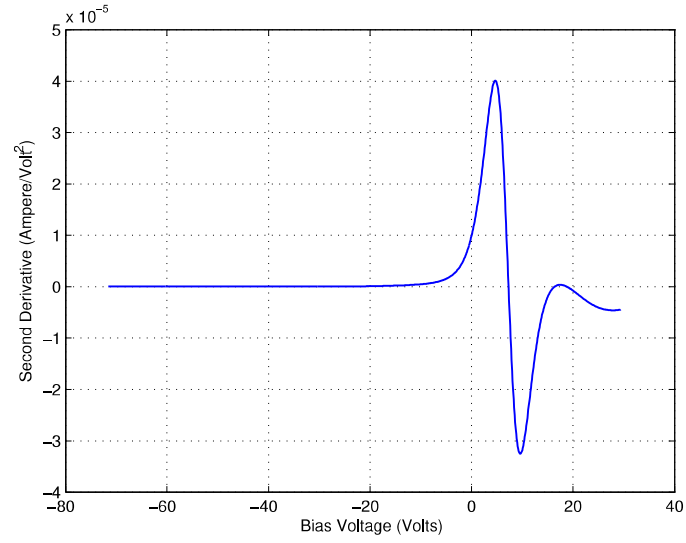


Figure 2.10: Second derivative of the fit

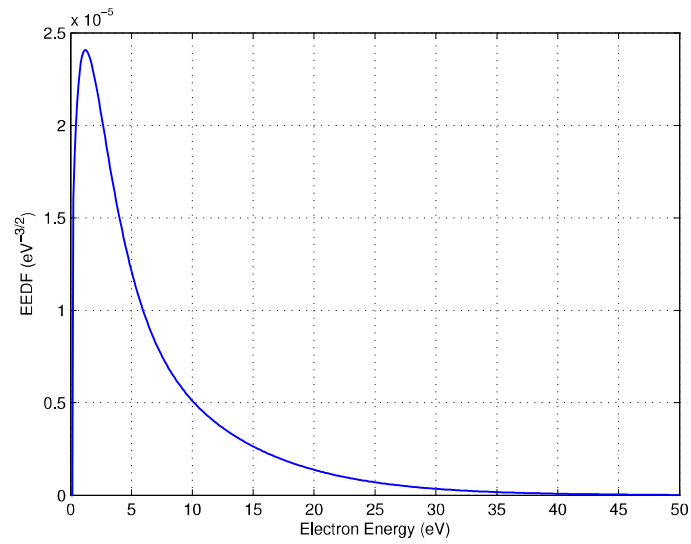


Figure 2.11: EEDF obtained from fit to the experimental data

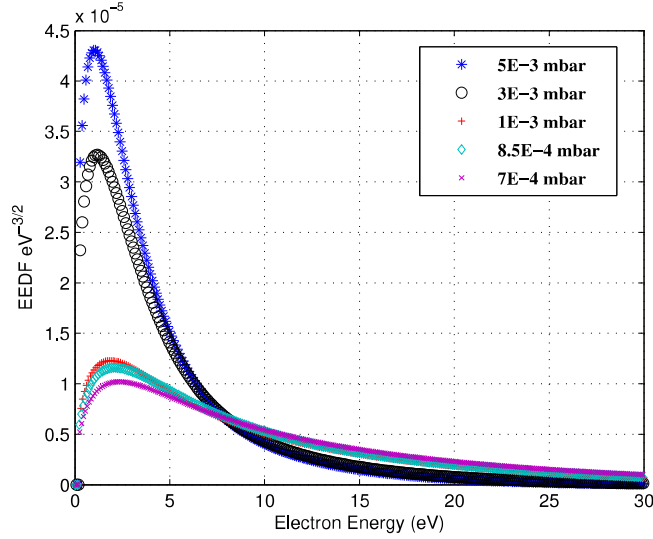


Figure 2.12: Variation of the Distribution function with working pressure

nent. The effective electron temperatures are calculated using  $T_e = \frac{2}{3} \int E f(E) dE$  where  $f(E)$  is the EEDF and  $E$  is the energy. Numerical trapezoidal is implemented in the software program for this purpose.

The variation of the second derivative with filling pressure is shown in Figure 2.12. As neutral pressure increases, more primary electrons participate in the inelastic collisions with neutrals with higher energy loss, which results to reduce the hot electron temperature. Figure 2.13 and 2.14 are the plots showing variation of plasma density and electron temperature with plasma neutral pressure at a fixed discharge current ( $I_d$ ) 0.8A and discharge voltage ( $V_d$ ) 60V. Plasma density increases with increasing neutral pressure and the effective electron temperature decreases.

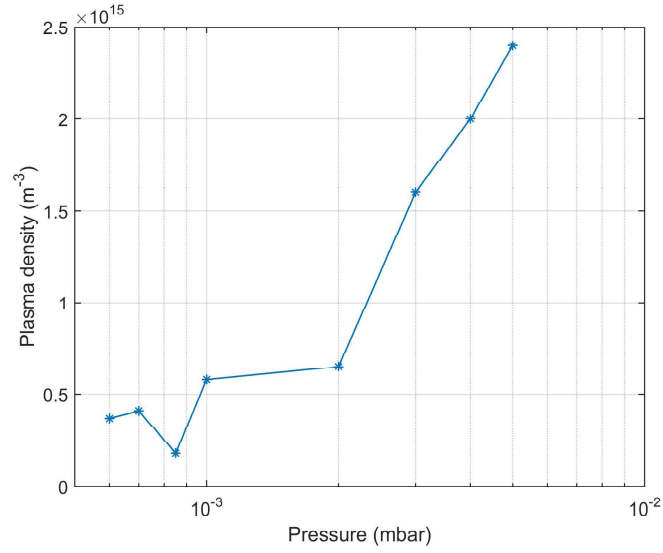


Figure 2.13: Variation of the plasma density with working pressure at discharge current ( $I_d$ ) = 0.8 A and discharge voltage ( $V_d$ ) = 60V.

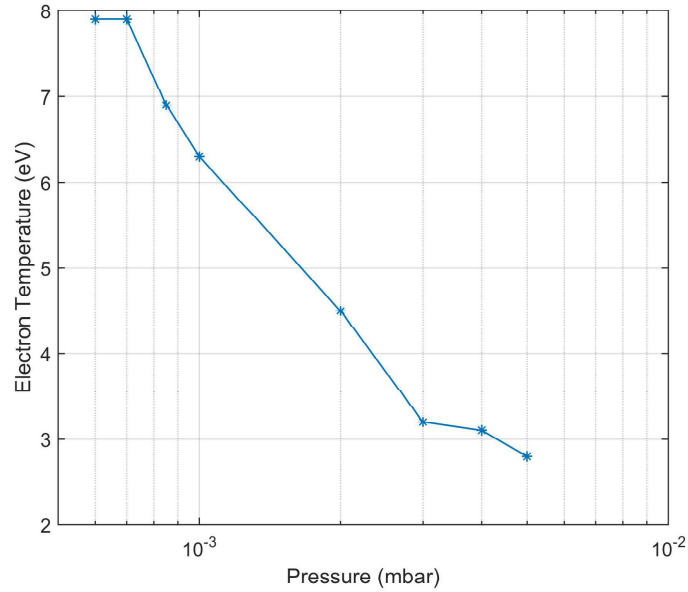


Figure 2.14: Variation of the effective electron temperature with working pressure at discharge current ( $I_d$ ) = 0.8 A and discharge voltage ( $V_d$ ) = 60V.

### Line Ratio Method

Spectroscopy methods are one of most reliable non-invasive diagnostics in plasmas. Early spectroscopy diagnostics in plasmas were implemented in Astrophysics to characterize space plasmas. Later on these non-invasive techniques are implemented to characterize different plasmas such as glow discharge plasma, filament produced plasmas, thermal plasmas, Radio frequency (RF) plasmas, high pressure plasmas, magnetized plasmas etc. Optical emission spectroscopy is the passive spectroscopy method which is based on the measurement of the optical emission radiated from plasma which is a characteristic of the species present in the plasma. Unlike electrical probes, spectroscopic measurements gives line of sight averaged measurements instead of local measurements.

The relationship between observed spectral line intensities and the electron temperature provides estimation of electron temperature. The popular models[94, 95] which gives the relation between line intensity and electron temperature are (i) Local-thermal equilibrium model (ii) Collisional radiative model (iii) Coronal Model. The criterion of the applicability of these models depends on the plasma density. In this thesis work, Corona model with relative line intensities have been used to estimate the electron temperature in low density plasmas, which is valid for plasma density less than  $10^{11}cm^{-3}$ . The two main important processes considered in corona model is the collisional excitation and spontaneous de-excitation. The accuracy of the model is decided on the available accurate data of the cross sections.

The Steady-state corona model was first introduced by R.v.d.r. Woolley to describe spectrum of the low density solar corona plasma. The basic assumption

in this model is at very low electron density, the collisions are so weak such that radiative decay dominates over the electron impact collisional de-excitation. As a consequence, depopulation of upper levels is dominated by radiative decay, whereas the population of upper levels is always by electron impact collisions. The basic assumptions on which this model developed are: (i) free electrons assumes Maxwellian velocity distribution (ii) ion and neutral temperatures are less than or equal to electron temperature (iii) plasma is optically thin to its own radiation.

The corona model is generally applicable for electron temperatures greater than  $10^4$  K. However, the model is not applicable for higher densities ( $n_e > 10^{11} \text{ cm}^{-3}$ ). This corona model assumes the balance between collisional ionization and radiative recombination, given by

$$n_e N_g^z S_g^z = n_e N_g^{z+1} \alpha_g^{z+1} \quad (2.25)$$

where  $n_e$  is the electron density;  $N_g^z, N_g^{z+1}$  is the population of ground levels in the charge states  $z$  and  $z+1$ ;  $S_g^z$  is the collisional ionization rate coefficient from the ground level;  $\alpha_g^{z+1}$  is the radiative recombination rate coefficient from the ground state of the next ionic stage. The empirical formula for these rate coefficients is given by

$$S_g^z = 2.34 \times 10^{-7} \frac{\zeta T_e^{1/4}}{X(z, g)^{7/4}} \exp\left(-\frac{X(z, g)}{kT_e}\right) \quad (2.26)$$

where  $\zeta$  is the number of outer electrons,  $T_e$  is in  $^{\circ}\text{K}$ , and  $X$  is in eV.

For the radiative recombination coefficient,

$$\alpha_g^{z+1} = \frac{2.05 \times 10^{-12} X(z, g)}{T_e^{1/2}} \quad (2.27)$$

From Eqs. (2.25), (2.26) and (2.27); the steady state ratio between consecutive

ions in a corona model plasma can be represented as,

$$\frac{n_g^z}{n_g^{z+1}} = \frac{\alpha_g^{z+1}}{S_g^z} = 8.77 \times 10^{-6} \frac{\zeta X(z, g)^{11/4}}{T_e^{3/4}} \exp\left(\frac{X(z, g)}{kT_e}\right) \quad (2.28)$$

The corona model also assumes that the dominant process in populating upper levels is Electron impact collisional excitation, which is balanced by spontaneous radiative decay. For an ionic charge  $z$ , it is given by

$$n_e N_g^z X_{gp}^z = N_p^z \sum_{q < p} A_{pq} \quad (2.29)$$

where  $X_{gp}^z$  is the excitation rate coefficient from ground level to the excited level  $p$  in the ionic charge  $z$ ,  $A_{pq}$  is the spontaneous radiative decay from level  $p$  to  $q$ , which is sum over all the levels lower than  $p$ . Therefore, the intensity ratio of two lines from same ionic charge is given by

$$\frac{I(\lambda_{ji})}{I(\lambda_{nm})} = \frac{1}{F_R} \frac{X_{gj}^z}{X_{gn}^z} \frac{B_{ji}}{B_{nm}} \quad (2.30)$$

where  $B$  is the branching ratio ( $A_{ji}/\sum_{q < j} A_{jq}$ ) which is a fraction of probability of transition to the particular level from level  $j$  to the total transition probability from level  $j$ .

There are number of experimental and theoretical data is available for excitation rate coefficients. The simple, efficient empirical formula for excitation rate coefficients is give by Rogemorter,

$$X_{ji} = 2\pi\alpha c a_0^2 \frac{1}{\omega_i} \left[ \frac{I_H}{kT_e} \right]^{1/2} \gamma_{ji} \exp\left(-\frac{\Delta E_{ij}}{kT_e}\right) \quad (2.31)$$

The distribution of electrons among the various energy levels depends mainly upon the two processes; collisions among the particles and radiative processes. These distributions give their contribution to the intensity of the spectral line. There are three models that can define their distribution.

The ratio of two line intensity is expressed in the form

$$\frac{I'}{I} = \frac{f'g'\lambda^3}{fg\lambda^3} \exp\left(\frac{E'_\infty - E' - E_\infty + E}{kT_e}\right) \frac{S}{\alpha} \quad (2.32)$$

After substituting S and  $\alpha$ , we get

$$kT_e = \left[ 7.87 \times 10^{-9} E_\infty'^{\frac{11}{4}} \left\{ \frac{fg\lambda'^3 I'}{f'g'\lambda^3 I} \right\} \exp\left(\frac{E_\infty + E' - E}{kT_e}\right) \right]^{\frac{4}{3}} \quad (2.33)$$

## Line ratio method Experimental Results

For the measurement of electron temperature using line ratio method, we have to choose a pair of spectral lines whose intensity is a function of electron temperature. The accuracy of the method is good when we choose two lines which has difference between transitions energy levels is large enough. For this purpose, argon neutral (ArI) spectral lines of wavelength 415.9 nm and 420.1 nm; Ar ion (ArII) spectral line of wavelength 434.8 nm are recorded. Figs. 2.15 and 2.16 show the emission spectrum of argon plasma for central wavelength 420.1 nm and 434.8 nm respectively. The central wavelength is at 1052 pixel in all the spectral data.

The variation of cold, hot components temperatures and effective electron temperature measured using Langmuir probe and Line intensity ratio method are demonstrated in Fig. 2.17. As the neutral pressure increases at a discharge cur-

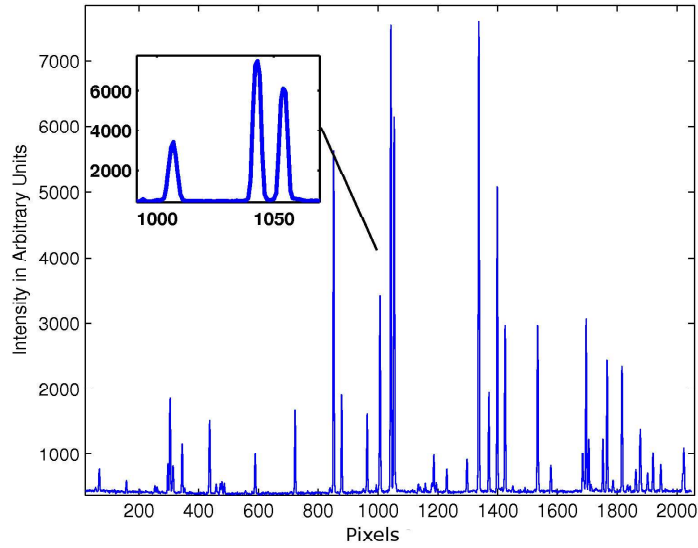


Figure 2.15: Emission spectra of Argon plasma at central wavelength 420nm

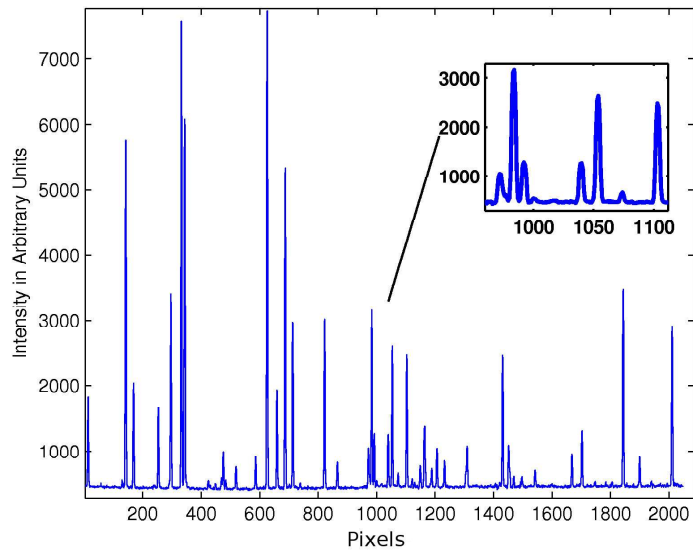


Figure 2.16: Emission spectra of Argon plasma at central wavelength 434nm



$\lambda$ (nm)	Transition	E(eV)	g	f
415.8 (ArI)	50	14.53	5	0.00363
420.1 (ArI)	47	14.5	7	0.00358
425.9 (ArI)	31	14.74	1	0.00361
427.7 (ArII)	35	21.35	4	0.443
434.8 (ArII)	45	19.49	8	0.15

Table 2.1: Ar I and Ar II transitions, Energy levels, statistical weight and absorption oscillatory strength

rent 0.8 A and discharge voltage 60 V, the hot components temperatures decreases showing the effect of energy transfer by inelastic collisions. But there is no significant change in the cold components temperatures. The effective temperature measured by Langmuir probe technique is well in agreement with the temperature measurements by Line ratio method in low pressure region, however the deviation in the results more in high pressure regime. This might be because of the non-consideration of collisional effects in the coronal model in this study.

## Plasma Fluctuations Measurement and Analysis

The adequate diagnosis of fluctuating quantities in plasma such as floating potential, density etc are very important in order to detect and analyze waves and oscillations present in plasma.

The power spectral density of any fluctuating signal can be obtained by discrete Fourier transform of the time series. In general, the fluctuation time series never meets periodic boundary condition. This results in a feature known as "Gibbs phenomenon", which refers to the partial sum of the Fourier series at a point where the function is discontinuous [96]. The spectrum seems to have a significant noise

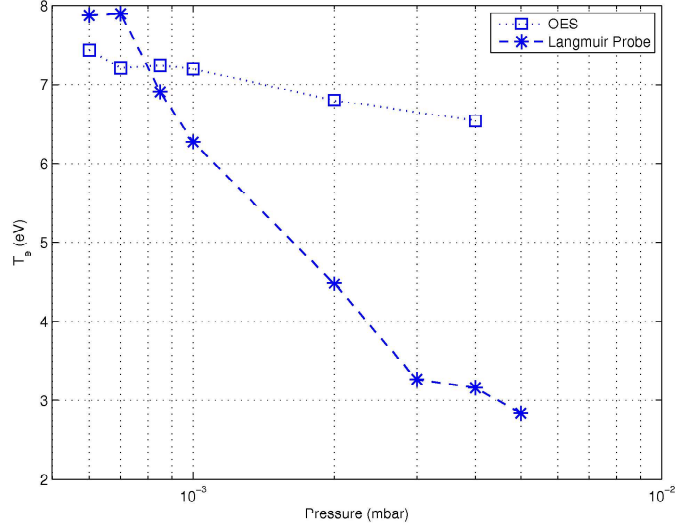


Figure 2.17: Electron temperature vs working pressure for a discharge current of 800 mA

level superimposed to the actual spectrum. Figure 2.18(a) shows power spectrum of fluctuation data sampled at 1MHz.

The standard solution is simply to average a number of power spectra in Fourier space, which cancels out the (phase uncorrelated) Gibbs side lobes. For that, the time series is split into overlap or non-overlap segments called bins. It is also appropriate to weight each partition by a window function. This method was first introduced by Welch [96]. The method is based on the concept of using periodogram spectrum estimates, which are the results of converting a signal from time domain to the frequency domain. Figure 2.18(b) shows the power spectrum of the same time series data using Welch's method. This plot clearly shows the spectrum without any noise. In this method the noise is reduced with sacrificing the frequency resolution.

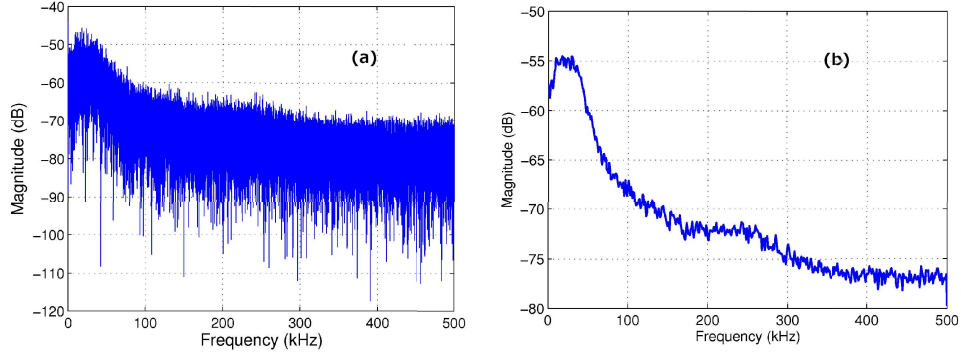


Figure 2.18: Power spectrum of the fluctuation data (a) with noise (b) with reduced noise using Welch method

If an arbitrary signal is sampled at a rate (sampling frequency) equal to  $f_s$  over an acquisition time  $T$ , with total samples acquired  $N$ , then the relation becomes,  $T = \frac{N}{f_s}$ . The frequency resolution of the FFT spectrum given by,

$$df = \frac{1}{T} = \frac{f_s}{N} \quad (2.34)$$

Let  $N = 50000$  and  $f_s = 1\text{MHz}$  then  $T = 50\text{ ms}$  and  $df = 20\text{ Hz}$ . If total samples are divided into windows each of length 500 then frequency resolution becomes  $df = 2\text{ kHz}$ .

The simple power spectrum provides useful information about how the signal energy is distributed over a frequency range. If two time series data is available, from measurements of same quantity at different points in space, the phase information is of utmost importance. Suppose  $x(t)$  and  $y(t)$  are the two independent signals and  $\hat{x}(\omega)$  and  $\hat{y}(\omega)$  are the Fourier transforms of the bins of the respective time series then cross-power spectrum between two signals defined as  $H_{xy}(\omega) = \langle \hat{x}(\omega) \cdot \hat{y}^*(\omega) \rangle$ , gives the phase and coherence between the signals with

## Chapter 2. Experimental Set-up and Diagnostics

---

respect to frequencies and cross phase defined as  $\Theta_{xy}(\omega) = \arg(H)$ , gives the phase angle with respect to frequency.

In this thesis work, floating potential fluctuation measurement using Langmuir probe and Grid has been carried for identifying instabilities.

First of all, the basic requirements of oscilloscope for adequate measurements of fluctuations, should be taken into account. As the instabilities studied in this thesis are governed by ion phenomena, the expected frequencies of the instabilities are few times less than ion plasma frequency. i.e., for the plasma used in these studies, the plasma densities are in the range  $\sim 1 \times 10^8 - 5 \times 10^9$  /cc, and the corresponding ion plasma frequencies are  $\sim 0.3$  MHz - 2 MHz. The expected frequencies of ion-flow driven instabilities in the presheath are in the range of tens of kHz to  $\sim 500$  kHz. Therefore, band width required for the oscilloscope should be in few MHz range. For wave number measurement, simultaneous fluctuation data from atleast two locations are required so at least two input channels are required on the oscilloscope. As shown in Figure 2.18 the power spectra noise can be reduced with increasing averages. Better frequency spectra can be obtained by increasing total number of samples. Depending on these considerations, Keysight make InfiniiVision DSO-X 2024A model oscilloscope, (Figure 2.19) has been used for data acquisition. It is a Digital Storage Oscilloscope with high band width and high sample rate. The oscilloscope has 200 MHz band width, 1 M $\Omega$  impedance and maximum sample rate of 2 GSa/sec. The oscilloscope has 4 channel input.

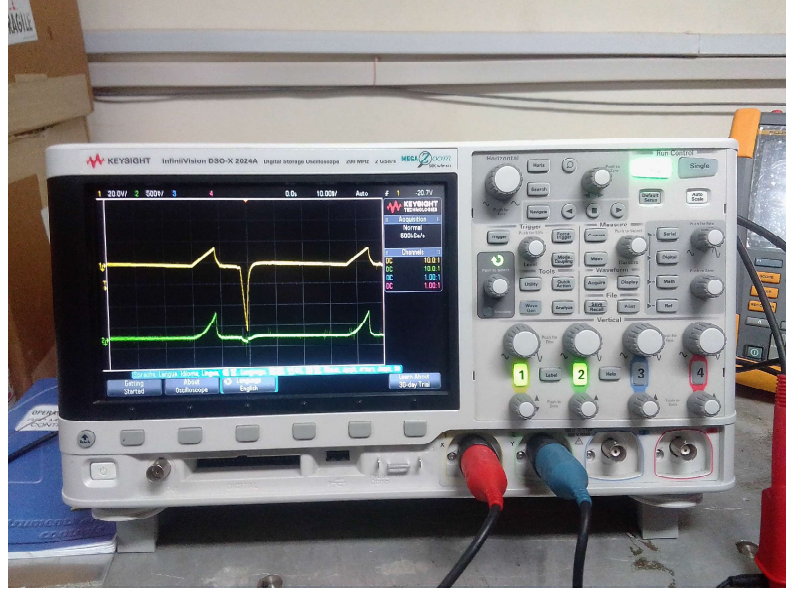


Figure 2.19: Keysight make InfiniiVision DSO-X 2024A model oscilloscope used for signal acquisition.

### Wave number measurement

Wave number of a wave propagating in the plasma can be measured with measuring simultaneous fluctuation signals from two electrostatic probes [97]. The measured time delay between the signals with know distance between the probes gives phase velocity of the wave. The frequency of the wave and the phase velocity together gives the wave number of the wave by the relation  $v_{phase} = \omega/k$ .

For time-delay measurement between two signals, Cross-correlations are useful. Cross-correlation is a measure of similarity of two time series data as a function of the displacement of one relative to the other. For continuous functions  $f$  and  $g$ ,

the cross correlation is defined as,

$$(f * g)(\tau) = \int_{-\infty}^{+\infty} f^*(t)g(t + \tau)dt \quad (2.35)$$

where  $f^*$  is the complex conjugate of  $f$ , and  $\tau$  is the displacement in time series, also known as ‘lag’.

After calculating cross-correlation between two signals, the maximum of the cross-correlation function indicates the point in time where the signals are best aligned, i.e., the time delay between the two signals is determined by the argument of maximum, or  $\arg \max$  of the cross-correlation, as in

$$\tau_{delay} = \arg \max((f * g)(t)) \quad (2.36)$$

Figure 2.20 shows two sine waves with frequency 5 Hz, amplitude 1 and time delay 0.05 seconds and cross-correlation between the two signals.

## Summary

Detailed description of the experimental set-up and diagnostics are presented in this chapter. The fluctuation analysis techniques and the standards of the instruments needed for analysis are explained. Characterization of plasma has been presented. Electron temperature, plasma density, plasma potential and electron energy distribution function in Argon plasma are measured by Langmuir probe technique and Effective electron temperature also been estimated using non-invasive Line intensity ratio method. Langmuir probe I-V data has been fitted with ana-

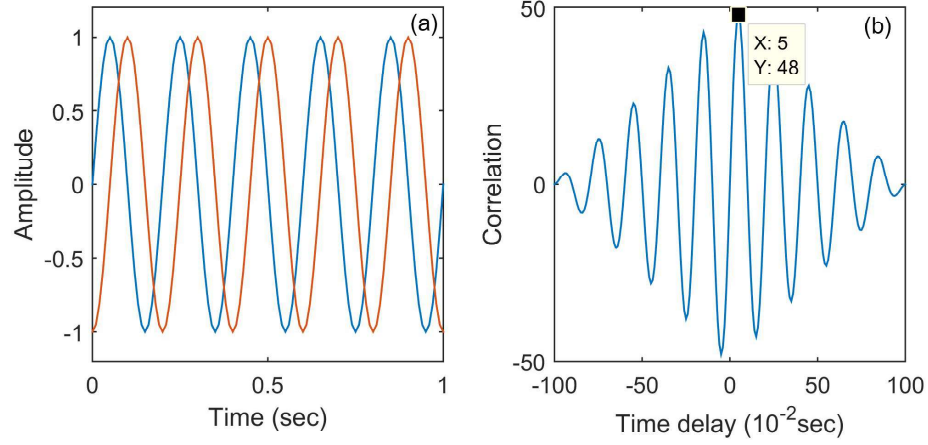


Figure 2.20: (a) Amplitude vs time of the two signals  $f$  and  $g$ . (b) Time delay between the signals  $f$  and  $g$  obtained by Cross-correlation

lytical formula and first, second derivatives are obtained from the fitted curve. A MATLAB software program has been developed for this least square fitting and to obtain plasma parameters. Plasma parameters are measured in different conditions of neutral pressure, discharge current and discharge voltages. From the results it is clear that, two populations i.e., hot and cold electrons exist in the discharge in low working pressure conditions. As the neutral pressure increases, the hot electron populations decreases and effective electron temperatures decreases. Ar neutral and Ar ion emission lines are used for Line intensity ratio method for electron temperature estimation. The temperature obtained from Line ratio method is in well agreement with the effective electron temperature obtained from Langmuir probe technique in low pressure regime but the results deviate in high pressure conditions.

# 3

## Identification of Sheath-Presheath boundaries

### Introduction

Identification of sheath and presheath boundaries is the preliminary task for studying any sheath-presheath phenomena, such as the instabilities excited in this region, studies in this thesis work. The method of identifying the sheath-presheath boundaries experimentally is to measure the spatial potential profile from boundary to bulk plasma and then fit with the theoretical potential profiles of sheath and presheath. The measured sheath potential profile is compared with the Child-Langmuir Law and the measured presheath profile compared the parabolic profile



### Chapter 3. Identification of Sheath-Presheath boundaries

---

as suggested by Riemann[52]. The point in the region where the measured profile start deviating from Child-Langmuir law is considered as sheath edge. The presheath region is identified by fitting of the potential profile from the sheath edge to uniform potential region. In this study, along with the sheath-presheath boundaries identification, the advantages of Laser-heated emissive probe and its affects in the high electric field sheath-presheath regime have also been explored in detail. These experiments gives the direct comparison of conventional and Laser heated emissive probes and their affects in the potential gradients.

Emissive probes are widely used for space/plasma potential measurements in variety of plasmas ranging from RF discharges to tokamaks.[98–101] The idea of emissive probe was given by Langmuir and it works on the simple principle of electron emission from a heated probe and when this probe is biased below plasma potential. The probe ceases to emit electrons when biased above the plasma potential. The emissive probes are required to be heated for emitting electrons. The conventional or the widely used emissive probes are generally a miniature filament made up of tungsten and are heated by passing electrical current through them. Laser heated emissive probe is a recent advancement in emissive probes proposed by Roman Schrittwieser *et al.*, which are heated by high power Lasers.[102] Laser-heated emissive probes (LHEP) are successfully used for plasma potential measurements in RF as well as fusion plasmas.[103, 104] However, LHEPs has to be exposed to wide range of plasma densities and in presence of high electric and magnetic gradients in order to establish its effective usage.

LHEP delivers several advantages over the conventional emissive probes (CEP). For example, since there is no heating current required to be passed though the

probe material, there is no effect of potential drop across the probe material on the plasma potential measurement and the whole laser-heated probe surface remains at same potential. Whereas, in CEP, since a potential drop is required across the probe material to pass the heating current, this potential drop is added to the measuring spatial potential in case of continuously glowing probe. Hence, proper care has to be taken in order to measure absolute plasma potential in CEPs.[105, 106] Furthermore, in CEPs, the mechanical contacts at the probe end terminals lead to reduced temperatures at the ends which results in non-uniform emission over the entire length of the probe. The sheath produced around supporting holders also hampers the emissions from the probe end terminals through the development of relative negative potentials near the end terminals. These issues with CEPs become more significant in measurement of plasma or space potential profiles in presence of strong potential gradients such as in the sheath region as well as in the presence of magnetic fields. In presence of magnetic field, the  $J_{filament} \times B$  forces on the filament emissive probes (CEPs) restricts the orientation of CEPs inside the plasma and also effects its lifetime. The last but not the least, the filament burn outs severely hinders the CEPs lifetime and replacing them in evacuated plasma devices frequently leads to loss of valuable experimental time. By heating a small probe head made up of  $LaB_6$ , tungsten or graphite using a suitable Laser beam, all the above mentioned issues with CEPs can be effectively eliminated. Hence plasma potential measurements with LHEPs need to be consolidated by carrying out experiments with LHEPs in different plasma devices.

## Estimation of Space potential using Emissive Probes

### Space Potential Measurement

Emissive probes are being used for last eight decades to measure plasma potential and well-established methods exist for interpreting the probe data.[107] Construction and heating methods of conventional current-heated probes are reviewed extensively by many authors [24, 108, 109] to showcase their various strengths and limitations. Emissive probes measures the space potential more accurately than their collecting counterpart [110]. Even though, Langmuir introduced the concept of emissive probe in 1920s, its significant usage in the plasma potential measurement came after the reports by Kemp and Sellen in 1967 [108]. They found that the floating potential of the emissive probe tends to saturate as probe temperature increased, and interpret saturating potential as plasma potential. However, if the probe is heated to large enough temperatures, as observed in several experimental investigations[109], the emitted current will not saturate at plasma potential, but will continue to increase due to space charge effects. And for that very reason, careful interpretation is required while using at the emissive probes in plasmas with very high or very low densities. In general this method is valid in the density range  $10^{11}$  to  $10^{18}m^{-3}$ [107]. Smith et al developed a method in an attempt to reduce space charge effects which do not depend on strong emission and hence can be adapted in plasmas with higher densities[111]. The emissive probe emits electrons in the plasma when biased more negatively than the space potential and ceases to emit electrons, except for a small number due to the tail of emitted elec-

tron distribution, when the bias becomes more than the space potential. In the current-voltage (I-V) characteristics, the emissive probes have a wire-temperature ( $T_w$ ) dependent exponential region, whereas the exponential region in case of collecting probes directly depends on the electron temperature ( $T_e$ ). Since the probe wire temperature remains much less than plasma electron temperature ( $T_w \ll T_e$ ) in most of the low temperature laboratory plasmas, where  $T_e \geq 1$  eV, emissive probes can measure the plasma potential more accurately. When inserted inside the plasma and biased externally, the I-V curve of emissive probe contains two components of current: the collected current and the emitted current. The calculations remain simpler till the space charge effect are neglected and the simple basic equations of collecting current and emitting currents describe the qualitative working principle of emissive probes.

The collected current by the emissive probe is similar to the collecting Langmuir probes and given as [23]:

$$I_c(V_b) = \begin{cases} I_{es} \exp [-e (V_P - V_B) / kT_e] & \text{if } V_B \leq V_P \\ I_{es} g'(V_B - V_p) & \text{if } V_B > V_P \end{cases} \quad (3.1)$$

Where  $I_{es}$  is the electron saturation current,  $V_B$  is the probe bias,  $V_p$  is the plasma potential,  $T_e$  is the electron temperature and  $g$  is a function accounting for the angular momentum of the collected current,  $g'$  is its first derivative.

The additional emitted current present in emissive probes is given by

$$I_e(V_B) = \begin{cases} I_{eo} & \text{if } V_B < V_P \\ I_{es} \exp \left( \frac{-e(V_B - V_p)}{T_w} \right) g(V_B - V_p) & \text{if } V_B \geq V_P \end{cases} \quad (3.2)$$

### Chapter 3. Identification of Sheath-Presheath boundaries

---

Where  $T_w$  is the wire temperature and  $I_{eo}$  is the temperature limited emission given by Richardson-Dushman equation:

$$I_{eo} = AT_w^2 S \exp\left(\frac{e\Phi_w}{T_w}\right) \quad (3.3)$$

Where A is Richardson's constant,  $T_w$  is the probe wire temperature, S is the surface area of the probe wire,  $\Phi_w$  is the work function of the material of the probe. Probe emits the emission current when bias voltage less than plasma potential but not above.

After obtaining the I-V characteristics of Emissive probes experimentally, different methods are being implemented for estimating the plasma potential using I-V characteristics. The well-known methods are (1) Separation point method,[112] (2) Floating point method [108] and (3) Inflection point method in the limit of zero emission.[111] Out of these three, the floating point method given by Kemp et al. [108], is relatively simple and convenient technique to estimate the space potential. Although the most accurate, the Inflection point method is lengthy and time consuming method. While, separation point method mostly is an inadequate method. Detailed information regarding comparison and choice of the technique that may be suitable to a particular plasma discharge system is thoroughly reviewed by Sheehan and Hershkowitz [107].

Separation point method compares the I-V characteristics of non-emitting and emitting modes of the same probe from below the plasma potential. The plasma potential is the lowest potential at which the collected current is same for the emitting and non-emitting modes. The point of separation in the superimposition of I-V characteristics from emitting and non-emitting modes reflects the plasma

potential. The accuracy of this method is  $T_w/e$ , though the uncertainty is much larger than  $T_w/e$ . For a sufficient electron emission current from the probe material surface, the sheath potential around the probe surface will decrease and the floating potential approaches the plasma potential. So, when the probe is heated from no emission regime to high emission regime, the floating potential rises rapidly and became saturated at higher emission levels. This saturated floating potential is the Plasma potential. Floating potential method determines the plasma potential with accuracy of the order of  $T_e/e$  and is suitable for measurements in lower electron temperature plasma and does not depend on plasma density. From the ease of measurement point of view, this method is the most appropriate as it can directly measure the plasma potential by measuring the saturated floating potential for higher emission, rather than reading multiple floating potentials at different emission currents.

Inflection point method is developed by Smith et al., to account for space charges effects associated with floating point method. Inflection point technique depends on the fact that inflection point of I-V traces of emissive probe approaches Plasma potential in the limit of zero emission. As emission increases, the inflection point is shifted slightly towards the negative potential because of space charge effects and this shift varies almost linearly. Hence to obtain the space potential, numbers of I-V characteristics are recorded while heating the probe slowly to moderate emission levels i.e. emission current is of the order of Electron saturation current. These inflection points are then extrapolated to zero emission where space charge effects are absent, which gives the plasma potential.

#### Laser-heated emissive probe

Laser heated emissive probes are different from their conventional counterpart in terms of method of heating. The tip of LHEP is heated by high power Lasers instead of electrical current which is used to heat the conventional emissive probes. Heating the probe tips with lasers provides several advantages over conventional heating using currents as it neither requires potential drop across the tip to carry heating current nor any pulsed circuit to avoid issues with uneven potential drops across the probe. So LHEP gives accurate space potential with simple circuitry. LHEP avoids the above problems simply by its nature. Since there is no heating current required to pass through the material, its entire surface always stays at same potential and hence the potential drop issues across the probe material with CEP are effectively eliminated. Again as no heating current passes through the LHEP probe tips, they are not subjected to any  $\mathbf{J} \times \mathbf{B}$  forces when used in presence of magnetic fields. Hence no deformation of LHEP probe tip occurs in strong electric and magnetic fields. The CEP suffers from frequent breaking of its current carrying element which limits its usage in high vacuum systems where changing of filaments of CEPs is always irksome. Furthermore, proper design of holding structures of LHEP reduces the effect of support material on emission as well. Note here that LHEP differs from the conventional emissive probes only in terms of heating methodology and the plasma potential estimation mechanism remains same for the both. All the techniques described in the earlier section for estimation of plasma potential remain same for LHEP and can be implemented on the LHEP I-V characteristics. LHEPs have been successfully used in many plasma devices to measure the plasma potential[102, 103].

## Probes design

As mentioned earlier two different types of emissive probes are used to investigate the spatial potential profile namely conventional emissive probe and Laser heated emissive probe. Conventional emissive probe of loop length 3 mm is made with tungsten wire of diameter 0.125 mm and length 7 mm. The tungsten wire is electrically connected to bunch of fine copper twisted wires in two single-bored ceramic tubes.[105] The electrical connections are brought outside the vacuum using two vacuum BNC connectors. The schematic diagram of the probes construction is shown in Figure 3.1. Laser heated emissive probe tip is made up of Lanthanum hexaboride ( $\text{LaB}_6$ ), which has low work function  $\sim 2.5$  eV. The LHEP probe tip is of a tablet shape with diameter  $\sim 2$  mm and thickness  $\sim 1.5$  mm and is being held by one single-bored ceramic tube. The electrical connection is brought out through this ceramic tube.  $\text{CO}_2$  laser of wavelength  $10.6 \mu\text{m}$  has been used to heat the probe tip. The 2 mm diameter laser beam is focused on to the probe tip using a Zinc selenide ( $\text{ZnSe}$ ) lens. The details of LHEP used along with the measurements of emission current and temperature profile of  $\text{LaB}_6$  material are presented elsewhere.[104] Spatial resolution of LHEP and CEP are  $\sim 2$  mm and  $\sim 3$  mm respectively, however, the shaft of CEP is bigger than that of LHEP as it has to accommodate two ends of curved tungsten wire. Usage of single ceramic tube to hold LHEP tip makes the probe shaft of LHEP smaller than the CEP shaft and hence disturb the plasma less compared to CEP.

The schematic of the electrical circuitry for both the probes is shown in Figure 3.2. The two terminals of the filament probe are connected to the heating power



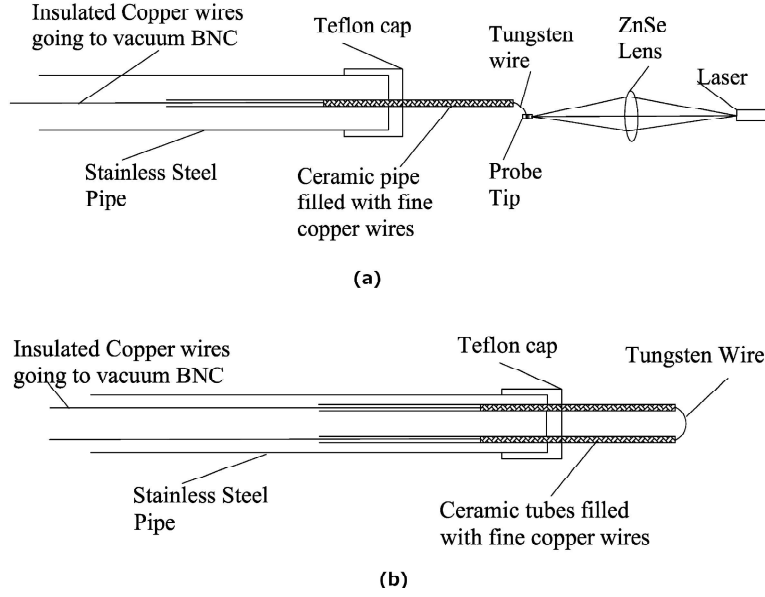


Figure 3.1: Schematic diagram of probes (a) Laser-heated Emissive probe (b) Current-heated emissive probe

supply through vacuum BNC and biasing power supply is connected to either positive or negative leg of the heating supply. The current flowing through the biasing circuit is measured by potential drop across the  $500\ \Omega$  resistor. Floating potential method is adopted for sheath potential profile measurement using both the probes. In order to measure the floating potential accurately, the input impedance of the measuring device must be sufficiently high so the current drawn is as small as possible [108]. In the reported measurements, the floating potential is measured across a  $1\ \text{M}\Omega$  resistor for both the CEP and LHEP.

Different techniques are compared to estimate the plasma potential for both conventional and laser heated emissive probes.

The sheath identification experiments using CEP and LHEP are carried out in system described in chapter 2. The experimental arrangement is shown in

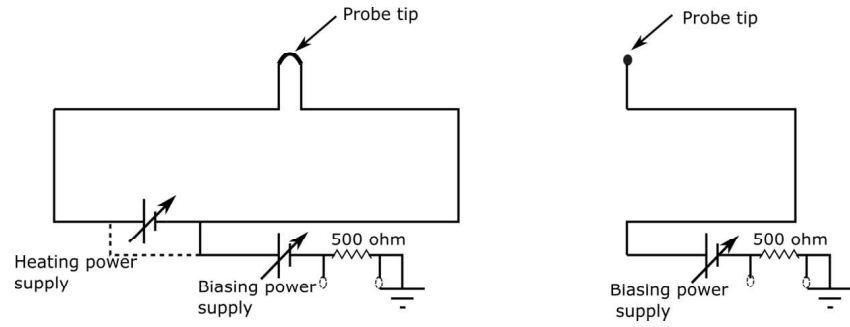


Figure 3.2: Schematic diagram of the probe circuits

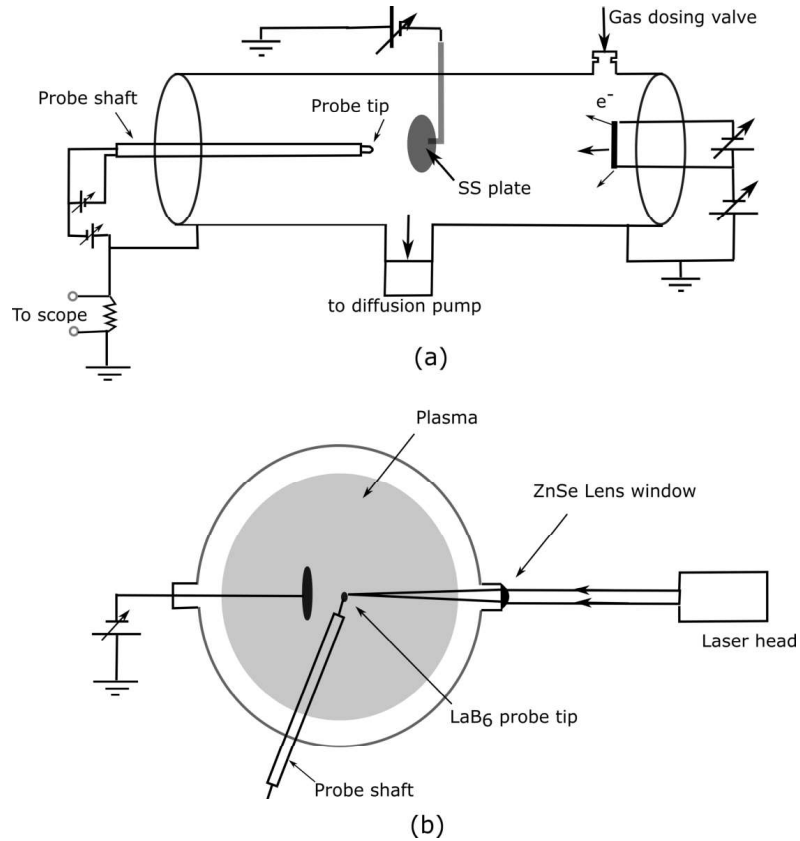


Figure 3.3: (a) Schematic diagram of the chamber (b) Schematic of Laser-heated probe arrangement.

Figure 3.3. Single Langmuir probe made up of tungsten wire of 0.5 mm diameter and 4 mm length is used to estimate the plasma parameters. For this study, the typical plasma density and electron temperature are  $\sim 1 \times 10^{14} m^{-3}$  and 2 - 4 eV respectively for the plasma produced with Helium at  $1 \times 10^{-3}$  to  $5 \times 10^{-3}$  mbar working pressure, discharge current of 250 mA to 600 mA and discharge voltage of - 60 V. Sheath to be studied is produced in the vicinity of a stainless steel (SS) plate of diameter 5 cm immersed in the plasma has been studied with emissive probes. This SS plate placed at the centre of the chamber is covered with Teflon cap on the backside and biased with negative potential of -30 V with respect to chamber to produce sheath.

## Experimental Results and Discussions

The experiments are carried out in two parts. The first set of experiment is to measure the plasma potential in the bulk region using both CEP and LHEPs. These experiments are carried out with working pressure  $\sim 5 \times 10^{-3}$  mbar, discharge current  $\sim 300$  mA and discharge voltage of - 60V. Electron density and temperature in these conditions are  $\sim 5 \times 10^{14} m^{-3}$  and  $\sim 2.5$  eV respectively. The second set of experiment is carried out for measurement of sheath potential measurement, which is carried out in different parameter regime of plasma, i.e., working pressure  $\sim 1 \times 10^{-3}$  mbar, discharge current  $\sim 600$  mA and discharge voltage of - 60V. Electron density and temperature in these conditions are  $\sim 4 \times 10^{14} m^{-3}$  and 3 eV respectively.

## **Estimation of Space potential using CEP**

In the experiments, the conventional emissive probe is operated as continuous emissive probe with DC current heating. After obtaining stable plasma in the system the CEP is biased from -30 V to +30 V for obtaining the I-V characteristics in both cold and emitting conditions for different heating currents. Analyzing the I-V characteristics, the plasma potential has been estimated using floating point method and inflection point method as described in section 2. The space potential values estimated from the separation point method are found to be erroneous as the I-V characteristics of cold and emitting probe does not match above crossing point and crossing point is also found to be sensitive to emitting current. Floating point method produced much better and consistent results. I-V characteristics of CEPs are plotted for different emission levels in Figure 3.4. From Figure 3.4, as the emission level increases, the floating potential shifts to more positive values initially and saturates at  $\sim 2.5$  V at higher emission levels more than  $4 \times 10^{-4}$  A, giving the plasma potential. Plasma potential also estimated with the Inflection point method, which is in good agreement with the floating point method. Because of the simplicity, we adopt floating point method throughout in this experiment.

We note here that as CEP carries the heating current, there exists a potential drop across the probe tip, which is exposed to the plasma. Therefore the measured potential includes this potential drop in addition to the plasma potential. Further the measured potential also depends on which leg of the probe has been connected to the measuring circuit. It has been observed that the measured floating potential differs by up to a maximum of  $\sim 3$  V in these experiments for positive and negative probe leg connections of the heating circuit to the biasing-cum-measuring

circuit as shown in Figure 3.5. This floating potential difference is proportional to applied heating voltage. This feature is quite common and has been studied in detail by Mravlag and Krumm [105]. As suggested in that reference [105], the floating potential is taken as average of these two values in this experiment. There is another method using two equal resistors in parallel with the CEP heating loop. From the point between the two resistors the exact value of the plasma potential can be determined [30]. Hence, this choice of connection also results in substantial errors in plasma potential measurements with floating point technique with CEP. The pulsed (AC) emissive probe can avoid this problem by measuring I-V characteristics in the non-heating cycle and will give accurate plasma potential, but it requires a sophisticated electronic setup which is very sensitive to stray signals. In absence of the sophisticated electronic circuitry, the CEP measurements are carried out as simple continuous emissive probe.

## Estimation of Space potential using LHEP

The complete exercise is repeated with the I-V characteristics obtained with LHEP. The probe is heated to different temperatures by varying the  $CO_2$  Laser power. Figure 3.6 shows the I-V characteristics obtained with LHEP at different heating powers, i.e., at different emission levels. As the emission current is increased the floating potential decreased and saturated at  $\sim 3$  V at above the heating power of  $\sim 20$  W giving space potential  $\sim 3$  V in the plasmas produced with exactly same operational parameters where the CEP are used.

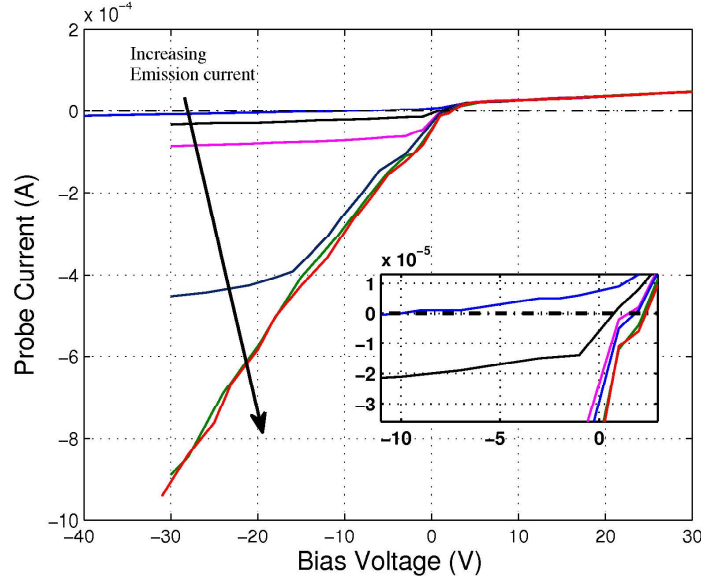


Figure 3.4: Characteristics of CEP for different emission currents. Electron density and temperature are  $\sim 5 \times 10^{14} m^{-3}$  and  $\sim 2.5$  eV, respectively.

### Sheath Potential Profile Measurement using CEP and LHEP

As described in the introduction the study of plasma sheath is very important, since sheath plays an important role in most phenomena like confinement of charged particles, heat load to the physical boundary. The sheath thickness and its potential structure is measured by many authors [4-7] using the emissive probes to understand the nature and dynamics of sheaths. In this thesis, an attempt has been made to measure the sheath potential structure formed in front of a stainless steel plate immersed in the plasma using a Laser heated emissive probe for the first time. To compare the results obtained using the LHEP, a conventional emissive probe (CEP) is also kept alongside the LHEP. In this set of experiment, the Helium plasma is produced at working pressure of  $1 \times 10^{-3}$  mbar, discharge voltage -60V

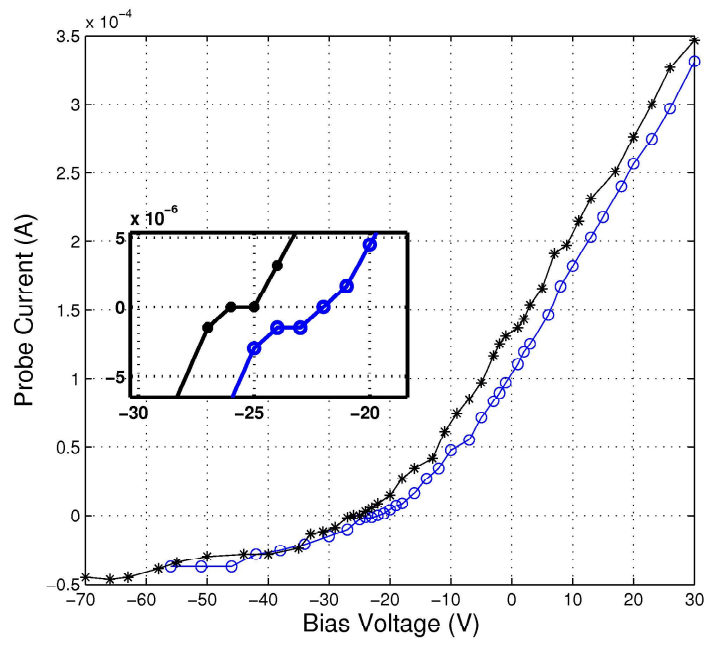


Figure 3.5: CEP I-V traces for bias circuit connected to different legs of the probe; (-o-) for connection to positive leg and (-\*-) for negative leg.

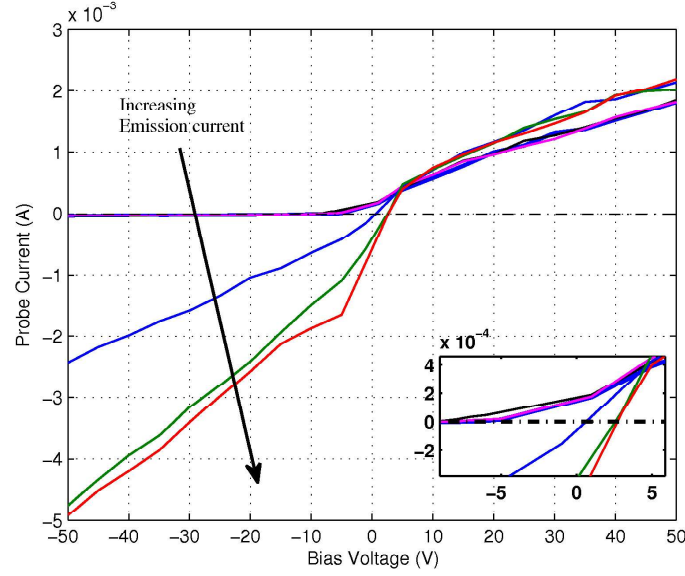


Figure 3.6: LHEP I-V traces for various emission levels in bulk plasma. Electron density and temperature are  $\sim 5 \times 10^{14} m^{-3}$  and  $\sim 2.5$  eV, respectively.

and discharge current 600 mA. Plasma potential is estimated by floating potential method using both the CEP and LHEP. The space potential measured with CEP and LHEP from sheath region to bulk region through presheath region and is plotted in Figure 3.7. Within the experimental uncertainties in the positions of both the probes, the LHEP always measured higher values of space potential at similar locations across the sheath and bulk plasma than that measured with CEP. The difference in measured space potential values by both the probes remain less ( $\sim 0.5 - 0.7$  V) in the bulk plasma whereas differences up to  $\sim 5$  V are observed in the region joining the sheath and bulk plasma, generally known as presheath. Further detailed studies are required to establish the cause of this large difference in the measured values of space potential in the presheath region by both the probes.

The presheath potential profile measured with LHEP is fitted with the formula



### Chapter 3. Identification of Sheath-Presheath boundaries

---

[31]  $\phi = \phi_0 + T_e \sqrt{\frac{x-x_0}{\lambda}}$  as shown in Figure 3.8, where  $\lambda$  is the ion-neutral collision mean free path,  $\phi_0$  is the potential at the sheath edge  $x_0$ . In case of LHEP, the potential drop  $\sim 4V$  in the presheath region is of the order of  $(T_e/e)$ . The sheath-presheath boundary is determined by extent of the potential profile well-fitted with the Child's law. Hence, the plasma potential profile near the plate measured with LHEP is fitted with Child's law [31] (shown in Figure 3.8) to determine the sheath-presheath boundary. The experimentally measured potential profile with CEP fits well with Child's law up to 3 mm away from the plate, whereas the data obtained with LHEP fits the Child's Law well up to 4 mm away from the plate. Hence both the probes measured almost same sheath thickness. The sheath thickness calculated using the Equation 1.35, where,  $\lambda_{Ds}$  is the Debye length at sheath edge,  $V_0$  is the potential on the plate and  $T_e$  is the electron temperature. Sheath thickness comes out to be  $\sim 6$  mm, which is closer to the value obtained with LHEP in comparison to CEP.

The measurements of plasma potential in the sheath, presheath and in the bulk plasma region of filament produced plasma using LHEP matches quite well with available theoretical models and also are comparable to those obtained with CEP. Therefore, the reported measurements with LHEP further establish its capabilities of plasma potential measurements in various regions of plasmas having different electric field gradients.

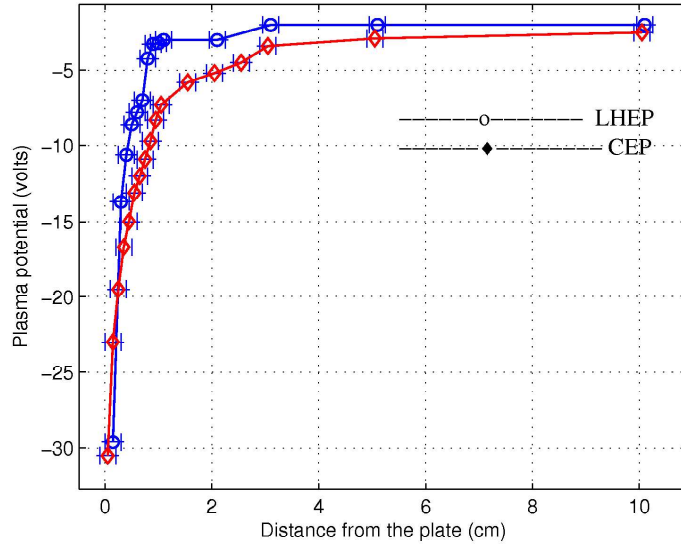


Figure 3.7: Potential profile measured with LHEP and CEP for various distance from the plate surface. The error bar in distance (x-axis) is  $\pm 1.5$  mm. Electron density and temperature are  $\sim 4 \times 10^{14} m^{-3}$  and  $\sim 3$  eV, respectively.

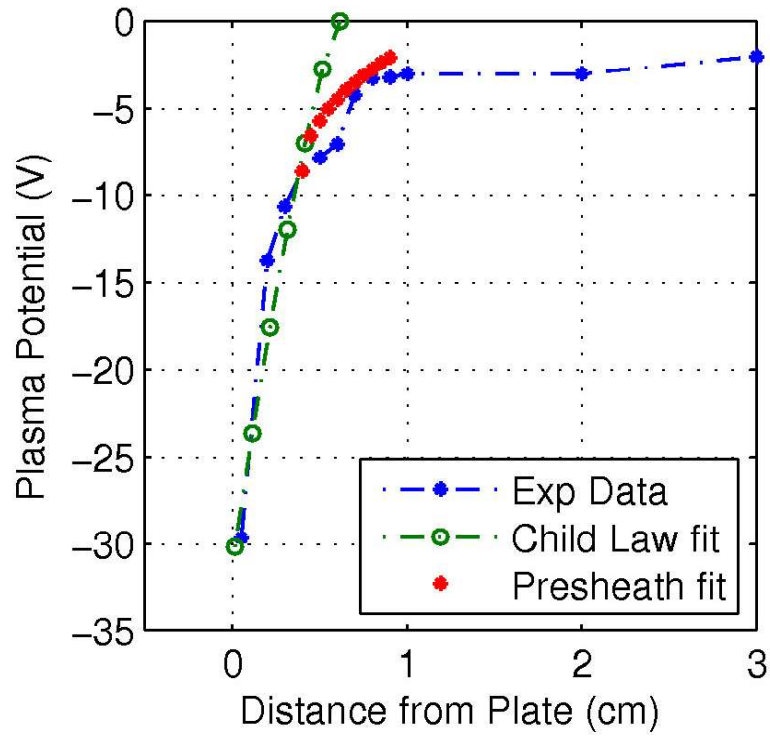


Figure 3.8: Child law and Presheath potential fit to the LHEP experimental data. The measurement errors are within  $\pm 5\%$ .

## Conclusion

Sheath-presheath boundaries are identified by measuring spatial potential profile from the material boundary to the bulk plasma using emissive probes. In this study current-heated emissive probe and Laser-heated emissive probes are employed for plasma potential measurement. Sheath and presheath boundaries are identified by fitting the measured spatial potential profile with the theoretical profiles. The LHEP is calibrated by measuring plasma potential in the bulk plasma using CEP. Both the probes measure similar plasma potential in the bulk plasma. The CEP measures the sheath thickness of  $\sim 3$  mm whereas the LHEP measures the sheath thickness of  $\sim 4$  mm close to the theoretically estimated value of  $\sim 6$  mm. The measured values of plasma potential using both the probes differ significantly in the presheath region. The vulnerability of current heated probe measurements in the presence of electric fields may be one of the reasons behind this discrepancy. Therefore, it indicates that with several advantages over CEP, the LHEP can be used effectively in measurements of plasma potentials in plasmas. This study also lightens up the need of study of plasma potential measurement in the different magnetic field configurations using current-heated and Laser-heated emissive probes simultaneously.

# 4

## Ion-ion counter streaming instability in the presheath of single-ion species and two-ion species plasmas

### Introduction

In general, the sheath equilibrium is unstable to three types of modes: (1) ion-ion instabilities and (2) electron-ion instabilities and (3) electron-electron instability. Ion-ion instability get excited because of the differential velocities between ion species. There are two different cases possible, one is, two different ion species moving in the same direction with different velocities, and another case of same

## Chapter 4. Ion-ion counter-streaming instability

---

or different ion species moving in the opposite direction (counter-streaming). The earlier case is possible in multi-ion species plasma, where different ion species streaming along with each other with different velocities in a potential drop and later is possible in sheaths produced by transparent grids in the plasma and ionospheric plasmas.

Ion-ion streaming instabilities have been extensively studied in space plasmas, where streaming of different ion species in different directions excites these instabilities. Counter streaming of ions are often observed in space plasmas and hence there lies strong possibility of observing ion-ion counter streaming instabilities. This instabilities has been extensively studied in auroral region.[15, 113, 114]

Apart from existence in terrestrial plasma, ion-ion counter streaming instability can also be excited in the filling of wake of body in flowing plasmas, near the grids in double plasmas and near the virtual cathodes. The flow of ions in all the above four examples are pictorially depicted in Figure 4.1. Ion-ion counter-streaming instability in single species plasma, near the grid in a double plasma device has been reported by Nakamura[7] and also in this thesis. This instability is excited by the counter streaming ions from both sides of the mesh grid. The ions flow from both sides of the grid, excite the instability, of which the zero-frequency mode is unstable if the density and velocity of both the beams are equal. This instability has much importance in case of ion-beam etching of materials and thin film deposition, where transparent negatively biased grids are commonly used to extract ion beams. Ion beam parameters and beam angle of incidence affects the etching rate and the presence of ion-ion counter streaming instability may modify the intensity and focusability of the ion beam.

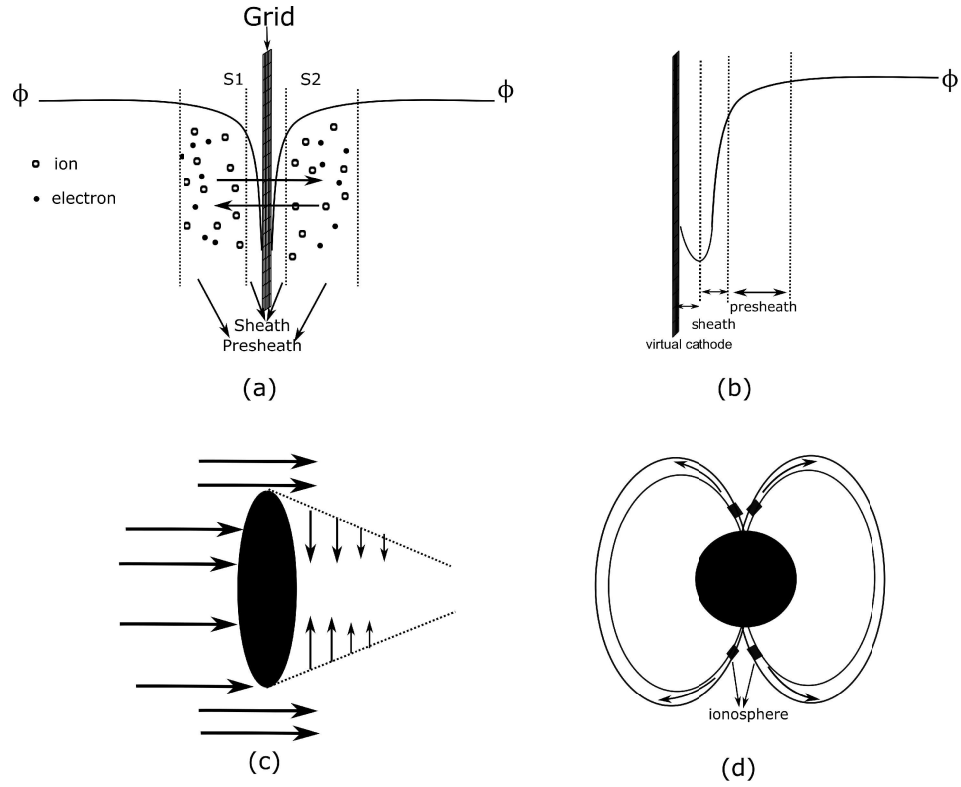


Figure 4.1: (a) Grids placed in the plasma (b) near virtual cathode formation (c) wake formation behind the object in flowing plasma (d) Terrestrial region of ionospheric plasma. ion flows are shown with arrows.

## Chapter 4. Ion-ion counter-streaming instability

---

In this chapter, the experimental observations and detailed studies of ion-ion counter streaming instability in the presheath-sheath region on either side of a floating mesh grid immersed in a filament-produced low temperature, low pressure Ar, He and Ar + He plasmas have been reported. To the best of our knowledge, the observations of ion-ion counter streaming instability in plasmas produced with different gases as well as with gas mixtures are reported for the first time. In the Ar plasma, the frequency spectra of the floating potential fluctuations from the grid and from a movable Langmuir probe traversing the sheath-presheath region show a dominant broad peak in the range of 10-20 kHz centering around 15 kHz. This peak in the frequency spectra is found to exist only in sheath-presheath region and disappears in the bulk plasma. This instability has been identified as the ion-ion counter streaming instability as it ceases to exist when the mesh grid is covered with a thin metal foil from one side, which restricts the counter streaming of the ions. Further, the wavenumber,  $k$  of the wave is measured experimentally, which matches quite well with the calculated one from the dispersion relation of ion-ion counter streaming instability. Unlike the observations of Nakamura,[\[7\]](#) the instability has been observed even when the mesh is kept floating inside the plasma, i.e., no biasing of the grid is required to excite the instability and the effect of biasing the mesh in both polarities has also being studied in detail. After establishing the observed floating potential fluctuations of  $\sim 10$ -20 kHz in the sheath-presheath region of mesh-grid to be due to the ion-ion counter streaming in Argon plasmas, the experiments are repeated in He and Ar + He (two-ion species) plasmas. The ion-ion counter streaming instability is observed in the He and Ar + He mixture plasmas. In the Ar + He plasma, the measured frequency band of



the fluctuations is shifted towards higher frequency, which is in agreement with the derived dispersion relation for He + Ar plasma. Further it has been observed that when the neutral pressure increases beyond a threshold level, ion collisions with neutrals suppresses the instability.

The remaining chapter is organized as follows: Experimental set-up and measurement techniques are explained in section II. Experimental results are discussed in section III. The dispersion relation for ion-ion counter streaming instability in single-ion species plasma has been derived in section IV followed by Discussion and summary in sections V and VI respectively.

## Experimental Set-up

The experimental set-up for this particular study is shown in Figure 4.2. The mesh grid made up of stainless steel is placed at center of the chamber to form sheath-presheath regime around it. Before plasma initiation, the experimental chamber is evacuated down to a base pressure of  $6 \times 10^{-6}$  mbar. For producing Ar plasma, the chamber is filled with Argon gas using a mass flow controller (MF1) in the pressure ( $P_{fill}$ ) range of  $\sim 6 \times 10^{-4}$  -  $5 \times 10^{-3}$  mbar, the filaments are heated by passing  $\sim 6$  -  $6.5$  A of current through each of them and biased negatively with respect to the chamber to initiate the discharge. The plasma is generated through electron impact ionization process by the thermally ejected electrons from hot Tungsten filaments, which are accelerated in the electric field present due to negative biasing of filaments with respect to the chamber. Application of discharge voltages in the range of - 40 to - 80 V drives discharge current in the range of 0.35 - 1.20 A. Typical plasma parameters are: plasma density,  $n_e \sim 2 \times 10^7$  -  $1 \times 10^9$ /cc

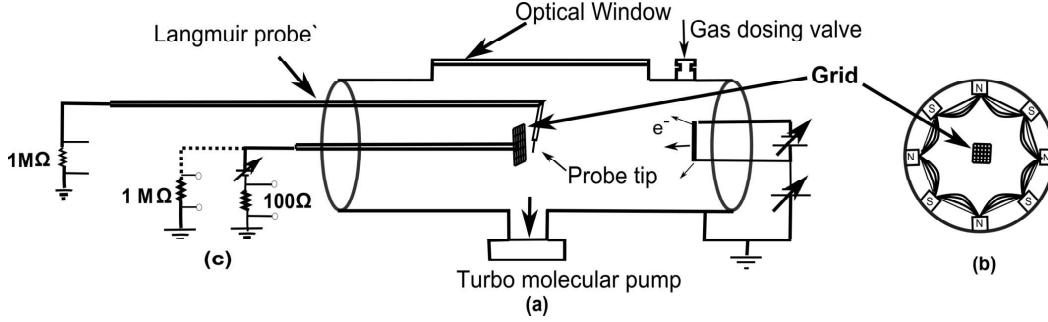


Figure 4.2: (a) Schematic diagram of the experimental set-up. (b) Cross-sectional view showing surface cusp magnetic field (c) Circuit diagram for Grid and Langmuir probe.

and electron temperature,  $T_e \sim 3 - 5$  eV. Conventional and Laser heated emissive probes are used to measure the sheath-presheath potential profile and to identify sheath, presheath boundaries.[115]

Similarly the He plasma is produced using another mass flow controller (MF2). The Ar + He (two ion-species) mixture plasma is produced in two ways and the observations reported later in the paper are repeated in both the cases. In first case a low pressure Ar plasma is produced at neutral pressure of  $5 \times 10^{-4}$  mbar and then He is introduced in a controlled manner using MF2 to bring the total neutral pressure of  $3 \times 10^{-3}$  mbar in the chamber. In the second case a low pressure He plasma is produced first at neutral pressure of  $4 \times 10^{-4}$  mbar and then Ar is introduced in a controlled fashion using MF1 to bring the total neutral pressure of  $3 \times 10^{-3}$  mbar in the chamber. In both the cases, the optical emission spectra from the plasma are recorded using Ocean optics USB4000-VIS-NIR spectrometer (wavelength range 350 - 1000 nm). The observations of Helium neutral spectral line at 501.5 nm and several Argon neutral lines in the wavelength range 650 - 950 nm ensure the presence of both the species in the plasma.

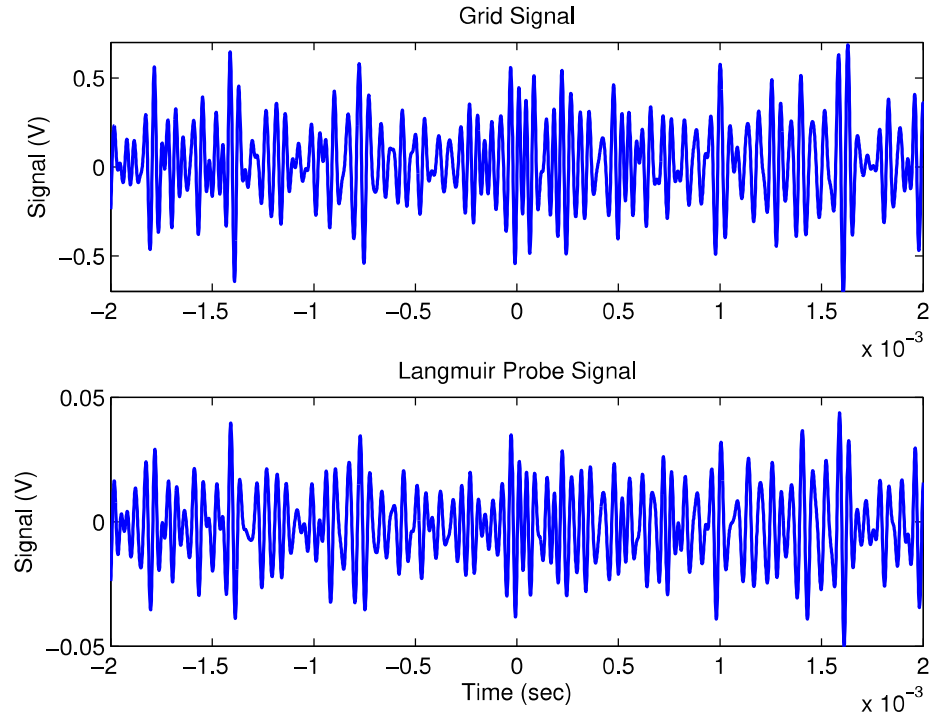


Figure 4.3: Typical filtered fluctuation signals between 10-30 kHz, acquired simultaneously from floating mesh grid and floating langmuir probe

The sheath, investigated in the present study, is produced around a stainless steel planar mesh grid of square shape having length of 5 cm placed at the radial and horizontal mid-plane of the plasma chamber. The mesh grid is oriented with its surface perpendicular to the axis of the cylindrical chamber as shown in Figure 4.2 (part b). The mesh grid has 36 lines per inch and of 75 percent transparency. Depending upon the experimental requirements, the mesh grid is either kept floating or biased with respect to the vessel. In case of floating potential measurements of the grid, it is terminated to a high resistor  $1\text{M}\Omega$  as shown in Figure 4.2 (part c) with dotted lines and the voltage across the resistor is measured with a Keysight make Oscilloscope model, InfiniiVision DSO-X 2024A, 200 MHz band width,  $1\text{M}\Omega$  impedance and maximum sample rate of 2 GSa/sec., whereas in the case of biased grid, the current through the grid is converted to voltage using a resistor  $500\Omega$  and measured in the oscilloscope.

An axially movable cylindrical Langmuir probe made up of tungsten having probe-tip length of 5 mm and diameter 0.7 mm is used to measure the floating potential in the sheath, presheath, bulk plasma and its cylindrical surface is placed parallel to the surface of the mesh grid. For floating potential measurements, the probe is terminated to a high resistor  $1\text{M}\Omega$  and the voltage across the resistor is fed into the oscilloscope. Floating potential fluctuations from both Langmuir probe and grid are recorded. The same probe is also used for density and temperature measurements in the bulk plasma by using I-V traces, obtained using a variable power supply.[116]

## Experimental Results

In the first set of experiments, the time traces of the floating potential fluctuation of the grid and that of Langmuir probe (LP) are recorded in Argon plasma produced with parameters  $P_{fill} = 8 \times 10^{-4}$  mbar, discharge voltage -80 V, Discharge current 1.2 A, total filament current 13 A,  $n_e \sim 5 \times 10^8$  /cc, and  $T_e \sim 4$  eV. The position of the mesh grid is kept fixed whereas the Langmuir probe is moved from the bulk plasma region to the presheath-sheath region of the mesh grid. Figure 4.3 shows the time trace of floating potential fluctuation signal filtered between 10-30 kHz, from the mesh grid and Langmuir probe, placed at 5 mm away from the grid surface. To characterize the observed fluctuations in the floating potential of mesh grid and LP, Fast Fourier Spectral Analysis has been performed on fluctuation data. The data have been recorded with a sampling time of one micro second and the Fast Fourier Transform (FFT) has been performed on the data length of 50,000 points. The frequency spectra of the floating potential fluctuation of grid and LP, smoothed over 700 points with frequency resolution of 1.4 kHz, is shown in Figure 4.4. Two distinct broadband peaks, one at  $\sim 10$ -20 kHz and another at  $\sim 200$  kHz are observed in the frequency spectra of both the grid and LP data, however the higher frequency peak exists only in the low pressure regime  $4 \times 10^{-4} - 1 \times 10^{-3}$  mbar and discharge voltage range 55-90 volts. The intensity of peak at  $\sim 10$  - 20 kHz is much higher than the other peak. Both the peaks in the frequency spectra of floating potential fluctuations of LP cease to exist as the LP is moved out of the sheath-presheath region of the mesh grid in to the bulk plasma. Figure 4.5 shows the frequency spectra of floating potential fluctuations measured in the

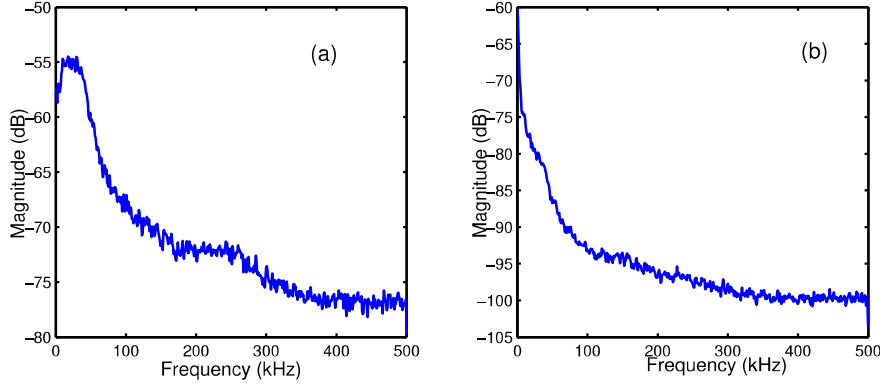


Figure 4.4: Power spectra of (a) Grid and (b) Langmuir probe shows broad band frequency in the frequency range 20 kHz at working pressure  $8 \times 10^{-4}$  mbar, discharge current 1.2 A, discharge voltage 80 V,  $n_e = 8 \times 10^8/cc$ ,  $T_e = 4$  eV.

presheath region (red line) and in bulk plasma far away from the mesh-grid (Blue line) by Langmuir probe. The figure clearly shows that the spectral peaks in the frequency spectra are absent in the bulk plasma demonstrating the existence of instabilities governing the observed spectral peaks in frequency spectra to be well confined in the presheath region only. In this chapter, we report only the detailed characterization of instability associated with the intense peak observed in the frequency spectra of floating potential fluctuation of grid and LP at  $\sim 10 - 20$  kHz.

Further experiments are carried out to find the effect of discharge current, discharge biasing voltage and the neutral pressure on the observed spectral peak at  $\sim 10 - 20$  kHz. As the discharge current is decreased from 1.2 A, the centre of the spectral peak shifted towards lower frequency attaining 12 kHz at 0.3 A. The width of the peak also decreased as the discharge current is decreased from 1.2 A, however the magnitude of the peak remained almost constant. The variation of spectral width and the central frequency with the variation in discharge current

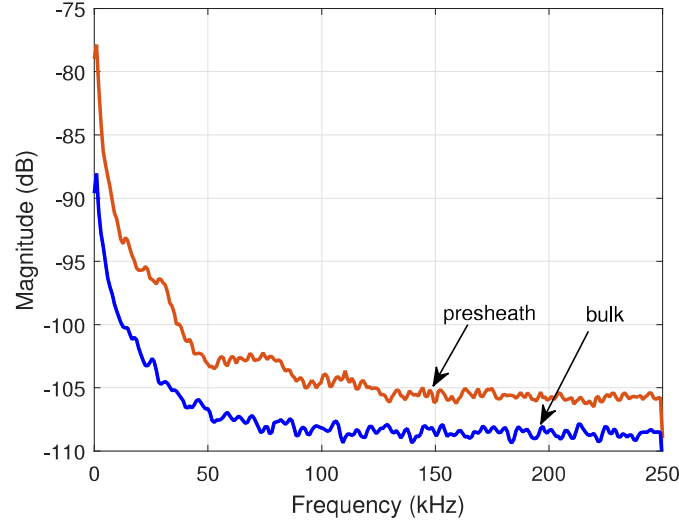


Figure 4.5: Frequency spectra of floating potential fluctuations from Langmuir probe in presheath and bulk plasmas. At working pressure  $9 \times 10^{-4}$  mbar, discharge current 0.75 A, discharge voltage 80 V,  $n_e = 6 \times 10^8/cc$ ,  $T_e = 3$  eV.

is shown in Figure 4.6. Note that the discharge current is varied by changing the heating current of the plasma producing filaments slightly at a constant discharge voltage. Similarly, in next set of experiments, the neutral pressure is varied keeping the discharge current nearly constant again by varying the heating current. It is observed that the characteristics of the spectral peak at  $\sim 10 - 20$  kHz followed the similar trend as observed with discharge current variation. Figure 4.7 shows that as the neutral pressure is decreased from  $1 \times 10^{-3}$  mbar to  $4 \times 10^{-4}$  mbar, the spectral peak width decreases and the peak centre shifts towards the lower frequency. We have also varied discharge voltage, keeping the discharge current nearly constant again by varying the heating current, and observed that the characteristics of the spectral peak at  $\sim 10 - 20$  kHz remained unaltered at discharge voltages in the range of 90 - 50 volts.

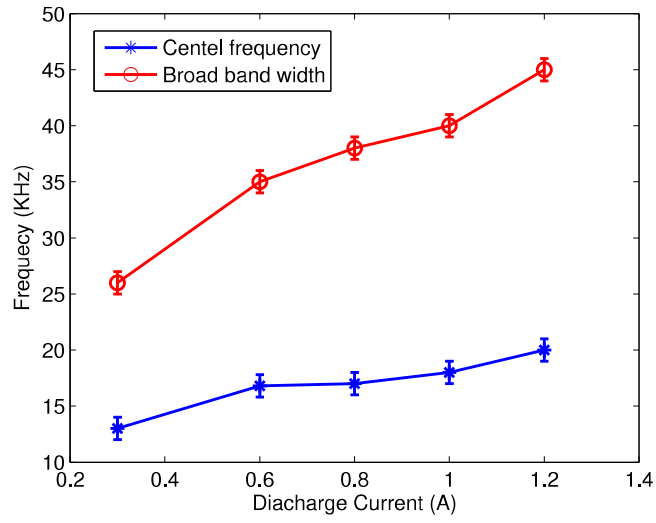


Figure 4.6: Variation of low frequency peak with discharge current. Central frequency (blue line -\*-) and width of the broad band peak (red line -o-) decreases with decreasing discharge current. working pressure  $8 \times 10^{-4}$  mbar, discharge voltage 80 volts



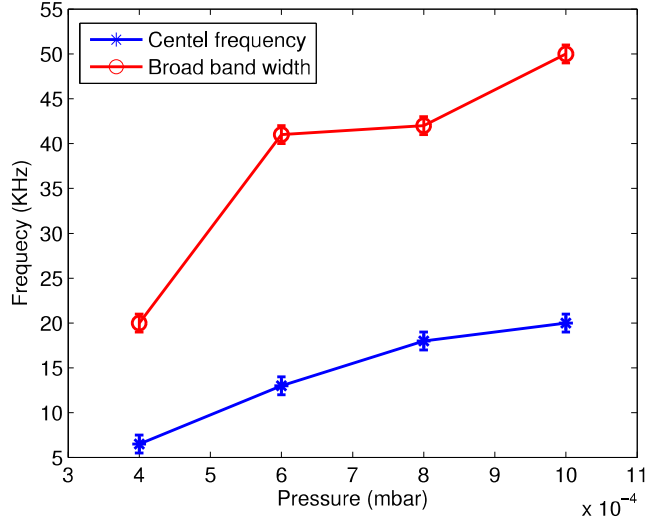


Figure 4.7: Variation of low frequency peak with neutral pressure. Central frequency (blue line -\*-) and width of the broad band peak (red line -o-) decreases with decreasing neutral pressure. Discharge current 1.2 A, discharge voltage 80 volts

The observed spectral peak in the frequency spectra at  $\sim 10 - 20$  kHz is much less than the ion plasma frequency  $0.23 - 1.1$  MHz for different discharge currents. And its dependence on the discharge current and neutral pressure, hence on plasma density, clearly indicates that the frequency of the instability is proportional to ion plasma frequency. Additional evidence of involvement of ions in the observed instability comes from the experiments carried out in higher neutral pressure. When the neutral pressure is increases beyond  $\sim 4 \times 10^{-3}$  mbar, the magnitude of the spectral peak starts decreasing. And the peak completely vanishes after a threshold pressure of  $\sim 6 \times 10^{-3}$  mbar. Beyond the neutral pressure  $\sim 4 \times 10^{-3}$  mbar the sheath-presheath becomes collisional as the ion-neutral mean free path became comparable to the presheath length. The amplitude of the spectral peak and the

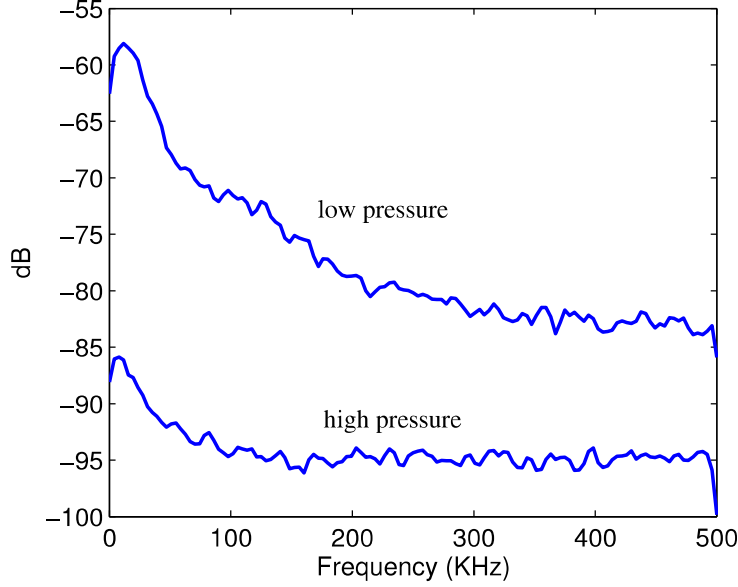


Figure 4.8: Graph showing power spectral density vs. frequency for high and low working pressures. High pressure:  $6 \times 10^{-3}$  mbar; Low pressure:  $8 \times 10^{-4}$  mbar

ion-neutral mean-free path versus the neutral pressure is plotted in Figure 4.8. In low temperature plasma ( $T_e/T_i \gg 1$ ), ion drift velocity in the presheath is much greater than the thermal speeds of ion and neutral. So, constant ion-neutral collision frequency at a velocity associated with the drift can be considered and is given by,  $\nu_{in} = n_g \langle \sigma(V_i) V_i \rangle \sim n_g \sigma(V_i) V_i$ . Ion-neutral mean free path is given by  $\lambda_{in} = 1/n_g \sigma(V_i)$ , where  $n_g$  is the neutral gas density,  $\sigma$  is the ion-neutral collision cross section and  $V_i$  is the ion drift velocity. The Figure 4.9 clearly shows that as the mean free path approaches the presheath dimension ( $\sim 1$  cm), at higher neutral pressures of  $\sim 4 - 6 \times 10^{-3}$  mbar, the spectral peak  $\sim 10 - 20$  kHz cease to exist.

To further verify the nature of the instabilities, we cover the mesh grid with Aluminium foil from one side. Covering the mesh from one side led to a significant

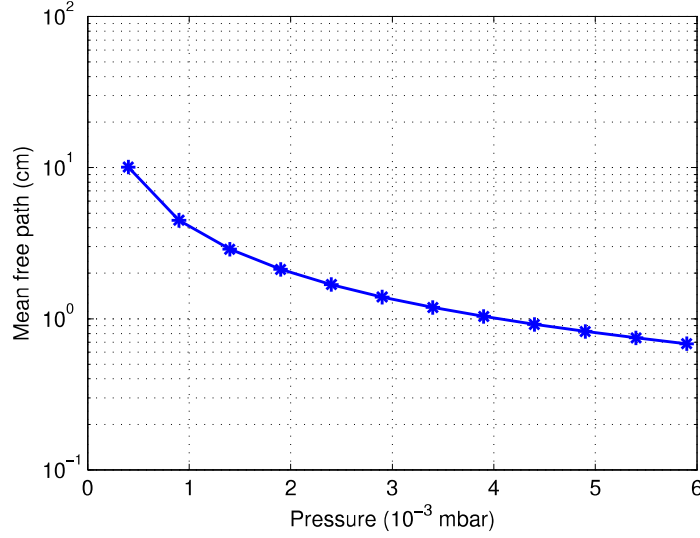


Figure 4.9: Ion-neutral mean free path vs. working pressure. The mean free path approaches the presheath dimension ( $\sim 1$  cm), at high neutral pressures  $4 - 6 \times 10^{-3}$  mbar.

reduction in the amplitude of this low frequency peak at 10 - 20 kHz. To ascertain the role of ion further in causing the observed instability, the grid is biased positively with respect to the plasma potential in the electron saturation regime. The instability remained absent in this case as the frequency peak at 10 - 20 kHz does not appear in the time trace of electron saturation current of the mesh grid and the floating potential of LP. These observations hints at the possibility of the ion-ion counter streaming instability being excited through the mesh grid as covering the mesh grid from one side restricts the ion flow through the grid on either side. And also the instability disappears with biasing the mesh grid positively in the electron saturation region as the positively biased grid repels the ions and restricts them to pass through it.

In the second set of experiments, the observations are repeated in Ar, He as

well as in Ar + He plasmas in similar experimental conditions of total neutral pressure  $3 \times 10^{-3}$  mbar, discharge current 0.7 A, discharge voltage -80 V and plasma parameters ( $n_e \sim 1-5 \times 10^8$  /cc  $T_e \sim 2-4$  eV). The He and He + Ar plasmas are produced by methods described in section 2 and the floating potential fluctuations from the mesh-grid and LP are recorded. The FFT spectra of floating potential fluctuations from all three plasmas (Ar, He and Ar + He) are compared in Figure 9. In the He plasmas, floating potential fluctuations of marginally (20% ) higher amplitude as compared to Ar plasmas have been observed. The frequency spectra of floating potential fluctuations in He plasma show a broadband peak similar to that observed in Ar plasmas, however, with a central frequency at  $\sim 37$  kHz as shown in Figure 9. The width of the frequency band remains same as that of Ar plasma. In Ar + He plasmas, the FP fluctuation magnitude reduced significantly ( $\sim 40\%$  ) as compared to He and Ar plasmas. The FFT of the fluctuations show a quite wider ( $\sim 50\%$  ) spectra lying between 20 kHz to 45 kHz and centred at  $\sim 35$  kHz with no distinct peak compared to Ar and He plasmas as shown in Figure 4.10. To establish the observed instability in Ar, He and Ar + He plasmas to be indeed an ion-ion counter streaming instability we first derive the dispersion relation of this instability and obtained the  $\omega$  vs  $k$  plots, both for single ion-specie case (He and Ar) as well as for two ion-species case. To establish the observed instability to be indeed an ion-ion counter streaming instability we first derive the dispersion relation of this instability and obtained the  $\omega$  vs  $k$  plots.

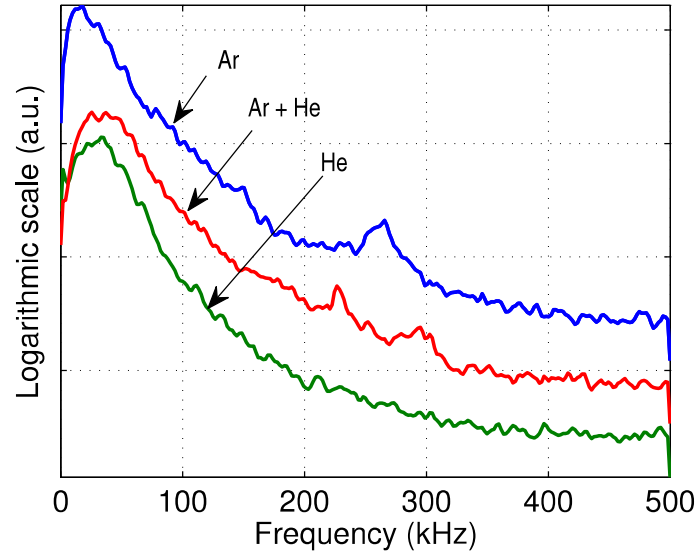


Figure 4.10: Power spectra of ion-ion counter streaming instability in logarithmic scale, in Argon, Helium and Ar+He multi ion species plasma.  $P_{fill} = 3 \times 10^{-3}$  mbar,  $n_e \sim 5 \times 10^8/cc$ ,  $T_e \sim 2-3$  eV.

## Dispersion relation for ion-ion counter streaming instability

### Single ion species plasma

The dispersion relation for ion-ion counter streaming instability in case of single ion species plasma is derived by linearizing the fluid equations for ions. Continuity equation for ions is given by,

$$\frac{\partial n}{\partial t} + \nabla \cdot (nV) = 0 \quad (4.1)$$

Furthermore, we have considered infinite, homogeneous plasma with counter streaming ions for deriving the dispersion relation.[8] Physical quantities can be represented as  $A(x, t) = A_0(x) + A_1(x, t)$  where  $A_0$  is the equilibrium part and  $A_1$  is the perturbed part.

Consider two counter streaming ion beams in one dimension with densities  $n_{\alpha 0}$ ,  $n_{\beta 0}$  and velocities  $V_{\alpha 0}, V_{\beta 0}$ . Linearized continuity equation can be written as,

$$-i\omega n_{\alpha 1} + ik(n_{\alpha 0}V_{\alpha 1} + n_{\alpha 1}V_{\alpha 0}) = 0 \quad (4.2)$$

$$-i\omega n_{\beta 1} + ik(n_{\beta 0}V_{\beta 1} + n_{\beta 1}V_{\beta 0}) = 0 \quad (4.3)$$

Considering ion momentum equation,

$$Mn_i \left[ \frac{\partial V}{\partial t} + (V \cdot \nabla)V \right] = eE - \nabla p - R_i \quad (4.4)$$

where  $R_i$  is the collisional term, which can be neglected in collisionless presheath conditions. Linearizing the momentum equation for ions, we get

$$Mn_{\alpha 0}[-i\omega V_{\alpha 1} + ikV_{\alpha 0}V_{\alpha 1}] = -en_0 ik\phi_1 - \gamma_i k_B T_i ikn_1 \quad (4.5)$$

$$Mn_{\beta 0}[-i\omega V_{\beta 1} + ikV_{\beta 0}V_{\beta 1}] = -en_0 ik\phi_1 - \gamma_i k_B T_i ikn_1 \quad (4.6)$$

where  $\gamma_i$  is the ratio of specific heat for ion fluid and  $T_i$  is the ion beam temperature.

Using eq. 4.2, 4.3, 4.5 and 4.6, we get

$$V_1 = \frac{ek\phi_1}{m(\omega - kV_0)} + \frac{\gamma_i k_B T_i ik}{n_0 M} n_1 \quad (4.7)$$

$$n_{i1} = \frac{en_0 k^2}{M[(\omega - kV_0)^2] - \gamma_i \vartheta_b^2 k^2} \phi_1 \quad (4.8)$$

where  $\vartheta_b = \sqrt{\frac{k_B T_i}{M}}$ ,  $T_i$  is the temperature of the ion beam.

Electrons follow Boltzmann distribution i.e.,

$$n_e = n_0 \exp\left(\frac{e\phi}{k_B T_e}\right) \quad (4.9)$$

Assuming perturbations are small compared to electron thermal energy,  $e\phi \ll k_B T_e$

$$n_e = n_0 \left(1 + \frac{e\phi}{k_B T_e}\right) \quad (4.10)$$

Now, perturbed electron density becomes

$$n_{e1} = n_0 \left(\frac{e\phi}{k_B T_e}\right) \quad (4.11)$$

## Chapter 4. Ion-ion counter-streaming instability

---

Poisson equation gives

$$-ikE_1 = \frac{e}{\varepsilon_0}(n_{\alpha 1} + n_{\beta 1} - n_{e1}) \quad (4.12)$$

$$\phi_1 \left[ 1 + \frac{1}{k^2 \lambda_{De}^2} - \left( \frac{\omega_{pi}^2}{(\omega - kV_0)^2 - \gamma_i k^2 \vartheta_b^2} + \frac{\omega_{pi}^2}{(\omega + kV_0)^2 - \gamma_i k^2 \vartheta_b^2} \right) \right] = 0 \quad (4.13)$$

For two equal density and velocity beams in opposite direction, linear dielectric function becomes

$$\epsilon(\omega, k) = 1 + \frac{1}{k^2 \lambda_{De}^2} - \left[ \frac{\omega_{pi}^2}{(\omega - kV_0)^2 - \gamma_i k^2 \vartheta_b^2} + \frac{\omega_{pi}^2}{(\omega + kV_0)^2 - \gamma_i k^2 \vartheta_b^2} \right] \quad (4.14)$$

In the above equation, the term  $\frac{1}{k^2 \lambda_{De}^2}$  and  $\gamma_i k^2 \vartheta_b^2 \ll (\omega \pm kV_0)^2$ , which are neglected and the above equation becomes,

$$\epsilon(\omega, k) = 1 - \left[ \frac{\omega_{pi}^2}{(\omega - kV_0)^2} + \frac{\omega_{pi}^2}{(\omega + kV_0)^2} \right] \quad (4.15)$$

The solution for complex  $\omega$  is found from  $\epsilon(\omega, k) = 0$  which is quartic in  $\omega$  with four independent roots, which are

$$\omega = \pm \left[ k^2 V_0^2 + \omega_p^2 \pm \omega_p (4k^2 V_0^2 + \omega_p^2)^{1/2} \right]^{1/2} \quad (4.16)$$

From equ. 4.16 it is found that, when  $0 < \frac{kV_0}{\omega_p} < \sqrt{2}$ , two roots are real and two roots are imaginary and  $\frac{kV_0}{\omega_p} > \sqrt{2}$ , all roots are real. Figures. 4.11 and 4.12 are graphical solutions of the equ. 4.16 with function in the square brackets in equ 15,  $\left[ \frac{\omega_{pi}^2}{(\omega - kV_0)^2} + \frac{\omega_{pi}^2}{(\omega + kV_0)^2} \right] = Y$  on the y-axis and  $\omega$  on x-axis. The function (Y) equals to one gives the solutions. The minimum unstable wave number  $k_0$  value



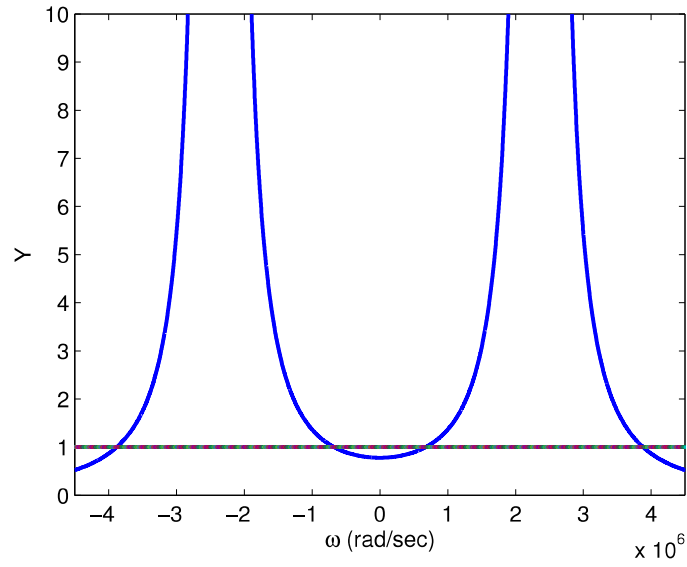


Figure 4.11: Function ( $Y$ ) vs frequency ( $\omega$ ) for  $\frac{kV_0}{\omega_p} > \sqrt{2}$ , in experimental conditions of ion plasma frequency 1 MHz. It is clear from figure that the dielectric response function has four real roots

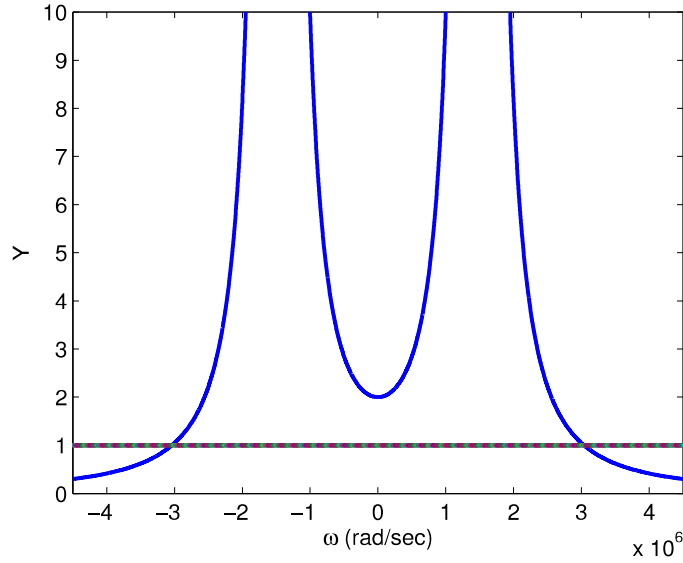


Figure 4.12: Function ( $Y$ ) vs frequency ( $\omega$ ) for  $0 < \frac{kV_0}{\omega_p} < \sqrt{2}$ , in experimental conditions of ion plasma frequency 1 MHz. It is clear from figure that the dielectric response function has two real roots and two imaginary roots.

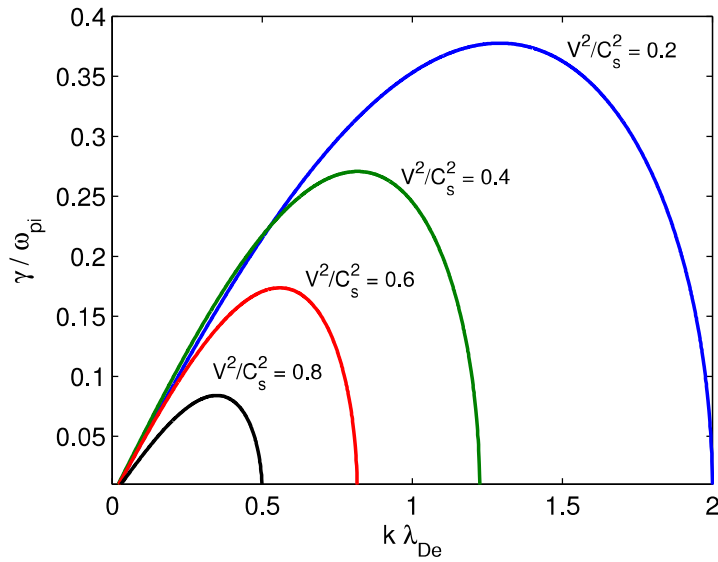


Figure 4.13: Growth rate of ion-ion counter streaming instability for  $V^2/C_s^2 = 0.2, 0.4, 0.6$  and  $0.8$  in presheath.

is obtained from the condition  $\frac{kV_0}{\omega_p} < \sqrt{2}$ , from which minimum unstable length required to grow modes exponentially is given by the condition,  $\frac{\omega_p L}{V_0} > \frac{2\pi}{\sqrt{2}}$  where  $L = \frac{2\pi}{k_0}$ . For typical plasma conditions,  $\omega_{pi} = 1.1$  MHz, and for beam velocity half of Bohm velocity, we get minimum unstable length to exponentially grow the mode as 6 mm.

Dispersion relation can be further improved by considering the factor  $k^2\lambda_{De}^2$  into account. Then equ.4.16 becomes,

$$\omega = \pm \left[ \frac{\omega_p^2 k^2 \lambda_{De}^2}{1 + k^2 \lambda_{De}^2} \left\{ 1 + \left( \frac{1 + k^2 \lambda_{De}^2}{k^2 \lambda_{De}^2} \right) \left( \frac{k^2 V^2}{\omega_p^2} \right) \pm \sqrt{1 + 4 \left( \frac{1 + k^2 \lambda_{De}^2}{k^2 \lambda_{De}^2} \right) \left( \frac{k^2 V^2}{\omega_p^2} \right)} \right\} \right]^{1/2} \quad (4.17)$$

In terms of growth rate  $\gamma$ ,

$$\frac{\gamma}{\omega_{pi}} = \left[ \frac{k^2 \lambda_{De}^2}{1 + k^2 \lambda_{De}^2} \left\{ -1 - \left( \frac{1 + k^2 \lambda_{De}^2}{k^2 \lambda_{De}^2} \right) \left( \frac{k^2 V^2}{\omega_p^2} \right) + \sqrt{1 + 4 \left( \frac{1 + k^2 \lambda_{De}^2}{k^2 \lambda_{De}^2} \right) \left( \frac{k^2 V^2}{\omega_p^2} \right)} \right\} \right]^{1/2} \quad (4.18)$$

For ion beam density  $n_i = \frac{1}{2}n_e$ , the above equation becomes,[117]

$$\frac{\gamma}{\omega_{pi}} = \left[ \frac{k^2 \lambda_{De}^2}{1 + k^2 \lambda_{De}^2} \left\{ -1 - 2 \left( 1 + k^2 \lambda_{De}^2 \right) \left( \frac{V^2}{C_s^2} \right) + \sqrt{1 + 8 \left( 1 + k^2 \lambda_{De}^2 \right) \left( \frac{V^2}{C_s^2} \right)} \right\} \right]^{1/2} \quad (4.19)$$

where  $C_s$  is the ion Bohm velocity. The growth rates are plotted for different Mach numbers ( $V/C_s$ ) in Figure 4.13.

Further from the growth rate plot Figure 4.13, for the central frequency of the peak  $\sim 20$  kHz,  $k\lambda_{De}$  comes out to be  $\sim 0.1$  for all the growth rates. Hence the wavenumber  $k$  is 0.15 for  $\lambda_{De} \sim 0.7$ . Therefore the wavelength of the wave should be  $\sim 4$  cm at the observed frequency.

## Two-ion-species plasma

In case of two-ion species the dispersion relation is derived taking into consideration the population of both the ion species drifting towards and away from the mesh-grid. Considering infinite, homogeneous plasma, the linear dielectric function becomes,

$$\epsilon(\omega, k) = 1 + \frac{1}{k^2 \lambda_{De}^2} - \frac{\omega_{p1}^2}{(\omega - kV_0)^2} - \frac{\omega_{p2}^2}{(\omega - kV_0)^2} - \frac{\omega_{p1}^2}{(\omega + kV_0)^2} - \frac{\omega_{p2}^2}{(\omega + kV_0)^2} \quad (4.20)$$

where  $\omega_{p1}$  and  $\omega_{p2}$  are the ion plasma frequencies of Argon and Helium ions respectively.

The solution for complex  $\omega$  is found from  $\epsilon(\omega, k) = 0$ , which is a quartic equation in  $\omega$ . i.e.,

$$\Omega^4 \left( \frac{1 + K^2}{K^2} \right) - 2\Omega^2 [4M^2 (1 + K^2) + (1 + \omega_{pr}^2)] + 8K^2 M^2 [2(1 + K^2) M^2 - (1 + \omega_{pr}^2)] = 0 \quad (4.21)$$

where,  $\Omega = \left( \frac{\omega}{\omega_{p1}} \right)$ ,  $K = k\lambda_{De}$ ,  $M$  is the mach number  $\left( \frac{V_0}{C_s} \right)$ ,  $\omega_{pr} = \left( \frac{\omega_{p2}}{\omega_{p1}} \right)$ ,  $\omega_{p1}$ ,  $\omega_{p2}$  are Argon and Helium ion plasma frequencies and ion densities  $n_{i1} = n_{i2} = \left( \frac{n_e}{4} \right)$

The growth rates obtained from the roots of the equ. 4.21 are plotted in Figure 4.14.

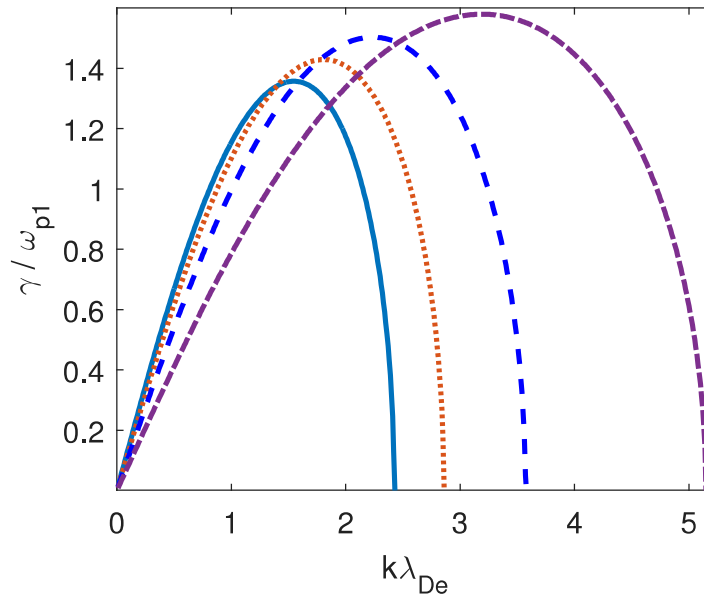


Figure 4.14: Normalized growth rates for ion-ion counter streaming instability in two-ion-species (Ar-He) plasma for different Mach numbers ( $M = V/C_s$ ),  $M^2 = 0.8$  (solid line), 0.6 (dotted line), 0.4 (dashed line), 0.2 (dash-dot line), with  $\omega_{pr} = \omega_{p2}/\omega_{p1} = \sqrt{10}$

### Discussion

When a mesh grid is placed inside the plasma, a sheath is produced on either side of it. In the sheath on either side, if ionization is neglected then three categories of particles are probable to exist. They are electrons, ions entering from the bulk plasma and ions entering from the sheath of other side of mesh grid through the mesh grid. On one side (say S1 as shown in Figure 4.15) of the mesh grid, the ions enter the sheath with Bohm velocity[1] after getting accelerated in the presheath of S1. The ions entering into S1 through the mesh grid from the other side (say S2), accelerated in presheath of S2, will also have Bohm velocity at sheath edge of S1 as they are being retarded by the potential of the grid. Therefore, the ion velocities in sheath S1 of both the ions coming from bulk plasma as well as from the S2 through mesh grid remain the same. The similar situation will arise in the sheath-presheath region of S2. Therefore the system can be considered to be a counter-streaming ion-ion system in the sheath-presheath of both sides S1 and S2. The experimental evidences related to the observation of spectral peak in the frequency spectra of floating potential fluctuations of mesh grid and a LP placed in the sheath-presheath region of Ar, He and Ar + He plasmas, provided in section III, clearly indicate a presence of ion-ion counter streaming instability. Theoretical estimate of wave number at the observed frequency from the dispersion relation Equ. 4.17 for this instability gives a value  $0.15 \text{ mm}^{-1}$ . To establish further the instability to be the ion-ion counter streaming instability, we deduced the wave number from the simultaneous measurement of floating potential fluctuations from grid and Langmuir probe. Figure 4.3 shows fluctuation data

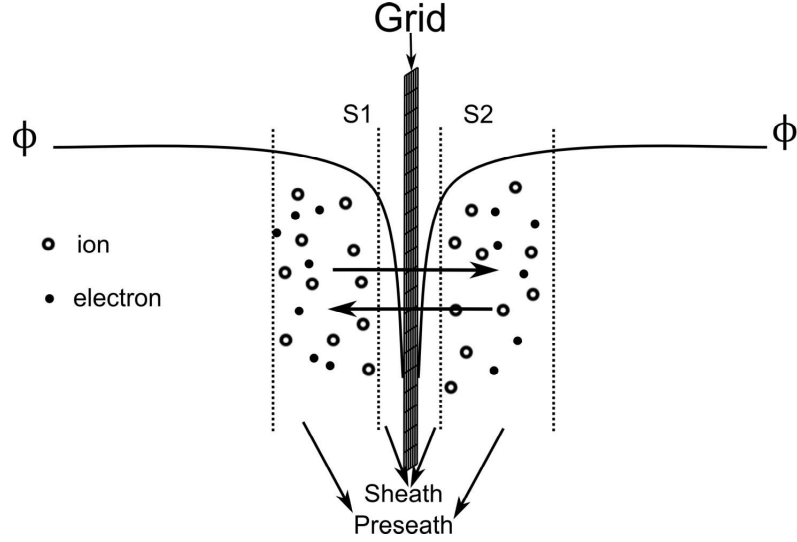


Figure 4.15: Schematic diagram of Sheath-Presheath produced on both side of mesh grid immersed in plasma. Arrow indicates counter streaming of ions across the mesh grid from either side, accelerated through potential well

from both grid and Langmuir probe, which is placed 5 mm away from the mesh grid. The cross-correlation between time series data of Grid and Langmuir probe plotted in Figure 4.16 shows a time delay of 5 microseconds in the frequency range of 10-30 KHz. This time lag between the signals is further verified by plotting the floating potential fluctuation data filtered between 20 - 22 kHz measured by mesh grid and the LP as shown in Figure 4.17. With the separation between grid and LP 5 mm, the time delay  $\sim 5 \times 10^{-6}$  seconds gives the phase velocity of  $\sim 1$  km/sec. The phase velocity of  $\sim 1$  km/sec with the frequency of the wave  $\sim 20$  kHz gives a wave number,  $k \sim 1.25$  /cm and hence a wavelength,  $\lambda \sim 5$  cm. The measured  $\lambda$  of the instability matches quite well with that calculated from the dispersion relation. After thoroughly establishing the presence of ion-ion counter streaming instability in sheath-presheath region of immersed mesh-

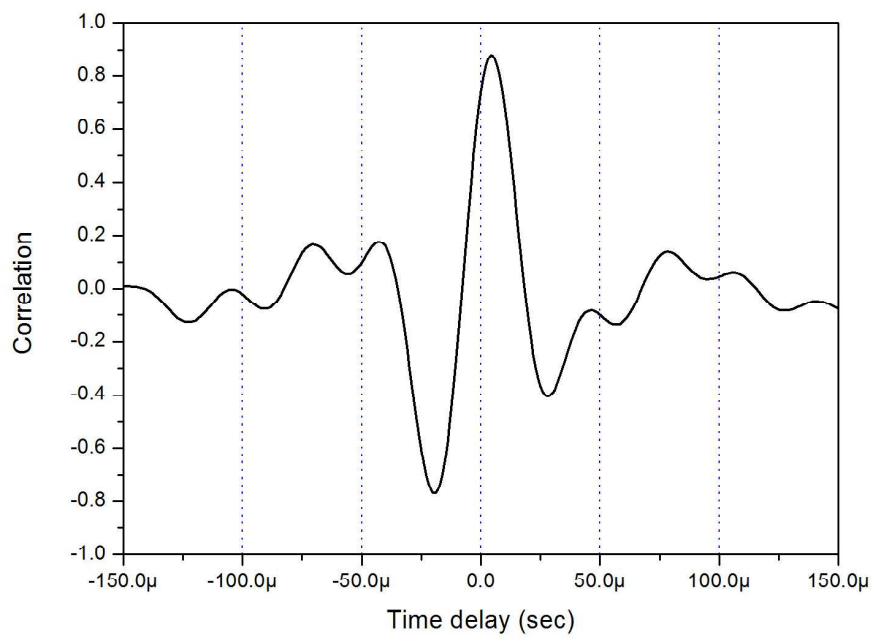


Figure 4.16: Correlation between time series data of Langmuir probe and Grid showing a time delay of 5 micro seconds



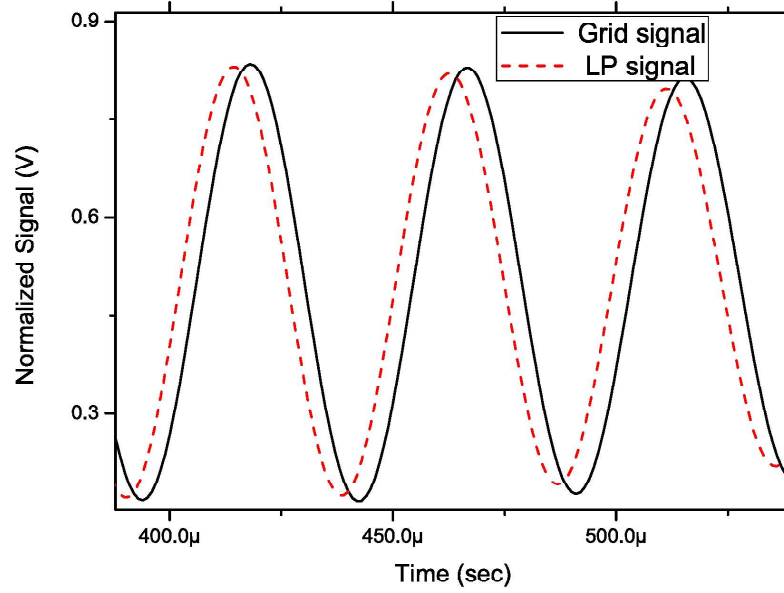


Figure 4.17: Grid and Langmuir probe floating potential fluctuation signal, filtered between 20-22 kHz.

grid in Argon plasma, the experiments are repeated in He plasma as well as in Ar + He plasma. In He plasmas, the centre of the broadband peak has been observed at higher frequency ( $\sim 37$  kHz) compared to Argon plasmas ( $\sim 17$  kHz) in similar experimental conditions. This result is in accordance with the derived dispersion relation for the ion-ion counter instability that, frequency of instability is the function of ion plasma frequency and the same ion density, Helium has larger ion plasma frequency than Argon because of its less atomic weight. Further, in the Ar + He plasma, the frequency spectra of floating potential fluctuations measured by both the grid and LP show a broader spectra lying between 20 kHz to 45 kHz with no distinct peak in similar experimental conditions. The broadening of the frequency spectra in this case is almost 50 % more than that observed in Ar and He single species plasmas indicating excitation of more number of  $k$ 's in case of two ion

species plasmas. This experimental result validates the theoretical prediction of excitation of wider range of  $k$  values in the two species (Ar + He) plasma compared to single specie (Ar or He) plasmas. The derived dispersion relations (Figure 4.13 and 4.14) of the instability clearly show that the growth rate of the instability is higher for wider range of  $k$  for two species plasma. Furthermore, the predicted frequency at the measured  $k$  in the Ar + He plasma from the dispersion relation (Figure 4.14) for two ion species plasma matches quite well with the centre of the broadband spectra at  $\sim 35$  kHz. Based on the evidences described above, it can be concluded that the observed instability in the presheath-sheath region of the mesh grid placed inside the Ar, He and Ar + He plasma is due to the ion-ion counter streaming instability.

### Effect of Mass Ratio on the instability

The mass ratio effect on counter streaming instability growth is important to know for various combination of ions. Figure 4.18 shows growth rate plots for ion mass ratio 10, 20, 50 and 100. From the figure, the growth rates for high Mach numbers increases with increase in the ion mass ratio, which shows the effective growth rate for higher mass ratio. The existing wave numbers also increases with increasing mass ratio.

### Summary

Broadband frequency peaks in the range 10-20 kHz, 25-40 kHz and 20 - 50 kHz are observed in the frequency spectra of the floating potential fluctuations of mesh-grid

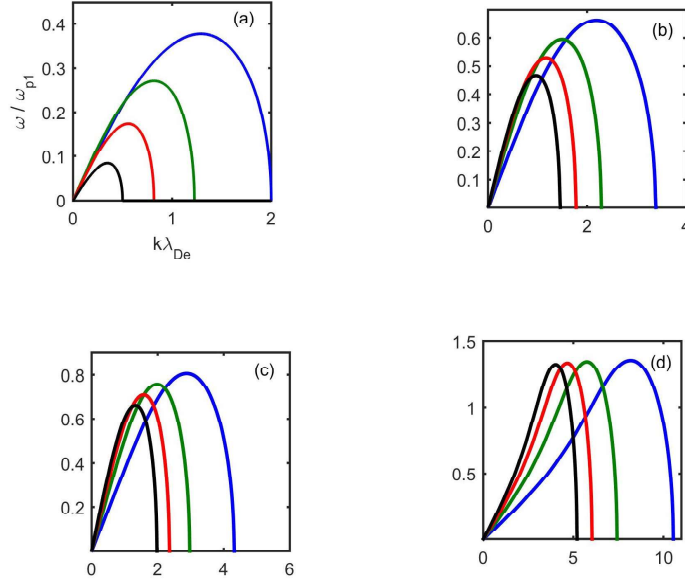


Figure 4.18: Grid and Langmuir probe floating potential fluctuation signal, filtered between 20-22 kHz.

immersed in Argon, Helium and Argon + Helium plasmas respectively. Identical spectral peaks are also observed in floating potential fluctuations measured with Langmuir probe placed in the sheath-presheath region of mesh grid. The spectral peak's central frequency and width are found to be varying systematically with the discharge current and neutral pressure indicating the associated instabilities direct dependence on plasma density. The instability is suppressed when the mesh grid is covered with Aluminum foil from one side and also with biasing the mesh grid in the electron saturation region. These observations firmly indicated the instability to be an ion-ion counter streaming instability, generated by motion of ions through the mesh grid. The existence of the ion-ion counter streaming instability in the vicinity of the mesh grid is confirmed by measuring the wavenumber of  $k$ , value of

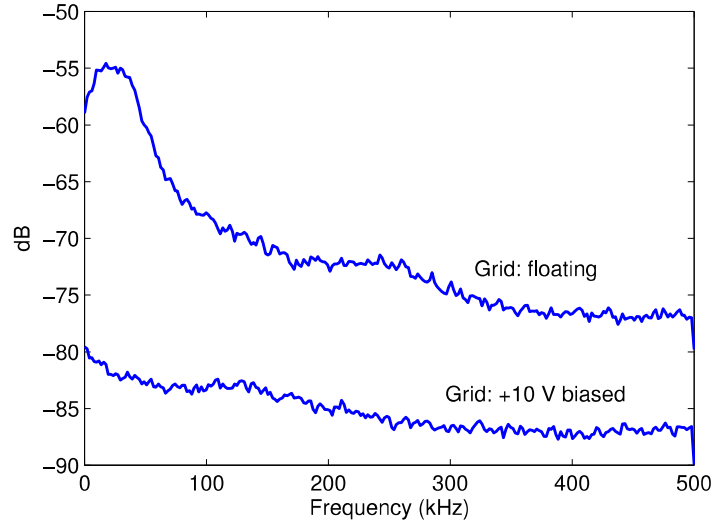


Figure 4.19: Frequency plot with grid in floating and biased in the electron saturation regime (+10 V)

which matches quite well with that obtained with theoretical dispersion relation of the instability in case of all the three plasmas. More broadening of frequency spectra in case of Ar + He plasma compared to the single specie (Ar or He) plasma, validates the theoretical prediction of higher growth rates for wider range of  $k$  values in two ion species plasmas. The suppression of the instability in the high pressure region by ion-neutral collisions further substantiate the involvement of ions is generating this instability.

# 5

## Ion-ion co-streaming instability in the presheath of two-ion species plasma

### Introduction

Sheath is a non-neutral region, which exists between quasi-neutral plasma and any physical surface in contact with plasma. As mentioned in chapter 1, formation of ion sheath requires ions to attain velocity greater than or equal to Bohm velocity. These entry velocities of ion species at the sheath edge is studied from long time. Bohm first derived the condition for entry velocity of ions at the sheath for a stable

sheath formation. The Bohm criterion states that ions should reach the sheath edge with a minimum velocity  $C_s = \sqrt{kT_e/m_i}$ . In unmagnetized, single ion species plasma, Bohm criterion is experimentally verified by measuring the ion velocities at the sheath edge. But in case of multi-ion species plasma there are questions still remain in the contest of valid flow velocities at the sheath edge. Riemann derived the generalized bohm criterion for multi-ion species plasma, which is given by

$$\sum_i \frac{n_{io}}{n_{eo}} \frac{C_{si}^2}{v_i^2} \leq 1 \quad (5.1)$$

where,  $C_{si}$  is the bohm velocity of the  $i^{th}$  ion species. However, this conditions does not reveals the exact entry velocities of individual ions. Several theories suggested that ions enter the sheath edge with their individual Bohm velocities [55, 118, 119].

Laser Induced Fluorescence (LIF) technique provides experimental measurements of ion velocity distribution function and ion flow speeds. Pioneering work by Severn *et al* in 2003 [23], in which the  $Ar^+$  velocities are measured near the sheath edge using LIF technique in Ar+He plasma, raises curtains for ion flow speeds measurements at the sheath experimentally in two-ion species plasma. In these experiments, they found for nearly equal ion concentrations,  $Ar^+$  reached the sheath edge with velocities more than their individual Bohm velocity, approaching system sound speed. Later, experiments are carried in Ar+Xe plasma with two LIF schemes to measure both  $Ar^+$  and  $Xe^+$  velocities at the sheath edge by D.Lee *et al* [62]. They found, both  $Ar^+$  and  $Xe^+$  reaches the sheath edge with system sound speed. In order to explain these results, Baalrud proposed a theory that suggests, ion-ion two-stream instability enhances the ion-ion collision friction, which leads to the equal velocities of ion species [8]. This theory also predicts, the

growth of the instability is maximum for equal ion concentrations. Hershkowitz *et al*, verified this theory, by measuring ion velocities for different ion concentration ratios. The results are in well agreement with the theory [63]. This theory proves its significance with the time with various frontier works [9, 11, 120].

In two or multi ion species plasma, the streaming of ions with differential velocities can cause ion-ion two-stream instability and the system is unstable to the instability. Apart from its existence in sheath-presheath regime, this instability also found in space plasmas. When the instability exists, it can enhance the friction force and anomalous ion heating can take place. This anomalous ion heating by the instability has been extensively studied in space plasma where the differential flow of ion species possible in ionospheric region.[15, 53, 54] The auroral zone is the one of the most prominent region for ion-ion two-stream instability to exist. The ionospheric ions (e.g.,  $H^+$ ,  $He^+$  and  $O^+$ ) can flow with differential speeds by virtue of difference in their mass. The linear theory for ion-ion two-stream instability under auroral conditions has been evaluated by different authors [15, 121, 122]. It is shown that the differential ion flow can cause instability, which can lead to strong heating of ions with net energy being transferred from lighter ions to heavier ions.

Although, much attempts has been made to detect the ion-ion co-streaming instability in the presheath regime, no direct measurement of this instability in this region has been reported. In this chapter, we report for the first time, the experimental observation of ion-ion co-streaming instability in the presheath regime.

### Plasma parameter regime

Experiments are carried in the same device described in chapter 2. Similarly as done in the ion-ion counter-streaming experiments in the Chapter-4, a SS mesh grid used to produce sheath-presheath and kept floating in the plasma at the middle of the chamber. There is no external bias applied to the grid in these set of experiments. Discharge is operated with application of discharge voltage - 80 V which drives discharge current in the range of 0.6 - 1.2 A, depending on the filling pressure. Typical plasma parameters are: plasma density,  $n_e \sim 3 \times 10^8 - 2 \times 10^9 / \text{cc}$  and electron temperature,  $T_e \sim 3 - 4 \text{ eV}$ . For producing Ar+He two-ion species plasma, two Mass flow controllers have been used. As the ionization rate coefficient of Argon and Helium is different, the equal neutral concentrations will not produce equal ion concentrations in the discharge. It has been demonstrated by Severn *et al* that  $0 \leq \left( \frac{n_{He}}{n_e} \right) \leq 0.5$  can be obtained with the neutral pressure ratio  $0 \leq \left( \frac{P_{He}}{P_{Ar}} \right) \leq 25$  [23]. Initially a low pressure argon plasma is produced with a filling pressure  $\sim 2 \times 10^{-4} \text{ mbar}$  and then Helium gas is introduced with another mass flow controller with partial pressure  $3 \times 10^{-3} \text{ mbar}$ , to take the ratio of partial pressures  $n_{He}/n_{Ar} \sim 15-18$  and beyond to study the existence of ion-ion co-streaming instability. This neutral pressure ratio is varied to observe the behavior of the instability.

An axially movable cylindrical Langmuir probe made up of tungsten having length of 5 mm and diameter 0.7 mm is used to measure the floating potential in the sheath, presheath, bulk plasma and its cylindrical surface is placed parallel to the surface of the mesh grid. For floating potential measurements, the probe



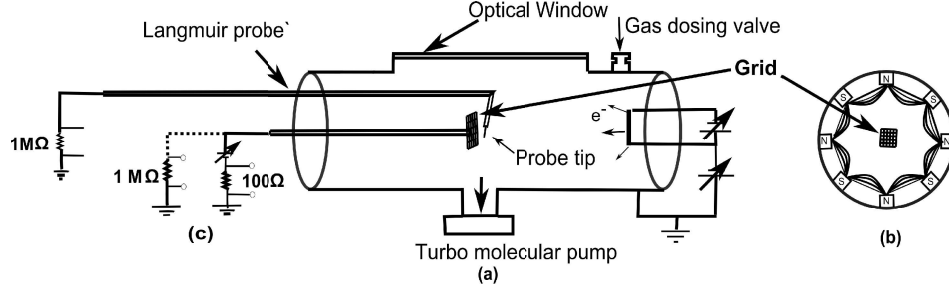


Figure 5.1: (a) Schematic diagram of the experimental set-up. (b) Cross-sectional view showing surface cusp magnetic field (c) Circuit diagram for Grid and Langmuir probe.

is terminated to a high resistor  $1 \text{ M}\Omega$  and the voltage across the resistor is fed into the oscilloscope. Floating potential fluctuations from both Langmuir probe and grid are recorded. A planar Langmuir probe is also employed for density and temperature measurements in the bulk plasma by using I-V traces, obtained using a variable power supply.[116]

## Experimental Results and Discussion

These set of experiments are carried out in two-ion species plasma formed using Argon and Helium gases for observing the ion-ion co-streaming instabilities in the presheath-sheath region of sheath system formed inside the plasma. As being predicted theoretically, the growth rate of the ion-ion co-streaming instability is maximum when the ratio of two ion concentrations in plasma becomes unity. Furthermore, previous experimental results show that, in the He + Ar plasmas produced with ratios of He and Ar pressures i.e.,  $\left(\frac{P_{He}}{P_{Ar}}\right)$  in the range of  $0 \leq \left(\frac{P_{He}}{P_{Ar}}\right) \leq 25$ , the ratio of He ions to the electron density i.e.,  $\left(\frac{n_{He^+}}{n_e}\right)$  in the

range of  $0 \leq \left(\frac{n_{He}^+}{n_e}\right) \leq 0.5$  can be obtained [23]. Based on the growth rate estimation using ion-ion co-streaming instability as described later, the growth rate maximizes for  $\left(\frac{n_{He}^+}{n_e}\right) \sim 0.35 - 0.5$ . This concentration of He<sup>+</sup> ion may therefore be expected at  $\left(\frac{P_{He}}{P_{Ar}}\right)$  in the range of  $\sim 15$  to  $20$ . Hence, experiments are carried out by producing plasmas with Ar and He neutral pressure ratio  $\left(\frac{P_{He}}{P_{Ar}}\right) \sim$  varying from  $5$  to  $18$  while keeping the total neutral pressure at  $\sim 3 \times 10^{-3}$  mbar. Depending upon the calibration of pressure guages, an error of  $5 - 10 \%$  is expected in the pressure measurement. As described in chapter 2, the neutral pressure ratios of Ar and He in Ar + He mixture plasmas are maintained by the calibrated flow rates in the mass flow controllers. The flow rates are calibrated by measuring the pressure inside the chamber. The presence of both the species are ensured by measuring the emission spectra of both the neutrals. Figure 5.2 shows the emission spectra from He + Ar plasmas. The figure clearly shows the presence of both Ar I and He I in Ar + He mixture plasma. The discharge current is in the range of  $1.0 - 1.2$  A at a constant discharge voltage of  $- 80$  V. At each neutral pressure ratio (from  $5 - 18$ ), the plasma is formed and after providing a sufficient stabilization time, the floating potential of the grid and Langmuir probe placed in the presheath region of the mesh is recorded. Figure 5.3 shows the time series data of the floating potential fluctuations from grid and Langmuir probe for  $\left(\frac{P_{He}}{P_{Ar}}\right) \sim 18$ . As described earlier these time series data of floating potential is analyzed to obtain their frequency spectra. Figure 5.4 shows the power spectra of the floating potential fluctuations from grid and Langmuir probe. The figures clearly show that there exist two distinct broad band peaks, one low frequency peak at  $\sim 20 - 40$  kHz and second high frequency peak at  $\sim 150 - 300$  kHz, in both the grid

and LP floating potential signals. Note here that in order to reduce the zero frequency response, floating potential time series data have been filtered through a high pass filter having lower cut-off at kHz. The low frequency peak at 20 - 40 kHz is identified as ion-ion counter streaming instability described in previous chapter. The high frequency peak has not been observed in case of single species plasma at similar experimental conditions. Further, the LP placed in the presheath region for fluctuation measurement is moved away from the grid and measurements are made in presheath and in the bulk plasma region away from the sheath system around the mesh grid. Figure 5.5 compares the frequency spectra of the floating potential fluctuation measured with LP in presheath region (red - solid line) and in the bulk plasma (blue - dotted line). Both the peaks at  $\sim 20$ -40 kHz and at  $\sim 150$ -300 kHz range in the frequency spectra exist only in presheath region while they vanish in the bulk region. The high frequency ( $\sim 150$  - 300 kHz), which only appears in the presheath region in two-ion species plasma is a clear signature of presence of ion-ion co streaming instability in the presheath region of a mesh grid immersed in the plasma. The experiments have been repeated several times on different days and similar results have been obtained.

After observing the presence of an instability in the frequency range of  $\sim 150$  -300 kHz in the presheath region with approximately equal ion concentration of both ions in a two ion species plasma, which is most likely the ion-ion co-streaming instability, the ratio of ions are varied systematically by increasing/decreasing the Ar/He gas and the variations in the observed spectral peak in the range of 150 - 300 kHz is recorded. The increase/decrease of Ar/He is monitored by increase/decrease in the intensity of ArI/HeI spectral lines. To start with, in the presence of the

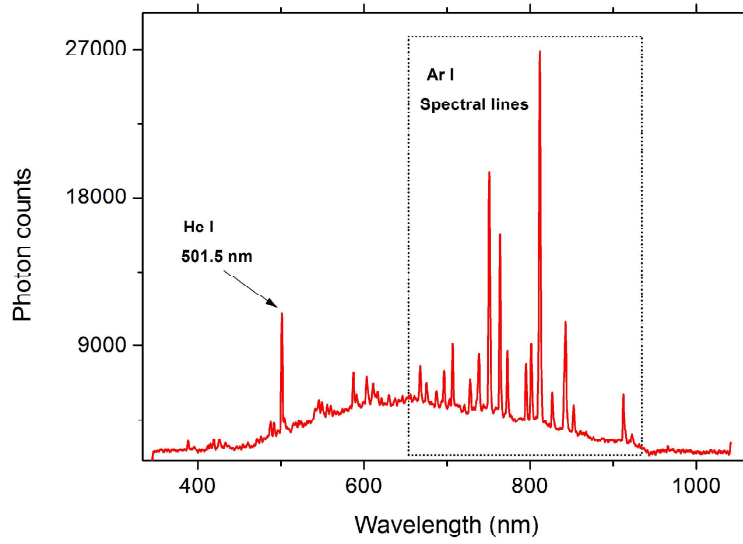


Figure 5.2: Wavelength spectra shows emission spectral lines from He I and Ar I in Ar+He plasma

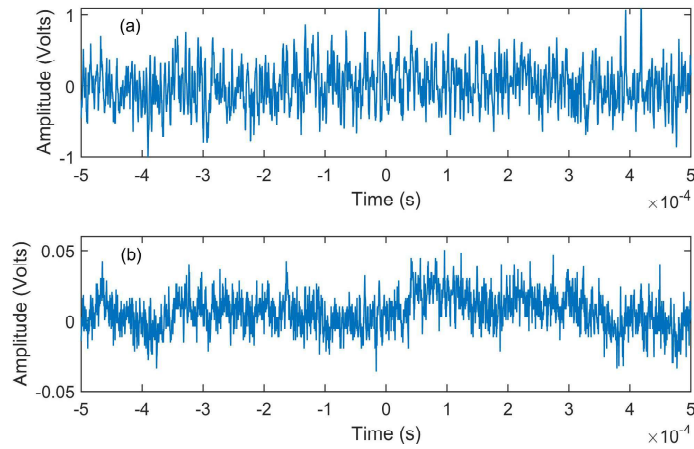


Figure 5.3: Time series data of floating potential fluctuations from (a) grid and (b) Langmuir probe

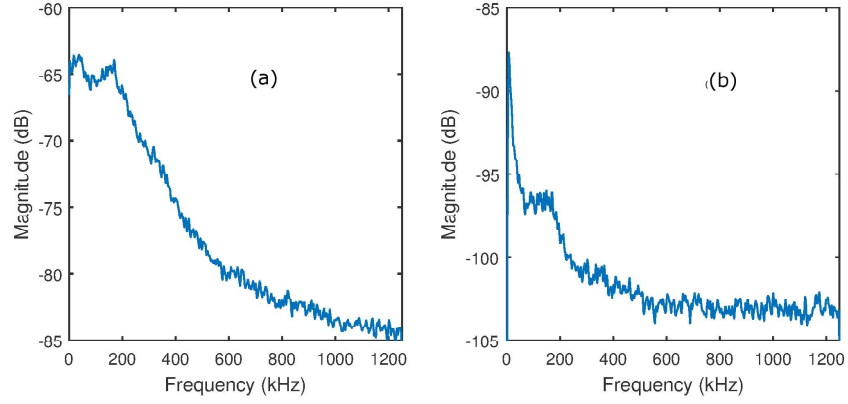


Figure 5.4: Frequency spectra of floating potential fluctuation signal from (a) grid and (b) Langmuir probe

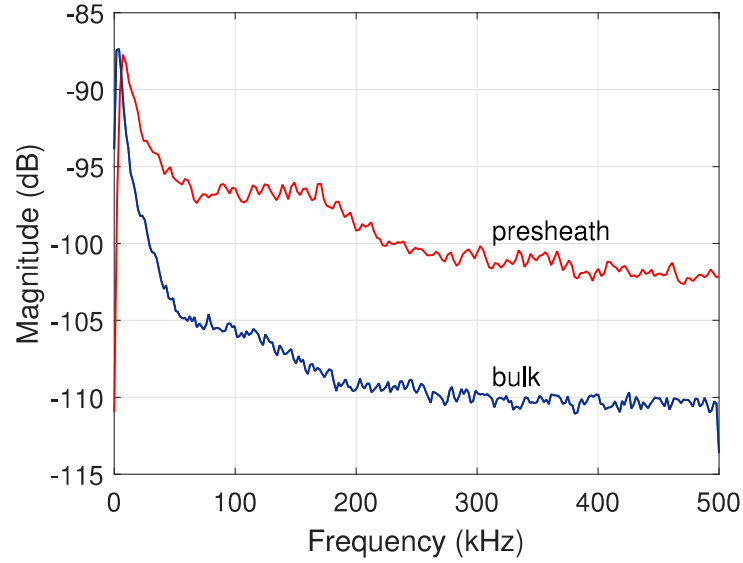


Figure 5.5: Comparison of frequency spectra of floating potential fluctuation signal from Langmuir probe from presheath and bulk plasmas

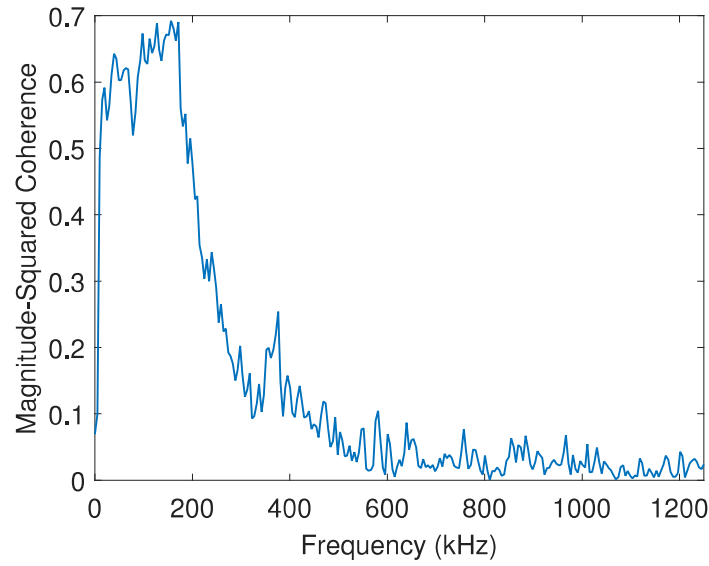


Figure 5.6: The coherence between time series signal from grid and Langmuir probe

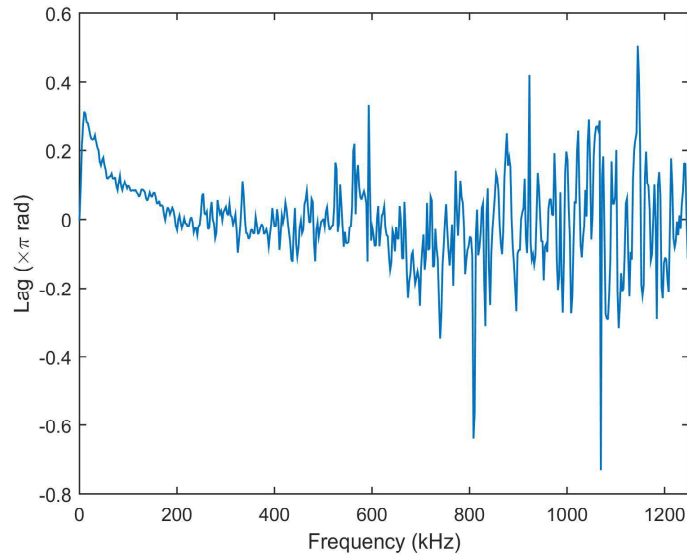


Figure 5.7: The phase lag vs. frequency obtained from floating potential fluctuation time series data from grid and Langmuir probe

instability with  $\left(\frac{P_{He}}{P_{Ar}}\right) \sim 18$ , the helium gas is suddenly turned off. It is observed that while the spectral peak at 20 - 40 kHz remained, but the spectral peak at 150 - 300 kHz vanished completely. Figure 5.8 shows the existence of 150 - 300 kHz peak in the plasma with neutral pressure ration of  $\left(\frac{P_{He}}{P_{Ar}}\right) \sim 18$  and the vanishing of the peak after sudden termination of the Helium flow. Again, these observations clearly suggest that the presence of two ion species is required for this instability at 150 - 300 kHz to be present. Next, to investigate the effect of neutral pressure ratio, which in turn varies the ion concentration ratio of both the ions, on the intensity of the instability, the neural pressure ratio is decreased gradually from 18 to 5 by increasing the Ar pressure. Figure 5.9 shows the frequency spectra of fluctuations from grid at different  $\left(\frac{P_{He}}{P_{Ar}}\right)$  ratios of 18, 10, 8 and 5. The amplitude of the peak at 150 - 300 kHz decreases as the  $\left(\frac{P_{He}}{P_{Ar}}\right)$  is decreased with its maximum at  $\left(\frac{P_{He}}{P_{Ar}}\right) \sim 18$ . The peak almost disappears at  $\left(\frac{P_{He}}{P_{Ar}}\right) \sim 5$ . Further, the central frequency of the band (150 - 300 kHz) also decreases as the ratio is lowered from 18 to 5. These observations of dependence of intensity of this instability on the ion concentration ratio further confirms the presence of ion-ion co-streaming instability in the presheath region.

To investigate further the origin of the spectral peak at 150 - 300 kHz in this two ion species plasma with equal ion concentration, the magnitude-squared coherence spectrum between the grid and LP signals has been obtained to check for the coherence between the two signals. The signals from the grid and LP are found to be highly coherent at 150 - 300 kHz frequency range as shown in Figure 5.6. Both these signals are then used to determine the phase velocity of the wave having frequency in the range of 150 - 300 kHz. First the time lag between the signals

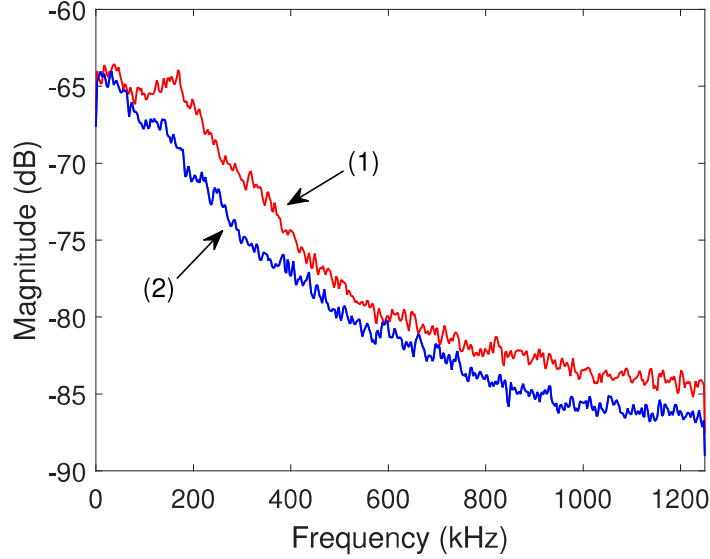


Figure 5.8: Frequency spectra of floating potential fluctuation signal from grid (1) in Ar-He plasma with  $\left(\frac{P_{He}}{P_{Ar}}\right) \sim 18$  (2) in Ar plasma after Helium flow is turned off

at the locations of grid and LP has been obtained by evaluating the cross power spectrum between the signals. The phase lag obtained with respect to frequency between the two signals is shown in Figure 5.7. Dividing the distance between grid and LP of  $\sim 2.5 \pm 0.5$  mm by the measured time lag of  $\sim 0.23 \mu\text{sec}$ , gives the phase velocity of the wave to be  $\sim 10.8 \pm 2.1$  km/sec. Taking the central frequency of the broad band peak  $\sim 200$  kHz, the wavenumber of the wave comes out to be  $\sim 100 \text{ m}^{-1}$ . The bulk plasma parameters of this two species plasma with  $\left(\frac{P_{He}}{P_{Ar}}\right) \sim 18$  is measured by another LP placed in the bulk plasma far away from the sheath system. The electron temperature and the density,  $T_e = 3$  eV and  $n_e = 2 \times 10^9/\text{cc}$  respectively are measured in the bulk plasma. Using these values of temperature and density, the system sound speed is calculated using the following



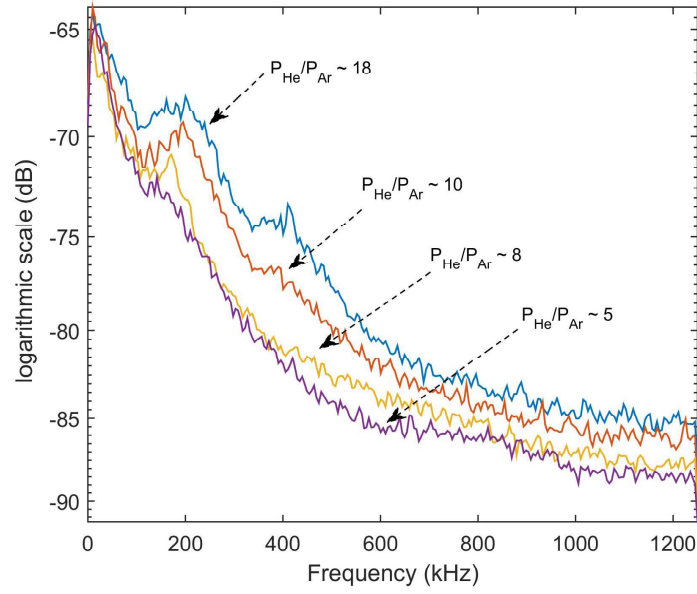


Figure 5.9: Variation of amplitude of the peak with partial pressure ratio  $\frac{P_{He}}{P_{Ar}} \sim 18, 10, 8$  and  $5$ .

formula  $C_s = \sqrt{\left(\frac{n_1}{n_e}\right) C_{s1}^2 + \left(\frac{n_2}{n_e}\right) C_{s2}^2}$ , where  $C_{s1}$  and  $C_{s2}$  are the individual Bohm speeds. The system sound speed comes out to be  $\sim 6.3$  km/sec.

To verify the instability with the theory, the observed frequency is compared with the frequency predicted by the linear fluid theory for ion-ion co-streaming instability. Using the dispersion relation of ion-ion co-streaming instability, the estimation of real frequency ( $\omega$ ) is attempted by using the measured value of wavenumber mentioned in previous paragraph. Also the comparison between the theoretically estimated maximum growth rate and the maximum measured intensity of the instability as a function of ion concentration ratio have been carried out.

The linear dielectric function for two ions streaming in the same direction (co-streaming) in the presheath with different velocities can be derived in similar way as done in case of counter-streaming instability presented in section 4.4. Assuming Maxwellian distribution, for ion waves with  $k\vartheta_{Ti} \ll (\omega - k.V_s) \ll k\vartheta_{Te}$  and  $T_i \ll T_e$ , the fluid plasma linear dielectric function of co-streaming instabilities is given by,

$$\epsilon(\omega, k) = 1 + \frac{1}{k^2 \lambda_{De}^2} - \left[ \frac{\omega_{p1}^2}{(\omega - kV_1)^2} + \frac{\omega_{p2}^2}{(\omega - kV_2)^2} \right] \quad (5.2)$$

Where  $\omega$  is the complex angular wave frequency,  $\omega_{p1}$ ,  $\omega_{p2}$ ,  $V_1$ ,  $V_2$  are the plasma frequency and velocities of the ion species 1 and 2 respectively. In order to determine the dispersion relation of the unstable modes, the quartic equation needs to be solve for obtaining the roots of Equation 5.2. Although the exact dispersion relation for each mode are analytically computable, they become very complicated. However, the unstable root can be computed by numerically solving equation 5.2. Further, as proposed by Baalrud et al [123], an approximate dispersion relation for

unstable root can be computed in the limit of  $k\lambda_{De} \leq 1$ . Taking  $\omega = \omega_R + i\gamma$ , the real frequency is given by,

$$\omega_R = k \sqrt{\left(\frac{n_1}{n_e}\right) \frac{C_{s1}^2}{C_s^2} V_1 + \left(\frac{n_2}{n_e}\right) \frac{C_{s2}^2}{C_s^2} V_2} \quad (5.3)$$

and growth rate

$$\gamma \approx \frac{k\Delta V \sqrt{\alpha}}{1 + \alpha} \sqrt{1 - \frac{k^2 \Delta V^2}{k^2 \Delta V_{up}^2} (1 + k^2 \lambda_{De}^2)} \quad (5.4)$$

where,  $\alpha = \frac{n_1}{n_2} \frac{M_2}{M_1}$  and  $\Delta V_{up}^2 = C_s^2 [1 + \sqrt{1 + 32\alpha/(1 + \alpha)^2}]$ . Figure 5.10 compares the growth rates obtained by numerically solving the equation 5.2 numerically and computed using the approximate growth rate from equation 5.4 for Ar + He plasma with equal ion concentrations, differential velocity  $\Delta V = C_{s1} - C_{s2}$ ,  $T_e = 3$  eV and  $n_e = 2 \times 10^9/\text{cc}$ . The growth rates match quite well proving the approximation reasonably accurate.

In order to confirm further the observed fluctuations in the 150 - 300 kHz range to be the ion-ion two streaming instability, the observed frequency at almost equal ion concentration and its variation with ion concentration ratio is compared with that predicted by the linear theory. Figure 5.11(a) shows the measured frequency variation with neutral concentration of two species. In these set of experiments, the peak of the broad band in the frequency spectra appears between 150-300 kHz, maximizes at 200 kHz for  $P_{He}/P_{Ar} \sim 18$ . In this case, the Ar pressure is increased and He pressure is decreased to deviate from the ratio of  $\left(\frac{P_{He}}{P_{Ar}}\right) \sim 18$  at which ion concentrations are approximately equal. As the concentration ratio reduced the frequency of the fluctuation are found to be reduced in accordance with prediction of the linear theory using Equation 5.2, as shown in Figure 5.11(b)

where the real frequency is plotted with ion concentration ratio for three values of wavenumber  $k$ . The top curve in Figure 5.11(b) is with  $k \sim 200 \text{ m}^{-1}$  (open circle with dash line), the central one is for  $k \sim 100 \text{ m}^{-1}$  (\* symbol with dotted line) and the third one is for  $k \sim 50 \text{ m}^{-1}$  (+ symbol with solid line). Using the measured wavenumber of the instability of  $\sim 100 \text{ m}^{-1}$ , Equation 5.3 gives the frequency of the instability is  $\sim 100 \text{ kHz}$  with approximately equal ion concentrations. However, the measured value of the frequency is  $\sim 200 \text{ kHz}$  (central peak of broadband spectra) for  $\left(\frac{P_{He}}{P_{Ar}}\right) \sim 15-20$  at which the ion concentrations of both the ions are approximately equal. This may be due to the fact that the measured wavenumber is for the Doppler shifted wave which is riding on the ions moving with system sound speed. Removing the Doppler shift from the measured phase velocity, the  $k$  value of the wave should be  $\sim 200 \text{ m}^{-1}$ . The estimated real frequency of the wave with  $k \sim 200 \text{ m}^{-1}$  using equation 5.3 [top curve of figure 5.11(b)] matches quite well with the experimentally measured values. The intensity of the broadband peak is also found to be reduced as the neutral concentration ratio of  $\left(\frac{P_{He}}{P_{Ar}}\right) \sim$  is reduced from 18. The measured intensity variation is shown in Figure 5.11(c). This observation is again consistent with the computed growth rates by solving the equation 5.2 numerically without any approximation. The variation of theoretical growth rates are plotted as a function of ion concentrations in Figure 5.11(d) for Ar + He plasmas. Figure 5.11(d) shows that for the Ar + He plasma, the growth rate maximizes at  $\left(\frac{n_{He}^+}{n_e}\right) \sim 0.35 - 0.5$  and decreased further as the He ion concentration is decreased. As mentioned earlier the Helium concentration is  $0 \leq \left(\frac{n_{He}}{n_e}\right) \leq 0.5$  in plasma produced with neutral pressure ratio  $P_{He}/P_{Ar}$  between 0 and 25[23]. Hence it is expected that for our experiments, where the maximum intensity is obtained

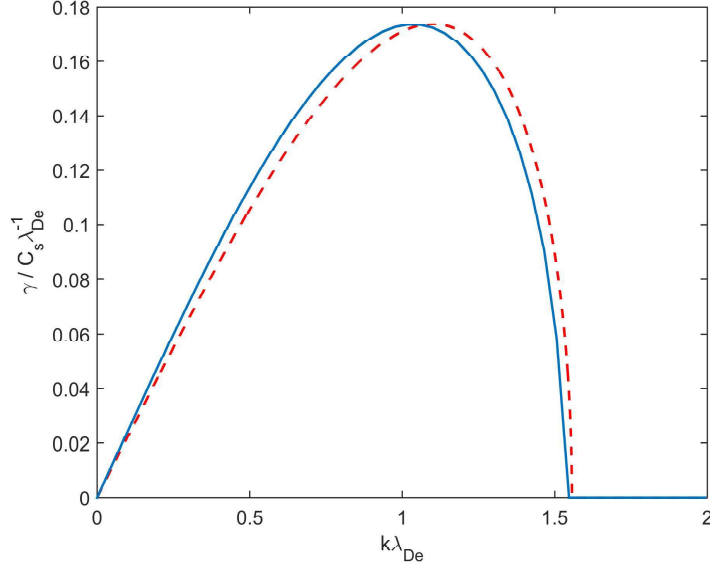


Figure 5.10: Normalized growth rates calculated for Ar+He plasma, solid line (-) by solving equ 5.2 numerically and dashed line (- -) from approximate growth rate equ 5.4 with  $\Delta V = C_{s1} - C_{s2}$ ,  $T_e = 3$  eV and  $n_e = 2 \times 10^9/\text{cc}$

in the plasmas produced with He and Ar neutral concentration of  $\sim 15 - 20$ , the ion concentration ratio is in the range of 0.35 - 0.5 and the intensity decreased further as the He pressure is reduced and Ar pressure is increased to bring the ratio of two further down.

Based on the experimental observations and above mentioned theoretical comparison, it can be definitely concluded that the ion-ion co-streaming instability has been excited in the presheath region of a sheath system formed around a mesh grid placed inside a weakly ionized low-pressure plasma.

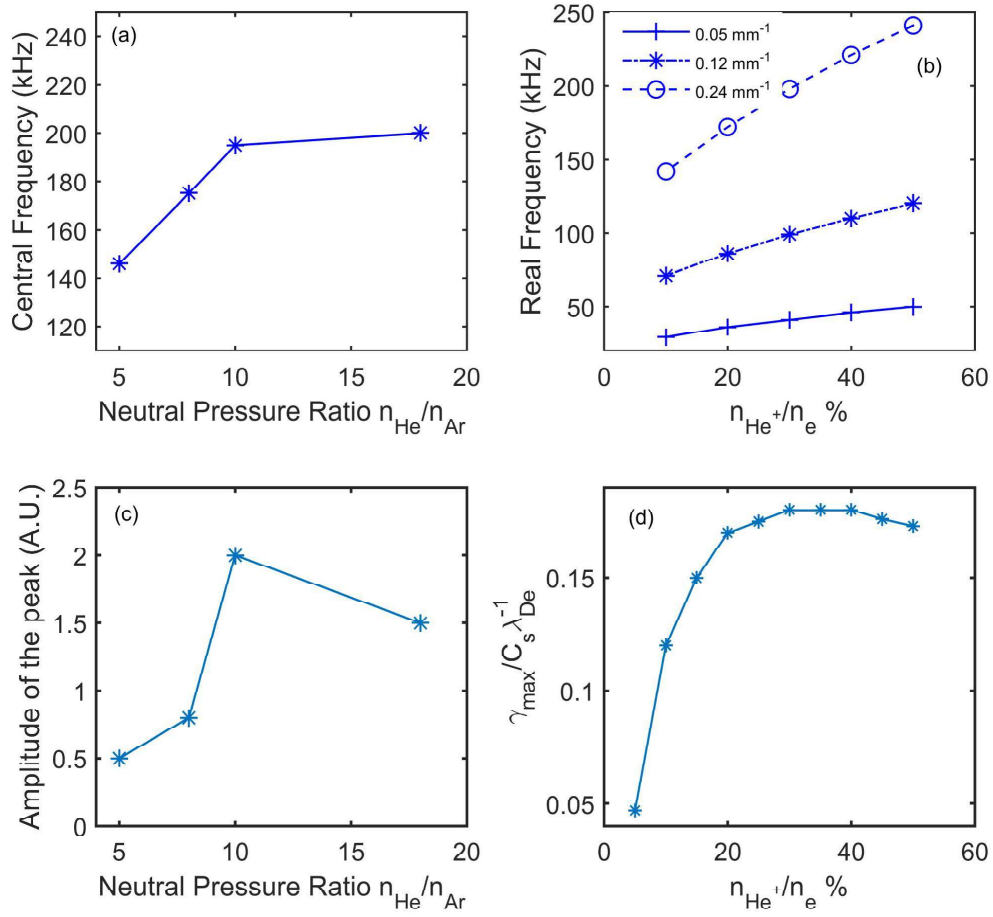


Figure 5.11: (a) Measured central frequency vs neutral pressure ratio (b) Real frequency obtained theoretically vs ion concentration ratio for different wavenumbers (k) (c) Measured amplitude of the peak vs neutral pressure ratio (d) Normalized maximum growth rate vs ion concentration ratio.

## Conclusions

Ion-ion co-streaming instability arising because of differential velocities of ion species is theoretically predicted to be existing in the presheath region of a sheath system present in a two ion species plasma. PIC simulations also confirmed its existence and are thought to be responsible for both the ion species to exit the plasma with equal velocity at the sheath boundary. However, no direct evidence of its experimental detection in the presheath is reported. We have observed this instability in the presheath region of a sheath system formed around a transparent mesh grid immersed in a low temperature, low pressure weakly ionized plasma. A broadband peak with a central frequency  $\sim 150 - 300$  kHz in the frequency spectra of floating potential fluctuations of grid and LP in He + Ar mixture plasma is identified as ion-ion co-streaming instability. The instability is only observed in the presheath region and remained absent in the bulk plasma. The intensity of the instability maximizes in the plasma produced with approximately equal ion concentrations of both the ion species and vanishes in a single species plasma with same experimental conditions as well as when the ion concentration ratio of He to Ar is reduced far below unity. The wavenumber  $k \sim 100 \text{ m}^{-1}$  is estimated using measured phase velocity  $\sim 11 \pm 2 \text{ km/sec}$ . The observed frequency of the instability matches well with the calculated real frequency from the dispersion relation of ion-ion co-streaming instability for approximately equal ion concentrations. The observed decrease in the frequency with ion concentration ratio far below unity is also consistent with the theoretical prediction. The intensity of the instability also maximizes at approximately equal ion concentration and decreases with decreasing

## Chapter 5. Ion-ion co-streaming instability

---

the concentration ratio again following the theoretical predictions. These experiments are the first direct experimental evidence of ion-ion co-streaming instability excited near the sheath edge in Ar + He two-ion species plasma.



# 6

## Self-excited ion-acoustic instability in the presheath of single-ion species plasma

### Introduction

In this chapter experimental observations of self-excited (no external means) ion-acoustic wave in the presheath region of a sheath-presheath formed around a mesh grid immersed in single-ion species Argon plasma and its detailed characterization is presented. Recent theoretical developments [11] have established the excitation of ion-acoustic instabilities in the presheath region by virtue of differential

flow speed between ions and electrons. The authors further went on to show that several interesting phenomena can be explained on the basis of existence of this instability in the presheath region. Enhanced collisional friction by this instability has been predicted to be the reason for thermalization of ions near the sheath edge. Langmuir's paradox, i.e., rapid thermalization of electrons to Maxwellian distribution in a low pressure plasma is anticipated to be due to enhanced electron-electron scattering in the presheath by the ion-acoustic instability enhanced collisions [67]. Furthermore, this instability is expected to affect the particle flow in the sheath presheath region and cause anomalous transport in the plasma boundary layers. It has also been suggested that the likely mechanism for the sustenance of both collisional and collisionless presheaths are partially by the collective process of ion-acoustic waves (IAWs). It is possible that the turbulent development of an IAW will yield not only particle fluxes of the right value, but also energy fluxes of the observed anomalous value in order to explain the inadequacy of the excess energy transmission factors for electrons and ions in presheath region [124].

Ion acoustic instability in plasmas is a subject of study as old as plasma physics itself and has been studied extensively both theoretically as well as experimentally. Ion heating, plasma particle transport are found to be significantly influenced by ion-acoustic instability. Hence much attention has been paid on this instability to understand the favorable conditions of its excitation and growth rates etc. in space as well as in laboratory plasmas. Several experiments have been carried out in which the ion-acoustic waves are excited in the plasma by different means such as by injecting electron and ion beams in the plasmas [19, 125, 126]. Spontaneous excitation of IAWs are also reported in current-carrying plasmas both

theoretically and experimentally. It has been shown that a uniform current carrying plasma is unstable to ion-acoustic instability if,  $T_e \gg T_i$  and  $\vartheta \geq \sqrt{\frac{kT_e}{M}}$  where  $\vartheta$  is the relative velocity between electrons and ions and  $C_s = \sqrt{\frac{kT_e}{M}}$  is the ion-sound speed. In weakly ionized plasmas where  $T_e \gg T_i$ , the excitation of IAWs are controlled by the competition between inverse electron Landau damping and collisional damping due to ion-neutral collisions.

However, to the best of our knowledge, the experimental observations of self excited ion acoustic waves in the presheath region are not yet reported. In the experimental observations presented in this chapter, appropriate plasma conditions based on the pressure threshold due to ion-neutral collisions are discovered in which the ion-acoustic waves are self-excited in the presheath region. After proper identification of the IAWs in the presheath region, the instability is characterized in detail by measuring its wavenumber and parametric evolution. The rest of the chapter is arranged as follows: Linear dispersion relation derivation is done in Section 6.2, working plasma parameter regime is described in Section 6.3. Experimental results are discussed in Section 6.4, followed by Discussion in Section 6.5.

## Linear Dispersion Relation

The electrostatic dispersion relation for an unmagnetized, homogeneous, infinite plasma can be expressed as

$$D(k, \omega) = 0 \tag{6.1}$$

## Chapter 6. Ion-acoustic instability

---

where  $\omega = \omega_r + i\gamma$  is a complex angular frequency and  $k$  is real wave number and the dielectric function is defined by

$$D(k, \omega) = 1 + \sum_j \frac{\omega_{pj}^2}{k^2} \int \frac{k \cdot \partial F_j / \partial v}{\omega - k \cdot v} \quad (6.2)$$

Although this dispersion relation is derived for homogeneous, infinite plasma, the wavelength being considered here are much smaller than the gradient scale length of plasma parameters in the presheath, so this dispersion relation is considered to hold in presheath region as well.[\[11\]](#)

Considering Maxwellian electron and ion distributions with a differential flow  $V_i$ ,  $f_{e,0} = n_e \exp(-v^2/v_{Te}^2)/(\pi^{3/2}v_{Te}^3)$  and  $f_{i,0} = n_e \exp(-(v - V_i)^2/v_{Ti}^2)/(\pi^{3/2}v_{Ti}^3)$ , the dispersion relation equ. [6.2](#) can be written in terms of  $Z'(\xi)$  as,

$$D(k, \omega) = 1 - \frac{\omega_{pi}^2}{k^2 v_{Ti}^2} Z'(\xi_i) - \frac{\omega_{pe}^2}{k^2 v_{Te}^2} Z'(\xi_e) \quad (6.3)$$

where  $Z'(\xi)$  is the derivative of the plasma dispersion function,  $\xi_i = \frac{\omega - k \cdot V_i}{k v_{Ti}}$  and  $\xi_e = \frac{\omega}{k v_{Te}}$ .  $v_{Ti}$  and  $v_{Te}$  are the ion and electron thermal velocities respectively.

For  $T_e \gg T_i$ , the phase velocity of the wave will be much greater than ion thermal velocity and much less than electron thermal velocity i.e.,  $v_{Ti} \ll \frac{\omega}{k} \ll v_{Te}$ , and the asymptotic expansions of plasma dispersion function for large and small values of arguments are,

$$Z(\xi_j) \simeq -\frac{1}{\xi_j} - \frac{1}{2\xi_j^3} - \frac{3}{4\xi_j^5} - \dots \text{for } |\xi_j| \gg 1 \quad (6.4)$$

and

$$Z(\xi_j) \simeq -2\xi_j + \frac{4}{3}\xi_j^3 - \dots + i\sqrt{\pi} \frac{k}{|k|} \exp(-\xi_j^2), \text{ for } |\xi_j| \ll 1 \quad (6.5)$$

Using equs. 6.4 and 6.5, solving the dispersion relation from  $D(k, \omega) = 0$ , assuming  $\text{Im}(\omega) \ll \text{Re}(\omega)$ , we can obtain real part of the wave frequency is

$$\omega_r = k \cdot V_i - \frac{kC_s}{\sqrt{1 + k^2\lambda_{De}^2}} \quad (6.6)$$

and the growth rate equation is

$$\gamma = -\sqrt{\frac{\pi}{8}} \frac{k\lambda_{De}\omega_{pi}}{(1 + k^2\lambda_{De}^2)^2} \left\{ \left( \frac{T_e}{T_i} \right)^{3/2} \exp\left( -\frac{T_e/T_i}{2(1 + k^2\lambda_{De}^2)} \right) + \sqrt{\frac{m_e}{m_i}} \left( 1 - \frac{V_i}{C_s} \sqrt{1 + k^2\lambda_{De}^2} \right) \right\} \quad (6.7)$$

Figure 6.1 shows the growth rate for ion-acoustic instability with  $V_i = 0.9 C_s$  corresponds to near the sheath edge and  $T_e/T_i = 100$ . The maximum growth rate shows the instability is much weaker in comparison with the ion-ion counter streaming instability and ion-ion co-streaming instability growth rates of which are shown in chapters 4 and 5 respectively. In order to identify the growth rates in the different location of presheath, growth rates plot for Argon plasma with  $\frac{T_e}{T_i} = 100$  and  $\frac{V_i}{C_s} = 1, 0.9, 0.8, 0.7$  and  $0.6$  is presented in Figure 6.2. This figure clearly shows the instability maximum growth rate for ion velocities approaching Bohm velocity. Figure 6.3 shows the growth rate plots for different  $(T_e/T_i)$  ratio. This plot shows, the growth rates increases upto  $T_e/T_i = 200$  and then saturates. However, the possible unstable wavenumbers increases with increase in  $T_e/T_i$ .

As mentioned earlier, the growth rate of ion-acoustic instability shows, this in-

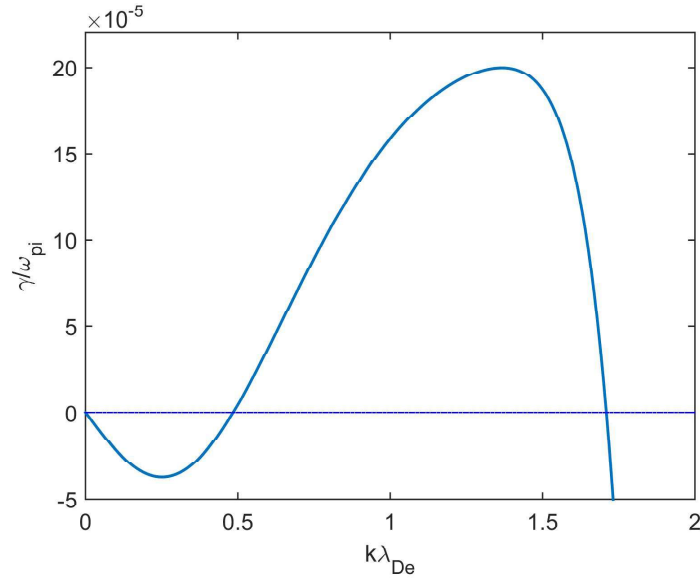


Figure 6.1: Growth rate plots of ion-acoustic instability for ion velocity  $V_i = 0.9$   $C_s$  and  $T_e/T_i = 100$ .

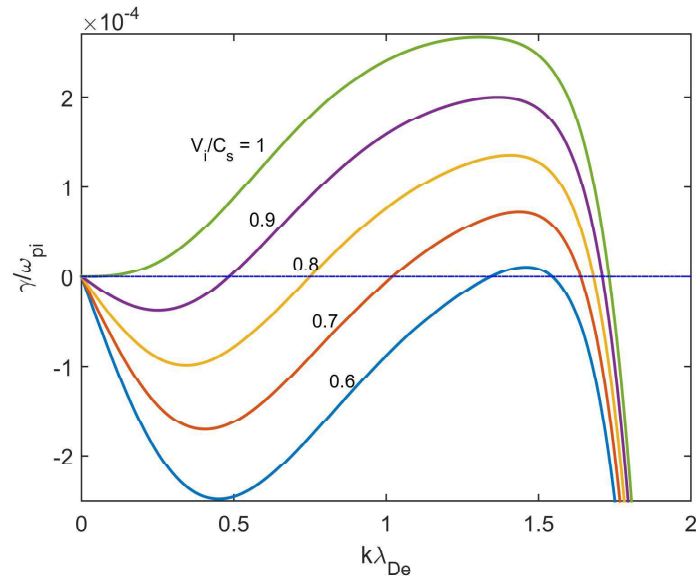


Figure 6.2: Growth rate plots of ion-acoustic instability for different ion velocities in the presheath normalized with Bohm velocity.

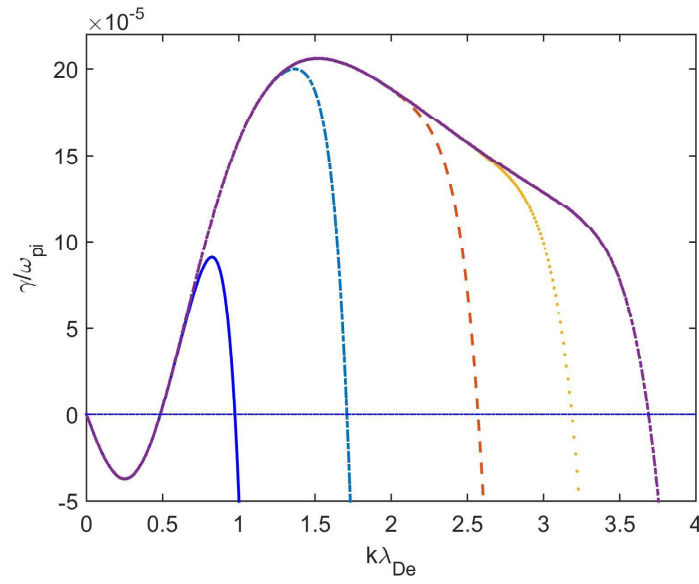


Figure 6.3: Growth rates for ion-acoustic instability near the sheath edge with different electron to ion temperature ratio ( $T_e/T_i$ ) and ion velocity  $V_i = 0.9 C_s$ .  $T_e/T_i = 50$  (solid line), 100 (dash-dot line), 200 (dash line), 300 (dotted line), and 400 (dot-dash line)

stability is much weaker in comparison with the earlier two instabilities i.e., ion-ion counter streaming instability and ion-ion co-streaming instability in the presheath. So this instability is much sensitive to the ion-neutral collisions. Baalrud derived pressure threshold for this instability by comparing the ion-neutral collisions frequency with the growth rate of the instability [11]. The pressure threshold to sustain the instability can be obtained from the condition  $\gamma_{max} \geq \nu_{in}$ , where  $\gamma$  is the growth rate of the ion-acoustic instability and  $\nu_{in}$  is the ion-neutral collision frequency. The ion-neutral collision frequency is given by the expression,  $\nu = n_g \sigma(V_i) V_i$ . This expressions is dominated by the collision cross-section  $\sigma(V_i)$ . From the ideal gas equation of state at the room temperature, the relation between neutral gas density ( $n_g$ ) and the pressure can be written as  $n_g[cm^{-3}] = 3 \times 10^{13} p [mTorr]$ . By using the condition,  $\gamma_{max} \geq \nu_{in}$ , an estimate for neutral pressure conditions required for ion-acoustic instability is obtained as,

$$p_c[mTorr] \leq \frac{4.5 \times 10^{-17}}{\sigma[cm^2]} \frac{\gamma_{max}}{\omega_{pi}} \frac{C_s}{V_i} \sqrt{\frac{n_e[cm^{-3}]}{T_e[eV]}} \quad (6.8)$$

BY considering the approximate value of charge exchange collision cross-section for Argon is  $\sigma = 10^{-15} cm^2$  [120, 127], and typical plasma density and temperatures  $5 \times 10^8/cc$  and 8 eV respectively, the pressure threshold obtained from Equation 6.8 is 0.11 mTorr, which shows this is a low-pressure phenomena, exists only in the low pressure discharges. However this approximation critically depends on ion-neutral collision cross-section data, which has to be evaluated properly in order to get the accurate estimation of pressure threshold.



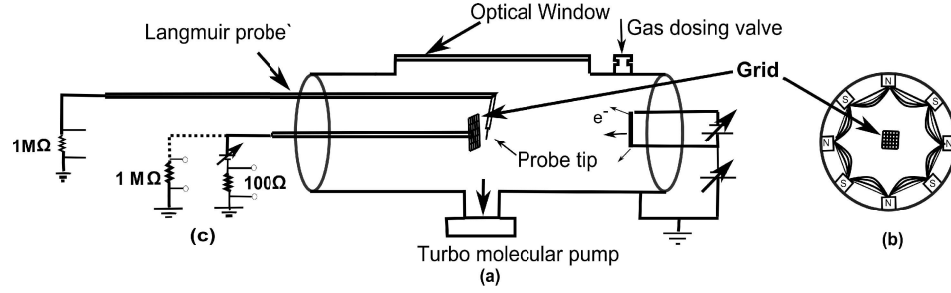


Figure 6.4: (a) Schematic diagram of the experimental set-up. (b) Cross-sectional view showing surface cusp magnetic field. (c) Circuit diagram for Grid and Langmuir probe.

## Plasma parameter regime

The experimental set-up is same as previous experiments, whose schematic diagram is as shown in Figure 6.4. The detailed description of the set-up is presented in Section 2.1. Based on the approximate pressure threshold derived in the last section, the discharge is operated in the low pressure regime,  $3 \times 10^{-4}$  to  $8 \times 10^{-4} \sim$  (0.2 to 0.6 mTorr) mbar to investigate the instability. The operation regime of discharge voltage and discharge current are 60 - 80 V and 0.6 - 1.2 A respectively. Typical plasma parameters are  $n_e = 2 \times 10^7 - 7 \times 10^8 \text{ cm}^{-3}$  and  $T_e = 4 - 8 \text{ eV}$ , where  $n_e$  and  $T_e$  are electron density and effective electron temperature respectively. Emissive probe is employed to measure the sheath-presheath potential profile and further to identify sheath, presheath boundaries [115].

### Experimental Results

These experiments are performed in single-ion species Argon plasma. Floating potential fluctuations from Langmuir probe placed near the sheath edge and from SS mesh grid are measured. Figure 6.5 shows the power spectrum of floating potential fluctuation signal at working pressure  $5 \times 10^{-4}$  mbar, discharge voltage 80 V and discharge current 1.0 A. Electron density and effective electron temperature are  $5 \times 10^8/\text{cc}$  and  $\sim 8$  eV respectively. The figure clearly shows two broad band peaks in the frequency range 10-20 kHz and 120-180 kHz are observed with these discharge parameters. The low frequency peak is identified to be ion-ion counter streaming instability excited in the presheath, which is described in chapter 4. The high frequency peak is predicted to be self-excited ion-acoustic instability in the presheath. To validate the ion-acoustic waves identity, the phase velocity and wave number of the wave corresponding to 120-180 kHz have been measured using the techniques described in the previous chapters. In this case, the Langmuir probe and grid are separated by 2.5 mm with error  $\pm 0.5$  mm. Figure 6.6 shows the phase lag as a function of frequencies. The phase lag for the central frequency of the broad band peak 160 kHz is  $0.1 \pi$  radians and corresponding time lag is  $0.3 \mu\text{Sec}$ , which gives phase velocity  $8.3 \pm 1.6$  km/sec. The wave number of the wave also estimated from measured phase velocity and central frequency of the peak. The obtained wave number is  $1.2 \pm 0.2 \text{ cm}^{-1}$ . The effective electron temperature is obtained from a planar Langmuir probe placed in the bulk plasma, far away from the sheath-presheath. The measured effective electron temperature is  $\sim 8$  eV and the system sound speed is 4.4 km/sec. Figure 6.6 also indicates that there is

no correlation between the signals above 200 kHz frequencies, means indication of noise above that frequency. The coherence between the signals shown in Figure 6.7 also implies that signals are coherent only in the low frequency (up to 30 kHz) and 120-180 kHz range.

This instability is identified to be sensitive to the experimental conditions and came to existence only in certain plasma parameters. The pressure regime in which the instability sustain the neutral damping is observed in the typical discharge. Figure 6.8 shows the the amplitude of the instability is prominent at  $5 \times 10^{-4}$  mbar with electron density  $5 \times 10^8$  /cc and electron temperature 8 eV. The instability is suppressed with increasing pressure beyond  $6.5 \times 10^{-4}$  mbar. This pressure regime to sustain the instability is observed to be very narrow. The approximate pressure threshold is obtained from Equation 6.8 for these plasma parameters with elastic, charge exchange collision cross-section for Argon  $\sigma = 10^{-15} \text{cm}^2$  [120, 127]. The obtained pressure threshold is 0.11 mTorr  $\cong 1.4 \times 10^{-4}$  mbar. So the experimentally observed pressure threshold are reasonably good agreement with the theory. Figure 6.9 shows the power spectra at a neutral pressure  $5 \times 10^{-4}$  mbar, discharge voltage 80 V and discharge current  $I_d = 1.0$  A and 0.6 A. The amplitude and central frequency of the high frequency peak decreases with discharge current, with which plasma density decreases.

## Discussion

Ion-acoustic instability excited in the presheath of low temperature plasma by virtue of differential flow between ions and electrons is theoretically explained to be reason for several interesting phenomena in sheath-presheath regime. In this

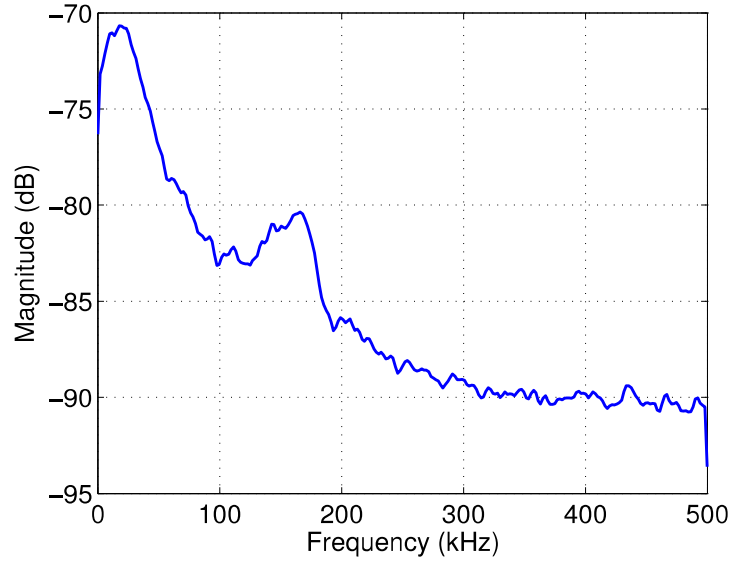


Figure 6.5: Frequency spectra of floating potential fluctuations from grid at a working pressure  $5 \times 10^{-4}$  mbar, electron density  $n_e = 3 \times 10^8/\text{cc}$  and effective electron temperature  $T_e = 8$  eV.

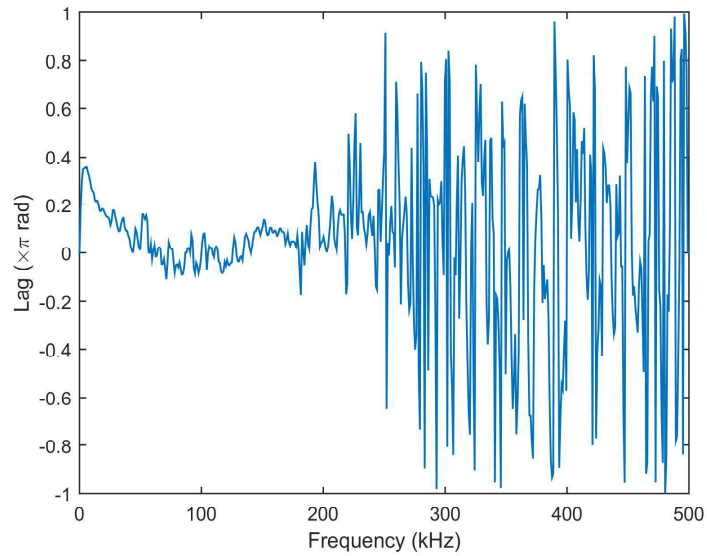


Figure 6.6: Phase with respect to frequency between grid and Langmuir probe floating potential fluctuations.

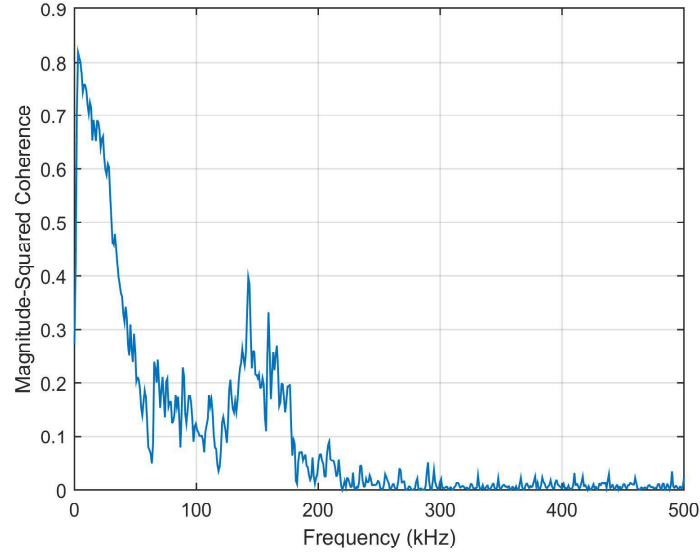


Figure 6.7: Coherence between grid and Langmuir probe floating potential fluctuations.

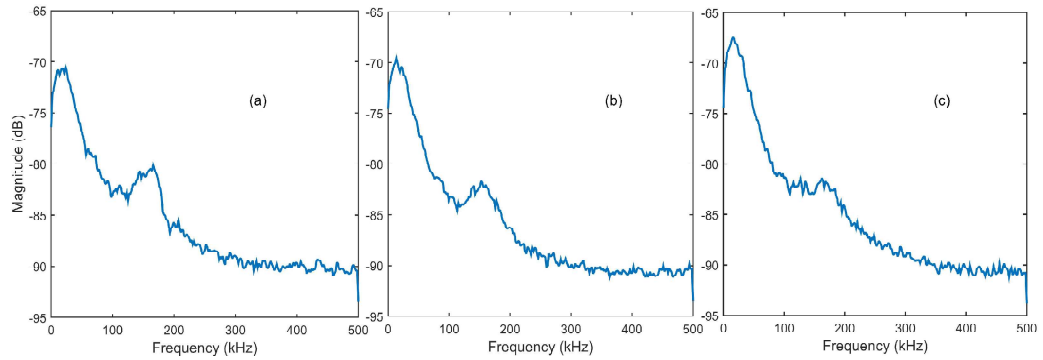


Figure 6.8: Power spectra of floating potential fluctuations at electron density  $\sim 8 \times 10^7/\text{cc}$ , effective electron temperature  $\sim 8$  eV and working pressure (a)  $5 \times 10^{-4}$  mbar (b)  $5.5 \times 10^{-4}$  mbar (c)  $6.5 \times 10^{-4}$  mbar.

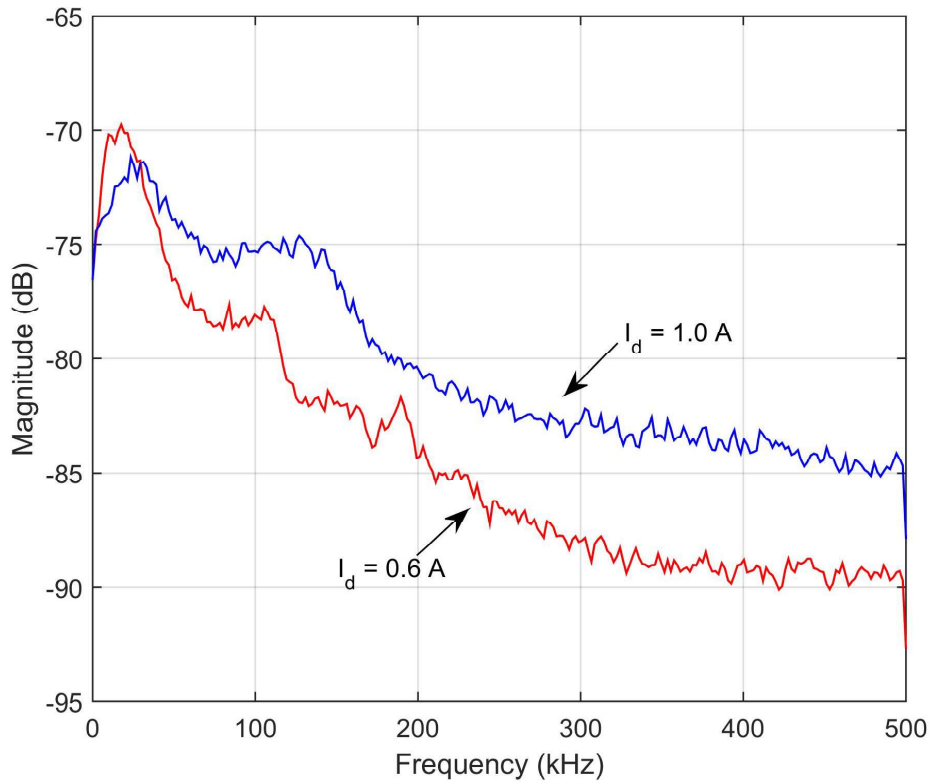


Figure 6.9: Comparison of power spectra of floating potential fluctuations at electron density  $6-8 \times 10^7/\text{cc}$ , effective electron temperature 7-8 eV and discharge currents  $I_d = 0.6$  A and 1.0 A

study, we experimentally observe the existence of the instability in the presheath around the mesh grid immersed in Argon plasma. The phase velocity and wave number of the excited wave are measured using simultaneously acquired floating potential fluctuations from Langmuir probe and grid. The phase velocity of the wave is observed to be  $8 \pm 1.6$  km/sec at plasma conditions with system sound speed 4.4 km/sec. These results are consistent with the previous study of ion acoustic wave velocity near the sheath edge by Oksuz *et al* [128]. These results show system sound speed near the sheath edge will be twice that of the velocity in bulk.

This instability is observed to be weak and sensitive to the experimental conditions unlike earlier ion-ion counter-streaming instability and ion-ion co-streaming instability. The pressure regime in which the instability sustains the neutral damping for the discharge conditions is observed. The suppression of instability with increasing working pressure shows the influence of ion-neutral collisions on the instability. This pressure regime is identified to be closer to the pressure threshold estimated by the model proposed by Baalrud [11].

## Conclusions and Future scope

This thesis presents the following three important experimental observation and characterization of ion flow driven instabilities in the sheath-presheath region of sheath system formed around a stainless steel (SS) mesh grid immersed in an unmagnetized, weakly ionized, low pressure, filament-produced single and two-ion species plasmas in a linear plasma device.

1. Ion-ion co-streaming instability (in two ion species plasma)
2. Ion-ion counter streaming instability (in single and two ion species plasmas)
3. Self-excited ion acoustic instability (in single ion species plasma)

To the best of our knowledge based on the available literature on the subject, the observations of ion-ion co streaming instability and ion-ion counter streaming instability in presheath-sheath region formed in a two ion-species plasma along



with ion acoustic instability in presheath-sheath region formed in a single ion species plasma are reported for the first time. The single species plasma studied are mainly produced in Argon and the two species plasma are produced with mixture of Argon and Helium. To carry out these studies, a simple and compact linear experimental device is constructed equipped with electric probe and spectroscopic diagnostics. The cylindrical vacuum chamber is made of stainless steel material having length 50 cm and inner diameter 20 cm. Hot-cathode filament discharge method with tungsten filaments is used for plasma production. The plasma density is enhanced by placing permanent NdFeB magnets along the inner surface of the chamber to produce cusp like magnetic fields in the poloidal periphery along the axis of the cylinder. The magnitude of magnetic field of these magnets reduces sharply from the cylinder wall (within few centimeters) and the core of the experimental chamber is magnetic field free. The magnetic field near the chamber wall improves the plasma confinement there. The diagnostics used in this study are planar and cylindrical Langmuir probes for plasma parameters measurement and fluctuation measurement respectively, current-heated and Laser-heated emissive probes for plasma potential measurement, sheath-presheath spatial potential profile measurement from which sheath and presheath boundaries identification is done and spectroscopy diagnostics. To study the thesis objectives, a sheath-presheath system has been formed around a stainless steel mesh grid placed in the center of the plasma. The dimension of the Sheath-presheath boundaries are determined by measuring spatial potential profile using Current-heated emissive probe and Laser-heated emissive probe. Sheath and presheath boundaries are identified by fitting experimental data with theoretical profiles. Simultaneously with these

measurements, the advantages of Laser-heated probe over current-heated probe especially in the measurement of potential in strong electric field have been explored. As the laser-heated probe does not require high currents to pass through it for heating, it seems to be more appropriate in potential measurement in presence of electric fields.

In this present thesis, three different ion-flow driven instabilities has been studied, namely (1) ion-ion co-streaming instability in the presheath of Ar+He plasma (2) ion-ion counter-streaming instability excited in the presheath of mesh grid placed in single and two-ion species plasmas (3) ion-acoustic instability excited in the presheath of Argon plasma.

Although ion-ion co-streaming instability has been invoked in many theoretical interpretations of physical phenomena occurring in laboratory and space plasmas such as ions of different masses reaching the sheath edge with equal velocity in two ion species plasma, enhanced friction between ions in sheath-presheath region of two ion species plasma, (give one space plasma example), direct experimental measurement of this instability is not yet reported. Direct evidence of existence of ion-ion co-streaming instability in the presheath is established in Ar + He two-ion species plasma by carrying out experiments in Ar + He two-ion species plasma. The frequency spectra of the floating potential fluctuations from the grid and LP placed in presheath region show a broad band peak with central frequency 160-300 kHz in plasma with nearly equal ion concentrations of both the ions. This broad band peak is not observed in a single species plasma under same experimental conditions and the amplitude of the peak decreases as the ion concentration ratio deviates from unity. The Langmuir probe data from presheath and bulk

plasmas indicates, the instability exists only in the presheath. The frequency of the measured wave matches quite well with the real frequency calculated from the dispersion relation of ion-ion co streaming instability at equal ion concentration. The measured frequency and amplitude variation with varying concentration ratio also follows the trends predicted by the theory. Further, the phase velocity and wavenumber of the excited waves are measured using time delay analysis of the fluctuation data from grid and LP. The average phase velocity is observed to be nearly twice the ion sound speed in the bulk plasma. These results are well in agreement with the previous results of ion wave velocity near the sheath edge in two-ion species plasma. The measured wave numbers are compared with theoretical dispersion relations.

The ion-ion counter streaming instability excited in the presheath of mesh grid placed in Ar, He and Ar+He plasmas is also observed in the sheath system of a mesh grid immersed in plasma. This instability is excited because of the counter streaming of ions penetrating the grid from both sides. In single ion species plasma, the central frequency of the peak is observed to be increasing with the plasma frequency, which is varied by changing discharge current and neutral pressure. The broadband frequency spectra peaks at lower frequency in Argon compared to that observed in Helium plasma which is due to higher mass of Argon. The wave number and phase velocity of the wave are measured by simultaneously acquiring the fluctuation data from Langmuir probe and the grid. These values are found to be in good agreement with those derived from dispersion relations. The work is further extended to measure and characterize this instability in two ion species plasmas. The frequency peaks are found to be broadened further in case of Ar

+ He plasma compared to the single species plasmas indicating existence of more number of possible wave numbers in two ion species plasma. This result is quite consistent with the derived dispersion relations of Ar + He two ion species plasma.

The self-excitation of ion-acoustic instability near the sheath edge is also predicted theoretically, but no experimental observation is reported till now. In our experiments with single-ion species Argon plasma, an appropriate plasma conditions have been discovered where this instability is observed and characterized. As the growth rate of this instability is very low compared to the other two instabilities explained above, it is very sensitive to the neutral pressure. Hence, it is sustained only in a very narrow region of neutral pressure. The effects of ion-neutral collisions on the instability is studied and a pressure threshold is obtained above which the instability is completely suppressed. The obtained pressure threshold is found to be in good agreement with the theoretical pressure threshold. The phase velocity and wavenumber of the excited waves are measured. The phase velocity of the excited waves near the sheath edge is observed to be nearly twice the ion sound speed in bulk plasma. These results are well in agreement with the previous results of measured ion acoustic wave velocity near the sheath edge, which are launched in the bulk plasma in a single-ion species plasma.

The results obtained in thesis have direct implications in industrial plasmas where the plasma generally contain two species and also in the extreme edge region of high temperature fusion plasma devices where presence of impurity in that location makes the plasma multi-ion species plasma. The plasma conditions for the ion-flow driven instabilities to exist in the presheath-sheath region of low temperature, unmagnetized plasmas have been established so that these instabilities

can be studied and understood experimentally.

### Future Scope

The experiments presented in this thesis work established the presence of the ion-flow driven instabilities in the sheath-presheath region. One of them, the ion-ion co streaming instability, has been proven theoretically to explain the experimental observations of equal velocities of ions of different masses at the sheath edge in two ion species plasmas. Hence, the measurement of the ion flow speeds simultaneously with the observations of the instabilities will be carried out. Laser induced fluorescence technique can be used for the same. In the experiments, the floating potential fluctuations in the presheath region are measured with LP, which can disturb the sheath-presheath region by having its own sheath around it. Hence, non-invasive spectroscopic techniques will be used to measure the light fluctuation measurement emitting from different ion species. With these measurements the oscillations of different species and their synchronization (if any) will be studied as a function of ion concentrations in Ar + He plasma. Ion-ion counter streaming and ion acoustic instabilities are observed to be excited in the presheath of grids. For this instability, the width of broadband peak in the frequency spectra of floating potential fluctuations increased in Ar and He plasma as compared to plasmas with Ar and He alone. This is quite consistent with the theoretical prediction, as indicated by the dispersion relation, more number of ks are possible in mixture of gases. The theory also predicts that, the width further increases as one increases the mass difference of the ions present in the multi or two species plasma. So experiments with more combination of gases having more mass dif-

ference like He-Kr or He-Xe or Ar-Xe will be carried out to verify the theoretical predictions. The ion-acoustic instability is observed to have low neutral pressure cut-off too, which is not understood. Further experiments will be carried out to understand the physical reason behind existence of this lower-cutoff. All these experiments are carried out in unmagnetized plasma. These experiments will be repeated in presence of magnetic field of different strength and orientation near the sheath-presheath region.

# Bibliography

- [1] K U Riemann. The Bohm criterion and sheath formation. *Journal of Physics D: Applied Physics*, 24(4):493–518, 1991.
- [2] D R McCarthy, Peter J Catto, and S I Krasheninnikov. Nonlocal theory and turbulence of the sheath-driven electron temperature gradient instability. *Physics of Plasmas*, 8(3):750, 2001.
- [3] Peter Vitello. Pre-sheaths and Turbulent Flow in Electronegative Plasmas. *Japanese Journal of Applied Physics*, 38(7B):4283–4290, 1999.
- [4] M. Griskey and R. Stenzel. Secondary-Electron-Emission Instability in a Plasma. *Physical Review Letters*, 82(3):556–559, 1999.
- [5] M. D. Campanell, A. V. Khrabrov, and I. D. Kaganovich. General cause of sheath instability identified for low collisionality plasmas in devices with secondary electron emission. *Physical Review Letters*, 108(23):1–5, 2012.
- [6] Vara Prasad Kella, J. Ghosh, P. K. Chattopadhyay, D. Sharma, and Y. C. Saxena. Observation of ion-ion counter streaming instability in presheath-sheath region of a mesh grid immersed in low temperature plasma. *Physics of Plasmas*, 24(3):032110, 2017.
- [7] Y. Nakamura and S. Sato. Strong low-frequency turbulence observed in presheaths. *Physics of Plasmas*, 10(3):900–904, 2003.

## Bibliography

---

- [8] S. D. Baalrud, C. C. Hegna, and J. D. Callen. Instability-Enhanced collisional friction can determine the bohm criterion in multiple-ion-species plasmas. *Physical Review Letters*, 103(20):205002, 2009.
- [9] Scott D Baalrud, Trevor Lafleur, William Fox, and Kai Germaschewski. Instability-enhanced friction in the presheath of two-ion-species plasmas. *Plasma Sources Science and Technology*, 24(1):015034, 2015.
- [10] Vara Prasad Kella, J. Ghosh, D. Sharma, Y. C. Saxena, and P. K. Chattopadhyay. Experimental observation of ion-ion co-streaming instability in presheath region of mesh grid immersed in ar+he two-ion-species laboratory plasma. *to be submitted*.
- [11] Scott D Baalrud. Influence of ion streaming instabilities on transport near plasma boundaries. *Plasma Sources Science and Technology*, 25(2):25008, 2016.
- [12] D B Fenneman, M Raether, and M Yamada. Ion-acoustic instability in the positive column of a helium discharge. *Physics of Fluids*, 16(6):871, 1973.
- [13] E. Ahedo and F. I. Parra. Partial trapping of secondary-electron emission in a Hall thruster plasma. *Physics of Plasmas*, 12(7):1–7, 2005.
- [14] S D Baalrud and C C Hegna. Kinetic theory of the presheath and the Bohm criterion. *Plasma Sources Science and Technology*, 20(2):025013, 2011.
- [15] R M Winglee, P B Dusenbery, H L Collin, C S Lin, and A M Persoon. Simulations and Observations of Heating of Auroral Ion Beams. *Journal of Geophysical Research: Space Physics*, 94:8943–8965, 1989.



- [16] Chi-Shung Yip, Noah Hershkowitz, and Greg Severn. Ion velocity-locking in the neighborhood of virtual cathodes via instability enhanced collisional friction. *Plasma Sources Science and Technology*, 26(1):015008, 2017.
- [17] D. Winske, J. Giacalone, M. F. Thomsen, and M. M. Mellott. A comparative study of plasma heating by ion acoustic and modified two-stream instabilities at subcritical quasi-perpendicular shocks. *Journal of Geophysical Research: Space Physics*, 92(A5):4411–4422, 1987.
- [18] H Tanaca, A Hirose, and M Koganei. Ion-Wave Instabilities in Mercury-Vapor Plasma. *Phys. Rev.*, 161(1):94–101, 1967.
- [19] M Yamada and M Raether. Evolution of the ion acoustic instability in a direct current discharge plasma. *Physics of Fluids*, 18:361–368, 1975.
- [20] N Th. Karatzas, A J Anastassiadis, and K Papadopoulos. Generation and Behavior of Large-Amplitude Ion-Acoustic Waves. *Phys. Rev. Lett.*, 35(1):33–36, 1975.
- [21] Y. Kawai, Ch. Hollenstein, and M. Guyot. Ion acoustic turbulence in a large-volume plasma. *Physics of Fluids*, 21(6):970, 1978.
- [22] S. D. Baalrud, J. D. Callen, and C. C. Hegna. Instability-enhanced collisional effects and Langmuir’s paradox. *Physical Review Letters*, 102(24):245005, 2009.
- [23] G. D. Severn, Xu Wang, Eunsuk Ko, and N. Hershkowitz. Experimental Studies of the Bohm Criterion in a Two-Ion-Species Plasma Using Laser-Induced Fluorescence. *Physical Review Letters*, 90(14):145001, 2003.

## Bibliography

---

- [24] N. Hershkowitz, C. S. Yip, and G. D. Severn. Experimental test of instability enhanced collisional friction for determining ion loss in two ion species plasmas. *Physics of Plasmas*, 18(5):057102, 2011.
- [25] Vara Prasad Kella, J. Ghosh, D. Sharma, Y. C. Saxena, and P. K. Chattopadhyay. Self-excited ion-acoustic instability in the presheath of low temperature plasma. *to be submitted*.
- [26] Peratt Anthony L. *Physics of the Plasma Universe*. Springer-Verlag New York, Inc., 1992.
- [27] R. Udiljak, D. Anderson, M. Lisak, V. E. Semenov, and J. Puech. Improved model for multipactor in low pressure gas. *Physics of Plasmas*, 11(11):5022–5031, 2004.
- [28] Liebermann M.A. and Linchtenberg Alan J. *Principles of Plasma Discharges and Materials Processing*. Wiley Publications, 2005.
- [29] Wesson John. *Tokamaks*. Oxford Science Publications, 1997.
- [30] F. F. Chen. *Introduction to Plasma Physics and Controlled Fusion*. Springer, 1984.
- [31] Kikuchi Mitsuru and Azumi Masafumi. *Frontiers in Fusion Research II: Introduction to Modern Tokamak Physics*. Springer International Publishing, 2015.
- [32] John D Lindl, Robert L Mccrory, and E Michael Campbell. Progress towards ignition and burn propagation in Inertial fusion confinement. *Physics Today*, page 32, September 1992.

- [33] M. I. Boulos. Thermal plasma processing. *IEEE Transactions on Plasma Science*, 19(6):1078–1089, 1991.
- [34] J Hopwood. Review of inductively coupled plasmas for plasma processing. *Plasma Sources Science and Technology*, 1(2):109, 1992.
- [35] Hyun-Ha Kim. Nonthermal plasma processing for air-pollution control: A historical review, current issues, and future prospects. *Plasma Processes and Polymers*, 1(2):91–110, 2004.
- [36] T. Czerwiec, H. Michel, and E. Bergmann. Low-pressure, high-density plasma nitriding: mechanisms, technology and results. *Surface and Coatings Technology*, 108:182 – 190, 1998.
- [37] P J Kelly and R D Arnell. Magnetron sputtering : a review of recent developments and applications. *Vacuum*, 56:159–172, 2000.
- [38] J Hopwood. Review of inductively coupled plasmas for plasma processing. *Plasma Sources Science and Technology*, 1(2):109, 1992.
- [39] R. G. Poulsen. Plasma etching in integrated circuit manufacture-a review. *Journal of Vacuum Science and Technology*, 14(1):266–274, 1977.
- [40] Keizo Suzuki, Sadayuki Okudaira, Noriyuki Sakudo, and Ichiro Kanomata. Microwave plasma etching. *Japanese Journal of Applied Physics*, 16(11):1979–1984, 1977.
- [41] Roya Dastjerdi and Majid Montazer. Colloids and Surfaces B : Biointerfaces A review on the application of inorganic nano-structured materials in the

- modification of textiles : Focus on anti-microbial properties. *Colloids and Surfaces B: Biointerfaces*, 79(1):5–18, 2010.
- [42] A L Yerokhin, L O Snizhko, N L Gurevina, A Leyland, A Pilkington, and A Matthews. Discharge characterization in plasma electrolytic oxidation of aluminium. *Journal of Physics D: Applied Physics*, 36(17):2110, 2003.
- [43] J. Karthikeyan, C.C. Berndt, J. Tikkanen, S. Reddy, and H. Herman. Plasma spray synthesis of nanomaterial powders and deposits. *Materials Science and Engineering: A*, 238(2):275 – 286, 1997.
- [44] K. Moustakas, D. Fatta, S. Malamis, K. Haralambous, and M. Loizidou. Demonstration plasma gasification/vitrification system for effective hazardous waste treatment. *Journal of Hazardous Materials*, 123(1):120 – 126, 2005.
- [45] Ray W.Y. Poon, Joan P.Y. Ho, Xuanyong Liu, C.Y. Chung, Paul K. Chu, Kelvin W.K. Yeung, William W. Lu, and Kenneth M.C. Cheung. Improvements of anti-corrosion and mechanical properties of niti orthopedic materials by acetylene, nitrogen and oxygen plasma immersion ion implantation. *Nuclear Instruments and Methods in Physics Research Section B: Beam Interactions with Materials and Atoms*, 237(1):411 – 416, 2005.
- [46] A Rabiei and A.G Evans. Failure mechanisms associated with the thermally grown oxide in plasma-sprayed thermal barrier coatings. *Acta Materialia*, 48(15):3963 – 3976, 2000.

- [47] K.-U. Riemann. Bohm's criterion and plasma-sheath transition. *Contributions to Plasma Physics*, 36(S1):19–27, 1996.
- [48] Devendra Sharma and Predhiman K. Kaw. Valid flow combinations for stable sheath in a magnetized multiple ion species plasma. *Physics of Plasmas*, 19(11):113507, 2012.
- [49] H-B Valentini and F Herrmann. Boundary value problems for multi-component plasmas and a generalized bohm criterion. *Journal of Physics D: Applied Physics*, 29(5):1175, 1996.
- [50] K.U. Riemann. The validity of bohms sheath criterion in rf discharges. *Physics of Fluids B: Plasma Physics*, 4(9):2693–2695, 1992.
- [51] C Stangeby Peter. *The Plasma Boundary of Magnetic Fusion Devices*. CRC Press, 2000.
- [52] K.-U. Riemann. The influence of collisions on the plasma sheath transition. *Physics of Plasmas*, 4(11):4158–4166, 1997.
- [53] I Roth, M K Hudson, and R Bergmann. Effects of ion two-stream instability on auroral ion heating. *Journal of Geophysical Research: Space Physics*, 94(A1):348–358, 1989.
- [54] L. Muschietti and I. Roth. Ion two-stream instabilities in the auroral acceleration zone. *Journal of Geophysical Research*, 113:A08201, 2008.
- [55] R N Franklin. The plasma-sheath and its stability in a quiescent plasma containing two species of positive ion. *Journal of Physics D: Applied Physics*, 36(15):1806–1809, 2003.

## Bibliography

---

- [56] J. T. Gudmundsson and M. A. Lieberman. Ar<sup>+</sup> and Xe<sup>+</sup> velocities near the presheath-sheath boundary in an Ar/Xe discharge. *Physical Review Letters*, 107(4):045002, 2011.
- [57] G. D. Severn, Xu Wang, Eunsuk Ko, and N. Hershkowitz. Experimental Studies of the Bohm Criterion in a Two-Ion-Species Plasma Using Laser-Induced Fluorescence. *Physical Review Letters*, 90(14):145001, 2003.
- [58] X. Wang and N. Hershkowitz. Experimental studies of the two-ion species flow in the plasma presheath. *Physics of Plasmas*, 13(5):053503, 2006.
- [59] Chi-Shung Yip, Noah Hershkowitz, and Greg Severn. Experimental Test of Instability-Enhanced Collisional Friction for Determining Ion Loss in Two Ion Species Plasmas. *Physical Review Letters*, 104(22):225003, 2010.
- [60] S. D. Baalrud and C. C. Hegna. Determining the bohm criterion in plasmas with two ion species. *Physics of Plasmas*, 18(2):023505, 2011.
- [61] Chi-Shung Yip, Noah Hershkowitz, and Greg Severn. Ion velocity-locking in the neighborhood of virtual cathodes via instability enhanced collisional friction. *Plasma Sources Science and Technology*, 26(1):015008, 2016.
- [62] Dongsoo Lee, Noah Hershkowitz, and Greg D. Severn. Measurements of Ar<sup>+</sup> and Xe<sup>+</sup> velocities near the sheath boundary of Ar-Xe plasma using two diode lasers. *Applied Physics Letters*, 91(4):16–19, 2007.
- [63] N. Hershkowitz, C. S. Yip, and G. D. Severn. Experimental test of instability enhanced collisional friction for determining ion loss in two ion species plasmas. *Physics of Plasmas*, 18(5):057102, 2011.

- [64] J. T. Gudmundsson and M. A. Lieberman. Ar<sup>+</sup> and Xe<sup>+</sup> velocities near the presheath-sheath boundary in an Ar/Xe discharge. *Physical Review Letters*, 107(4):045002, 2011.
- [65] N. Hershkowitz, Xu Wang, and A. M. A. Hala. Presheath environment in weakly ionized single and multispecies plasmas. *IEEE Transactions on Plasma Science*, 33(2):631–636, 2005.
- [66] Chi-Shung Yip, Noah Hershkowitz, and Greg Severn. Verifying effects of instability enhanced ion-ion Coulomb collisions on ion velocity distribution functions near the sheath edge in low temperature plasmas. *Plasma Sources Science and Technology*, 24:015018, 2015.
- [67] S D Baalrud, J D Callen, and C C Hegna. Instability-enhanced collisional effects and Langmuir’s paradox. *Phys Rev Lett*, 102(24):245005, 2009.
- [68] Lutfi Oksuz, Dongsoo Lee, and Noah Hershkowitz. Ion acoustic wave studies near the presheath/sheath boundary in a weakly collisional argon/xenon plasma. *Plasma Sources Science and Technology*, 17(1):015012, 2008.
- [69] R. Udiljak, D. Anderson, M. Lisak, V. E. Semenov, and J. Puech. Improved model for multipactor in low pressure gas. *Physics of Plasmas*, 11(11):5022–5031, 2004.
- [70] Ward Handley and Scott Robertson. A hot-filament discharge with very low electron temperature. *Physics of Plasmas*, 16(1):010702, 2009.
- [71] Scott Robertson and Zoltan Sternovsky. Model for the density, temperature,

## Bibliography

---

- and plasma potential of low-density hot-filament discharges. *Physical Review E*, 72(1):016402, 2005.
- [72] H M Mott-Smith and Irving Langmuir. The Theory of Collectors in Gaseous Discharges. *Phys. Rev.*, 28(4):727–763, 1926.
- [73] Robert L. Merlino. Understanding Langmuir probe current-voltage characteristics. *American Journal of Physics*, 75(12):1078, 2007.
- [74] H. Morkoç, S. Strite, G. B. Gao, M. E. Lin, B. Sverdlov, and M. Burns. Large-band-gap SiC, III-V nitride, and II-VI ZnSe-based semiconductor device technologies. *Journal of Applied Physics*, 76(3):1363–1398, 1994.
- [75] S J Davies, P D Morgan, Y Ul’Haq, C F Maggi, S K Erents, W Fundamenski, L D Horton, A Loarte, G F Matthews, R D Monk, and P C Stangeby. Parallel electron temperature and density gradients measured in the {JET} MkI divertor using thermal helium beams. *Journal of Nuclear Materials*, 241-243:426–432, 1997.
- [76] Y Andrew, S J Davies, D Elder, L D Horton, G F Matthews, A Meigs, P D Morgan, M O’Mullane, M Stamp, R Prentice, and P C Stangeby. Interpretative modelling of JET’s thermal helium diagnostic. *Journal of Nuclear Materials*, 266-269:1234–1239, 1999.
- [77] Y Andrew and M G O’Mullane. Sensitivity of calculated neutral helium line intensities and their ratios to uncertainties in excitation rate coefficients. *Plasma Physics and Controlled Fusion*, 42(3):301, 2000.



- [78] J M Carmona, K J McCarthy, R Balbín, and S Petrov. Charge-exchange spectroscopic diagnostic for the TJ-II stellarator. *Review of Scientific Instruments*, 77(10), 2006.
- [79] S. P. Cunningham. in conference on thermonuclear reactors. *US Atomic Energy Commission Report No. 279*, Livermore, 1955.
- [80] V. A. Godyak and B. M. Alexandrovich. Comparative analyses of plasma probe diagnostics techniques. *Journal of Applied Physics*, 118(23):233302, 2015.
- [81] M. B. Hopkins and W. G. Graham. Langmuir probe technique for plasma parameter measurement in a medium density discharge. *Review of Scientific Instruments*, 57(9):2210–2217, 1986.
- [82] S H Lam. Unified Theory for the Langmuir Probe in a Collisionless Plasma. *Physics of Fluids*, 8(1):73–87, 1965.
- [83] F F Chen, editor. *Plasma Diagnostics Techniques*. Academic, New York, 1965.
- [84] M J M Parrot, L R O Storey, L W Parker, and J G Laframboise. Theory of cylindrical and spherical Langmuir probes in the limit of vanishing Debye number. *Physics of Fluids*, 25(12):2388, 1982.
- [85] V Godyak, R Lagushenko, and J Maya. Spatial evolution of the electron-energy distribution in the vicinity of a discharge-tube constriction. *Phys. Rev. A*, 38(4):2044–2055, 1988.

## Bibliography

---

- [86] Lin Kui-Xun, Lin Xuan-Ying, Chi Ling-Fei, Yu Chu-Ying, Yao Ruo-He, and Yu Yun-Peng. The reliability of measurements on electron energy distribution function in silane rf glow discharges. *Chinese Physics*, 12(2):198, 2003.
- [87] M B Hopkins and W G Graham. Electron energy distribution function measurements in a magnetic multipole plasma. *Journal of Physics D: Applied Physics*, 20(7):838, 1987.
- [88] Fumiyuki Fujita and Hatsuo Yamazaki. Determination of Electron Energy Distribution Function of Plasmas by Digital Processing from Langmuir Probe Characteristic. *Japanese Journal of Applied Physics*, 29(10R):2139, 1990.
- [89] Yu.B. Pankrashkin and M B Shapochkin. Investigation of the anisotropic electron distribution function in a glow discharge in hydrogen. *Plasma Physics Reports*, 29(12):1056–1061, 2003.
- [90] Hiroshi Amemiya. Experiments on the Energy Distribution Function in Hydrogen Plasmas. *Japanese Journal of Applied Physics*, 25(4R):595, 1986.
- [91] A. A. Azooz. Four free parameter empirical parametrization of glow discharge Langmuir probe data. *Review of Scientific Instruments*, 79(10):103501, 2008.
- [92] Aasim A. Azooz and Zyad Tarik Ali. Two temperatures components in CCP argon 13.56-MHz RF discharge. *IEEE Transactions on Plasma Science*, 43(5):1774–1779, 2015.
- [93] Matlab file exchange. <http://www.mathworks.com/matlabcentral/fileexchange>.

- [94] R F Boivin, J L Kline, and E E Scime. Electron temperature measurement by a helium line intensity ratio method in helicon plasmas. *Physics of Plasmas*, 8(12):5303, 2001.
- [95] McWhirter. R. W. P. *Plasma Diagnostic Techniques*. Academic Press, New York, 1965.
- [96] Dinklage Andreas, Klinger Thomas, Marx Gerrit, and Schweikhard Lutz. *Plasma Physics-Confinement, Transport and Collective Effects*. Springer-Verlag Berlin Heidelberg, 2005.
- [97] J M Beall, Y C Kim, and E J Powers. Estimation of wavenumber and frequency spectra using fixed probe pairs. *Journal of Applied Physics*, 53(6):3933, 1982.
- [98] J. P. Sheehan, Y. Raitses, N. Hershkowitz, I. Kaganovich, and N. J. Fisch. A comparison of emissive probe techniques for electric potential measurements in a complex plasma. *Physics of Plasmas*, 18(7):073501, 2011.
- [99] Wang En Yao, T. Intrator, and N. Hershkowitz. Direct indication technique of plasma potential with differential emissive probe. *Review of Scientific Instruments*, 56(4):519–524, 1985.
- [100] D. Diebold, N. Hershkowitz, A. D. Bailey, M. H. Cho, and T. Intrator. Emissive probe current bias method of measuring dc vacuum potential. *Review of Scientific Instruments*, 59(2):270–275, 1988.
- [101] M Sato and Y Hatta. Glowing probe for space potential measurement in gas discharges. *Journal of Scientific Instruments*, 39(9):481, 1962.

## Bibliography

---

- [102] Roman Schrittwieser, Codrina Ionita, Petru Balan, Ramona Gstrein, Olaf Grulke, Thomas Windisch, Christian Brandt, Thomas Klinger, Ramin Madani, George Amarandei, and Arun K. Sarma. Laser-heated emissive plasma probe. *Review of Scientific Instruments*, 79(8), 2008.
- [103] M Mizumura, S Uotsu, S Matsumura, and S Teii. Probe system with bias compensation using a laser heated emissive probe for RF discharge plasma diagnostics. *Journal of Physics D: Applied Physics*, 25(12):1744, 1992.
- [104] Payal Mehta, Arun Sarma, Joydeep Ghosh, Shwetang Pandya, Santosh Pandya, Paritosh Choudhuri, J. Govindarajan, C. Ionita Schrittwieser, and Roman Schrittwieser. Measurement of emission current and temperature profile of emissive probe materials using CO2 LASER. *Current Applied Physics*, 11(5):1215–1221, 2011.
- [105] E. Mravlag and P. Krumm. Space potential measurements with a continuously emitting probe. *Review of Scientific Instruments*, 61(8):2164–2170, 1990.
- [106] X. Wang, C. T. Howes, M. Horányi, and S. Robertson. Effect of filament supports on emissive probe measurements. *Review of Scientific Instruments*, 84(1):210–213, 2013.
- [107] J P Sheehan and N Hershkowitz. Emissive probes. *Plasma Sources Science and Technology*, 20(6):063001, 2011.
- [108] Robert F. Kemp and J. M. Sellen. Plasma potential measurements by electron emissive probes. *Review of Scientific Instruments*, 37(4):455–461, 1966.

- [109] J. J. Schuss. Behavior of electron-emitting plasma probes in the space-charge-limited regime. *Journal of Applied Physics*, 45(11):4778, 1974.
- [110] N. Hershkowitz and M. H. Cho. Measurement of plasma potential using collecting and emitting probes. *Journal of Vacuum Science & Technology A: Vacuum, Surfaces, and Films*, 6(3):2054–2059, 1988.
- [111] J. R. Smith, N. Hershkowitz, and P. Coakley. Inflection-point method of interpreting emissive probe characteristics. *Review of Scientific Instruments*, 50(2):210–218, 1979.
- [112] C R Hoffmann and D J Lees. A differential method of measuring plasma potential. *Plasma Physics*, 13(8):689, 1971.
- [113] Edward Ott, John B. McBride, Joseph H. Orens, and Jay P. Boris. Turbulent heating in computer simulations of the modified plasma two-stream instability. *Physical Review Letters*, 28(2):88–91, 1972.
- [114] Nagendra Singh, H Thiemann, and R W Schunk. Studies on counterstreaming plasma expansion. *Physica Scripta*, 33(4):355, 1986.
- [115] Vara Prasad Kella, Payal Mehta, A Sarma, J Ghosh, and P K Chattopadhyay. A comparative study of sheath potential profile measurements with laser-heated and current-heated emissive probes. *Review of Scientific Instruments*, 87(4):043508, 2016.
- [116] Robert L Merlino. Understanding Langmuir probe current-voltage characteristics. *American Journal of Physics*, 75(12):1078–1085, 2007.

## Bibliography

---

- [117] S K Wong and N A Krall. A nonlocal theory of counterstreaming ion instability. *Physics of Fluids B*, 5:1706, 1993.
- [118] R N Franklin. Plasmas with more than one species of positive ion and the bohm criterion. *Journal of Physics D: Applied Physics*, 33(24):3186–3189, 2000.
- [119] Xiang Nong, Hu Yemin, and Ou Jing. Bohm criterion for collisionless sheaths in two-ion-species plasmas. *Plasma Science and Technology*, 13(4):385, 2011.
- [120] Nam-Kyun Kim, Jaemin Song, Hyun-Joon Roh, Yunchang Jang, Sangwon Ryu, Sung-Ryul Huh, and Gon-Ho Kim. Ion-neutral collision effect on ion-ion two-stream-instability near sheath-presheath boundary in two-ion-species plasmas. *Plasma Sources Science and Technology*, 26(6):06LT01, 2017.
- [121] Antony Soosaleon and Blesson Jose. Two Stream Instability as a Source of Coronal Heating. *International Journal of Astronomy and Astrophysics*, 5:61–69, 2015.
- [122] R. L. Kaufmann, G. R. Ludlow, H. L. Collin, W. K. Peterson, and J. L. Burch. Interaction of upgoing auroral  $h^+$  and  $o^+$  beams. *Journal of Geophysical Research: Space Physics*, 91(A9):10080–10096, 1986.
- [123] S. D. Baalrud and C. C. Hegna. Determining the Bohm criterion in plasmas with two ion species. *Physics of Plasmas*, 18(2):023505, 2011.
- [124] U Deka, C B Dwivedi, and H Ramachandran. Propagation of ion-acoustic wave in the presheath region of a plasma sheath system. *Physica Scripta*, 73(1):87–97, 2006.

- [125] D B Fenneman, M Raether, and M Yamada. Ion-acoustic instability in the positive column of a helium discharge. *Physics of Fluids*, 16(6):871, 1973.
- [126] Christopher Rapson, Olaf Grulke, Konstantin Matyash, and Thomas Klinger. The effect of boundaries on the ion acoustic beam-plasma instability in experiment and simulation. *Physics of Plasmas*, 21(2014):052103, 2014.
- [127] John W. Sheldon. Correlation of resonance charge exchange cross-section data in the low-energy range. *Phys. Rev. Lett.*, 8:64–65, 1962.
- [128] Lutfi Oksuz, Dongsoo Lee, and Noah Hershkowitz. Ion acoustic wave studies near the presheath/sheath boundary in a weakly collisional argon/xenon plasma. *Plasma Sources Science and Technology*, 17(1):015012, 2008.